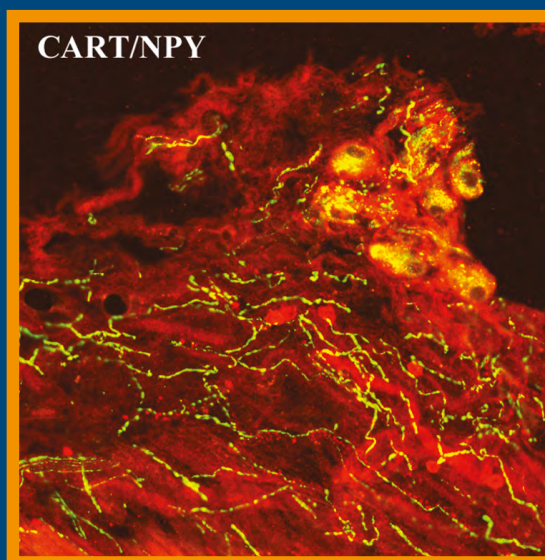


Folia Histochemica et Cytobiologica

Scientific quarterly devoted to problems of histochemistry,
cytochemistry and cell & tissue biology

https://journals.viamedica.pl/folia_histochemica_cytobiologica



Impact Factor:
1.698

Vol. 59
No. 3
2021

ISSN 0239-8508
e-ISSN 1897-5631

Folia Histochemica et Cytobiologica

Scientific quarterly devoted to problems of histochemistry,
cytochemistry and cell & tissue biology

Vol. 59

No. 3

2021

https://journals.viamedica.pl/folia_histochemica_cytobiologica

Official Journal of the Polish Society for Histochemistry and Cytochemistry

EDITOR-IN CHIEF:

Z. Kmiec (Gdansk, Poland)

EDITORS:

A.A. Brozyna (Bydgoszcz, Poland)

M. Piasecka (Szczecin, Poland)

M.Z. Ratajczak (Louisville, USA)

J. Thekkiniath (New Haven, USA)

EDITORIAL BOARD:

C.E. Alpers (Seattle, USA)

B. Bilinska (Cracow, Poland)

I.-D. Caruntu (Iasi, Romania)

J.R. Couchman (Copenhagen, Denmark)

M. Dietel (Berlin, Germany)

P. Dziegiel (Wroclaw, Poland)

T. Fujimoto (Nagoya, Japan)

S.D. Gadau (Sassari, Italy)

J. Kawiak (Warsaw, Poland)

J.Z. Kubiak (Rennes, France)

J.A. Litwin (Cracow, Poland)

C. Lucini (Naples, Italy)

A. Lukaszuk (Poznan, Poland)

Z. Mackiewicz (Vilnius, Lithuania)

A. Mazur (Clermont-Ferrand, France)

I. Petersen (Jena, Germany)

A.T. Slominski (Birmingham, USA)

C.J.F. van Noordan (Amsterdam, Netherlands)

C. Pellicciari (Pavia, Italy)

Y. Wegrowski (Reims, France)

S. Wolczynski (Bialystok, Poland)

M. Zabel (Poznan, Poland)

V. Zinchuk (Kochi, Japan)

M. J. Zeromski (Poznan, Poland)

M.A. Zmijewski (Gdansk, Poland)

MANAGING EDITOR:

C. Kobierzycki (Wroclaw, Poland)

PUBLISHER EDITOR:

I. Hallmann (Gdansk, Poland)

EDITORIAL OFFICE:

Department of Histology

Medical University of Gdansk

Debinki St. 1, 80–210 Gdansk, Poland

tel.: + 48 58 349 14 37

fax: + 48 58 349 14 19

e-mail: zkmiecc@gumed.edu.pl

https://journals.viamedica.pl/folia_histochemica_cytobiologica

Folia Histochemica et Cytobiologica (ISSN 0239-8508, e-ISSN 1897-5631) is published quarterly, one volume a year, by the Polish Society for Histochemistry and Cytochemistry at VM Media sp. z.o.o VM Group sp.k., Gdansk.

Indexed in: Index Medicus/MEDLINE, Excerpta Medica/EMBASE, Chemical Abstracts/CAS, SCI Expanded, Biochemistry & Biophysics Citation Index, Biosis Previews, Biological Abstracts, SCOPUS, ProQuest, EBSCO, DOAJ, Ulrich's Periodicals Directory, CrossRef, Free Medical Journals, Google Scholar, Medical Journals Links, Polish Scientific Bibliography/Polindex, Polish Medical Library (GBL), ROAD Directory of Open Access Scholarly, WorldCat (OCLC), Index Copernicus (149.79 points), Polish Ministry of Education and Science (70 points). Current Impact Factor of "Folia Histochemica et Cytobiologica" (2020) is 1.698.

POLISH SOCIETY FOR HISTOCHEMISTRY AND CYTOCHEMISTRY STATEMENT OF FOLIA HISTOCHEMICA ET CYTOBIOLOGICA EDITORIAL POLICY

Folia Histochemica et Cytobiologica is an international, English-language journal devoted to the rapidly developing fields of histochemistry, cytochemistry, cell and tissue biology.

The Folia Histochemica et Cytobiologica publishes papers that meet the needs and intellectual interests of medical professionals, basic scientists, college and university teachers and students. Prospective authors should read most recent issues of FHC to determine the appropriateness of a possible contribution. However, such an examination does not provide an infallible guide because editorial policy is always under review. Technical correctness is necessary, but it is not the only condition for acceptance. Clarity of exposition and potential interest of the readers are important considerations; it is the reader, not the author, who must receive the benefit of the doubt.

Folia Histochemica et Cytobiologica publishes review articles, original articles, short communications and proceedings of scientific congresses/symposia. Fields of particular interests include development and application of modern techniques in histochemistry and cell biology, cell biology and pathology, cell-microenvironment interactions, tissue organization and pathology.

Manuscripts announcing new theoretical or experimental results, or manuscripts questioning well-established and successful theories, are highly desirable and are a subject for evaluation by specialists. Manuscripts describing original research that clarifies past misunderstandings or allows a broader view of a subject are acceptable. Manuscripts that demonstrate new relations between apparently unrelated areas of fields of interests are appropriate. Manuscripts that show new ways of understanding, demonstrating, or deriving familiar results are also acceptable. Such manuscripts must provide some original cytobiological insight and not just a clever derivation.

Regularly, review or tutorial articles are published, often of a length greater than that of the average article. Most of these articles are a subject of a review; authors planning such articles are asked to consult with the editors at an early stage.

Most readers of a particular article will be specialists in the subject matter presented; the context within which the paper is presented should be established in the order given in Instructions for Authors. Manuscripts must be technically correct and must take proper cognizance of previous work on the same subject regardless of where it may have appeared. Such referencing is especially important for reminders of once well known ideas, proofs, or techniques that may have again become useful to readers. It is the responsibility of the author to provide adequate references; editors and referees will not do the literature search that should have been done by the authors. The references are a matter of review though.

Contributions considered include: Regular Articles (Papers), Short Communications, Review Articles, Conference Proceeding, Book Reviews and Technical Notes, which describe new laboratory methods or substantial improvements of the existing techniques. Regular articles should be about five journal pages or less in length. Short communications are usually confined to the discussion of a single concept and should be about two journal pages in length. Review articles are confined to a broad discussion and should contain the most recent knowledge about the subject.

Instructions concerning the preparation of manuscripts are given in the Information for Authors. Care in following those instructions will permit editors and referees to devote more time to thoughtful evaluation of contributions and will ultimately lead to a better, more interesting Journal.

Copying information, in part or in whole by any means is prohibited without a written permission from the owner.

SUBSCRIPTION

Folia Histochemica et Cytobiologica is available for paper subscription (print on demand).

To read and download articles for free as pdf document, visit https://journals.viamedica.pl/folia_histochemica_cytobiologica

Publisher: VM Media sp. z o.o. VM Group sp.k., Swietokrzyska St. 73, 80–180 Gdansk, <http://www.viamedica.pl>

Illustration on the cover: *CART (red), NPY (green); colocalization (gold/yellow) nerve cells and nerve fibers in the epicardium of chinchilla's right atrium* (see: Radzimirska M *et al.* pp. 157–166)

© Polish Society for Histochemistry and Cytochemistry



20-0869.003.001

Folia Histochemica et Cytobiologica

Scientific quarterly devoted to problems of histochemistry,
cytochemistry and cell & tissue biology

Vol. 59
No. 3
2021

https://journals.viamedica.pl/fovia_histochemica_cytobiologica

Official Journal of the Polish Society for Histochemistry and Cytochemistry

ORIGINAL PAPERS

Neuroanatomical distribution of the enkephalinergic and tachykininergic systems in the alpaca brainstem: an immunohistochemical study

Pablo Sánchez, Manuel Lisardo Sánchez, Arturo Mangas, Eliana de Souza¹, Luis Angel Aguilar, Rafael Coveñas 145

Distribution and neurochemical characteristic of the cardiac nerve structures in the heart of chinchilla (*Chinchilla laniger* Molina)

Malgorzata Radzimirska, Jacek Kuchinka, Tadeusz Kuder, Elzbieta Nowak, Wojciech Trybus, Grzegorz Wrobel, Aleksander Szczurkowski 157

Short-term fenofibrate treatment improves ultrastructure of hepatocytes of old rats

Adrian Zubrzycki, Agata Wronska, Agata Zauszkiewicz-Pawlak, Zbigniew Kmiec 167

Growth factors in the initial stage of bone formation, analysis of their expression in chondrocytes from epiphyseal cartilage of rat costochondral junction

Anna Hyc, Stanislaw Moskalewski, Anna Osiecka-Iwan 178

SDF-1/CXCR4 axis promotes osteogenic differentiation of BMSCs through the JAK2/STAT3 pathway

Wen Xiong, Xin Guo, Xianhua Cai 187

IL-39 increases ROS production and promotes the phosphorylation of p38 MAPK in the apoptotic cardiomyocytes

Wei Xiong, Hua Chen, Jiequan Lu, Jie Ren, Chen Nie, Ruijuan Liang, Feng Liu, Baofeng Huang, Yu Luo 195

Neuroanatomical distribution of the enkephalinergic and tachykininergic systems in the alpaca brainstem: an immunohistochemical study

Pablo Sánchez¹, Manuel Lisardo Sánchez¹, Arturo Mangas¹, Eliana de Souza¹,
Luis Angel Aguilar², Rafael Coveñas^{1,3}

¹Institute of Neuroscience of Castilla y León (INCYL), Laboratory of Neuroanatomy of the Peptidergic Systems (Lab. 14), University of Salamanca, Salamanca, Spain

²San Ignacio de Loyola University (USIL), Faculty of Health Sciences, Lima, Peru

³Grupo GIR USAL: BMD (*Bases Moleculares del Desarrollo*)

Abstract

Introduction. A recent study has shown a close neuroanatomical relationship between the enkephalinergic (methionine-enkephalin) and tachykininergic (substance P) systems in the alpaca diencephalon. In this study, our aim is to show this relationship in the alpaca brainstem.

Material and methods. Using an immunohistochemical technique, the distribution of immunoreactive (Ir) fibers and cell bodies containing substance P (SP) or methionine-enkephalin (MET) has been studied in the alpaca brainstem. Five adult males were used; brain tissue was fixed and processed by standard methods.

Results. SP- and MET-Ir fibers showed a widespread and similar distribution in the mesencephalon, pons and medulla oblongata. The co-localization of fibers containing SP or MET was found in most of the nuclei/tracts of the alpaca brainstem. This close neuroanatomical relationship suggests multiple physiological interactions between both neuropeptides. The distribution of the cell bodies containing SP was very restricted (cell bodies were only observed in a few nuclei located in the mesencephalon and medulla oblongata), whereas MET-Ir perikarya showed a moderately widespread distribution in the mesencephalon, pons and medulla oblongata.

Conclusions. This study increases the knowledge on the neuroanatomical distribution/relationship of the tachykininergic (SP) and enkephalinergic (MET) systems in the alpaca central nervous system. (*Folia Histochemica et Cytobiologica* 2021, Vol. 59, No. 3, 145–156)

Key words: substance P; methionine-enkephalin; mesencephalon; pons; medulla oblongata; *Lama pacos*, IHC

Introduction

The brainstem plays a fundamental role by conducting the information of the brain with the rest of the body and *vice versa* and, in addition, it integrates the

information of the cardiovascular/respiratory systems, is involved in pain perception and its motor neurons send outputs through the cranial nerves [1].

Many studies have been performed to know the distribution/function of substance P (SP) in the mammalian central and peripheral nervous systems [2]. SP belongs to the tachykinin family of peptides, like neurokinin A, and both peptides arise from the polyprotein precursor produced by differential splicing of the pre-protachykinin A gene [2]. SP, mainly *via* the neurokinin-1 receptor, plays many functional/pathophysiological roles in inflammation-associated vasodilation, pain perception, immune responses,

Correspondence address: Dr. Manuel Lisardo Sánchez
Universidad de Salamanca, Instituto de Neurociencias
de Castilla y León (INCYL)
Laboratorio de Neuroanatomía de los Sistema Peptidérgicos
(Lab. 14) c/Pintor Fernando Gallego, 1
37007-Salamanca, Spain
phone: +34 923294400 ext. 1856, fax: +34 923294549
e-mail: lisardosanchez8@gmail.com

This article is available in open access under Creative Common Attribution-Non-Commercial-No Derivatives 4.0 International (CC BY-NC-ND 4.0) license, allowing to download articles and share them with others as long as they credit the authors and the publisher, but without permission to change them in any way or use them commercially.

learning, nausea, stress, anxiety, cancer and depression [3, 4]. SP is widely distributed through the nervous system (*e.g.*, thalamus, hypothalamus, brainstem, spinal cord) [5–8].

Methionine-enkephalin (MET) is an opioid pentapeptide derived from the pro-enkephalin and pro-opiomelanocortin precursors after their proteolytic cleavage [9, 10]. MET is widely visualized through the central nervous system (CNS) of mammals (*e.g.*, cat, dog, monkey), suggesting the multiple physiological functions in which the peptide is involved [11–13]. Thus, MET has been located in nervous system regions involved in the transmission and control of pain messages (*e.g.*, thalamus, brainstem reticular formation, raphe nuclei, periaqueductal gray, spinal cord). MET is also involved in analgesia, stress, respiratory and cardiovascular mechanisms, feeding behavior, peristalsis and memory [14].

The ungulate alpaca (*Lama pacos*) belongs to the family of Camelidae which is a member of the order Artiodactyla. The alpaca has precious wool that is greatly demanded for producing a high quality fiber. Due to the economic importance, many studies have been focused on the hormonal processes involved in reproductive mechanisms [15, 16]. Alpacas can live from the sea level to 5,000 m altitude, indicating that this species has special physiological adjustment mechanisms, as are those related to providing sufficient blood flow to the brain and the implication of these unique features in the neuroanatomical organization of some CNS nuclei. In addition to those works focused on the alpaca reproductive mechanisms, several studies have been previously performed on the neuroanatomical location of neuropeptides (calcitonin gene-related peptide, somatostatin-28 (1-12), neurotensin, leucine-enkephalin, alpha-neo-endorphin, adrenocorticotrophic hormone (18-39), beta-endorphin (1-27)) in the alpaca brainstem [17–22]. In addition, a recent study has shown a close neuroanatomical relationship between the enkephalinergic (methionine-enkephalin) and tachykinergic (substance P) systems in the alpaca diencephalon and the presence of some neuropeptides (*e.g.*, neurotensin) has also been reported in this region of the alpaca CNS [5, 23]. To our best knowledge no immunohistochemical study on the distribution of SP and MET has been carried out in the alpaca brainstem. Therefore, the main goal of this work is to study, for the first time, the presence of immunoreactive structures containing SP/MET in the alpaca brainstem and to know whether in this brain region a close neuroanatomical relationship between both systems occurs, in addition to the diencephalon. Another goal is to compare the distribution of both peptides with that described for

other neuropeptides in the alpaca brainstem and to compare the presence of SP/MET in the alpaca with the presence observed for both peptides in the same brain region of other mammals.

Material and methods

Animals. As previously reported [5], the use of animals in this study along with procedures of their maintenance, experimental design, protocols and methodology were carried out according to the principles of laboratory animal care and performed under the advices of the ethical and legal guidance of Peruvian and Spanish laws. This work was as well approved by the Research Commission of the Cayetano Heredia Peruvian University (Lima, Peru). Because previous studies on the distribution of neuropeptides were carried out in males [17–22] and, in order to compare the results observed here with previous works performed in the alpaca brainstem [17–22], the present study was carried out in male alpacas. Five adult alpacas (*Lama pacos*) (70–80 kg; 5–8 years) were obtained from the Cayetano Heredia Peruvian University (Faculty of Veterinary Medicine and Animal Sciences). As previously reported [17–22], alpacas were maintained at 0 m altitude, under standard conditions of temperature and lightning and were provided with free access to food and water and, from birth to the moment of the perfusion; animals were kept at sea level.

Tissue preparation. As previously reported [5, 17–20], animals were deeply anesthetized with ketamine (10 mg/kg) and xylazine (4 mg/kg) both administered intravenously. Afterwards, they were heparinized and perfused with 3 L of cold NaCl (0.9%) through the carotid artery. This pre-rinse was straight away followed by infusion of the fixative: 5 L of cold paraformaldehyde (4%) diluted in 0.15 M phosphate-buffered saline (PBS) (pH 7.2). Once brainstems were dissected out, they were post-fixed overnight in the same fixative solution and cryoprotected, via immersion in sucrose solutions at increasing concentrations (10–30%), until they sank. Making use of a cryostat, frontal sections were cut (50 μ m) and kept in PBS at 4°C. Two of six sections were used for immunohistochemistry: section 1, for anti-MET staining; section 2, for Nissl staining to identify/delimited the brainstem nuclei or for histological controls; section 3, for anti-SP staining; sections 4–6 were kept for other experimental purposes. The distance between sections 1 and 7 (and so on, kept in the same container) was about 300 μ m. Thus, sections kept in containers 1 and 3 were respectively used for anti-MET and anti-SP. In each container, 55–60 frontal sections/animal were collected.

Immunohistochemistry and specificity of the antisera. As formerly reported [5, 17–20] and to prevent possible interference with endogenous peroxidase, free-floating sections were treated with a mixture of NaOH, NH₃ and H₂O₂ (20 min).

Sections were then washed with PBS (3 × 10 min) and to improve antibody penetration free-floating sections were pre-incubated (30 min) in a PBS solution containing normal horse serum (1%) and Triton X-100 (0.3%). Then, sections were incubated overnight (4°C) in the latter solution supplemented with anti-SP antiserum (1/3,000) or anti-MET antiserum (1/3,000). Sections were washed in PBS (30 min) and incubated (1 h) in biotinylated anti-rabbit IgG (1/200). Later, sections were treated (1 h) with Vectastain ABC reagent (1/100) and washed in PBS (30 min) and Tris-HCl buffer (pH 7.6; 10 min). Finally, the tissue bound peroxidase was developed (using H₂O₂ and 3, 3'-diaminobenzidine as chromogen), sections were rinsed (PBS) and coverslipped with PBS and glycerol (1/1).

The polyclonal primary antibodies used here (anti-SP; anti-MET; obtained at the laboratory of Professor Gérard Tramu, University of Bordeaux I, France), were raised in rabbits against immunogens assembled by coupling the full synthetic SP or MET to a carrier protein (human serum albumin) with glutaraldehyde, as formerly reported [5, 13, 24]. Rabbits were immunized with immunogens emulsified with Freund's complete adjuvant and provided with booster doses of Freund's incomplete adjuvant at intervals of two weeks. Ten days, after three of such booster injections, plasma from rabbits was obtained and periodically thereafter. To avoid non-specific immunoreactivity due to the anticarrier antibodies, rabbit antisera were preabsorbed with the coupling agent and the carrier protein, being this preabsorption performed prior to the immunohistochemical technique. The immunological properties of the anti-SP and anti-MET antisera have been previously reported [5, 10, 13, 25, 26]. The anti-MET used in this study was purified by affinity chromatography [5, 10, 13]. In addition, in this study, three histological controls were performed. Thus, primary antibody was treated with an excess (100 µg/ml of diluted antiserum) of the same synthetic antigen (*e.g.*, MET to anti-MET serum) and the first antiserum was omitted in the first incubation bath (no immunoreactivity was found in both cases). Moreover, primary antibodies were preabsorbed with heterologous antigens (*e.g.*, neurokinin A to anti-SP serum; leucine-enkephalin to anti-MET serum): this preabsorption did not block the staining.

Mapping. This was performed by following frontal planes of the alpaca brainstem (the brain atlas used here is available from the Mammalian Brain Collections of the University of Wisconsin, Madison, USA). For mapping and nomenclature of the brainstem nuclei, we also followed previous published works performed in this camelid [17–22]. In addition, contiguous sections to those reacted for SP or MET were stained with cresyl violet to delineate the brainstem nuclei in which immunoreactive structures were observed.

As previously reported [5, 17–22], immunoreactive fibers were graded into four categories: single (a few immunoreac-

tive fibers; Fig. 2b), low, moderate (Fig. 2d) and high (Fig. 4b, d). To determine the density of the immunoreactive fibers, sections were viewed (at a constant magnification) with reference to photographs in which low, moderate or high densities were previously determined [5, 17–22]. The density of the immunoreactive cell bodies was considered high (> 20 perikarya/section), moderate (10–20 perikarya/section) and low (< 10 perikarya/section). Immunoreactive cell bodies size was measured following the protocol described by Marcos *et al.* [24]. Using a micrometer grid, the size of cell bodies was measured with the nucleus in the focal plane, and, as previously reported [5, 17–22], cell bodies with < 15 µm diameter were considered small, perikarya with a diameter between 15–25 µm were contemplated as medium sized, and those with a > 25 µm diameter were considered large.

Using an Olympus DP-50 digital camera (Olympus, Tokyo, Japan) attached to a Kyowa Unilux 12 microscope (Kyowa Optical, Sagamihara, Japan), photomicrographs were taken. Adobe Photoshop CS6 software was used to adjust contrast and brightness.

Results

General considerations

Figures 1–4 and Table 1 show the presence and density of the immunoreactive structures (fibers and cell bodies) containing SP/MET observed in 44 tracts/nuclei of the alpaca brainstem. SP- and MET-immunoreactive fibers showed a widespread distribution. Thus, SP-immunoreactive fibers were observed in 42 (95.45%) of 44 tracts/nuclei, whereas fibers containing MET were found in 41 of them (93.18%). In the mesencephalon, SP- and MET-immunoreactive fibers were visualized in all tracts/nuclei (13 of 13, 100%); in the pons, in 13 of 13 tracts/nuclei (for SP-immunoreactive fibers, 100%) and in 12 of 13 (for MET-immunoreactive fibers, 92.30%), and in the medulla oblongata in 16 tracts/nuclei of 18 (88.88%) for both SP- and MET-immunoreactive fibers. Thus, in the brainstem, the distribution of SP- and MET-immunoreactive fibers was similar (Fig. 1; Table 1). This means that a close neuroanatomical relationship between SP- and MET-immunoreactive fibers occurs. Finally, in the alpaca brainstem, the density of the SP-immunoreactive fibers is a little higher when compared with the density observed for the MET-immunoreactive fibers (Fig. 1; Table 1).

In the alpaca brainstem, MET-immunoreactive perikarya were observed in 22 of the 44 brainstem nuclei (50%), whereas cell bodies containing SP were visualized in 3 nuclei (6.81%). In the mesencephalon, SP-immunoreactive cell bodies were found in 2 nuclei (15.38%) and those containing MET in

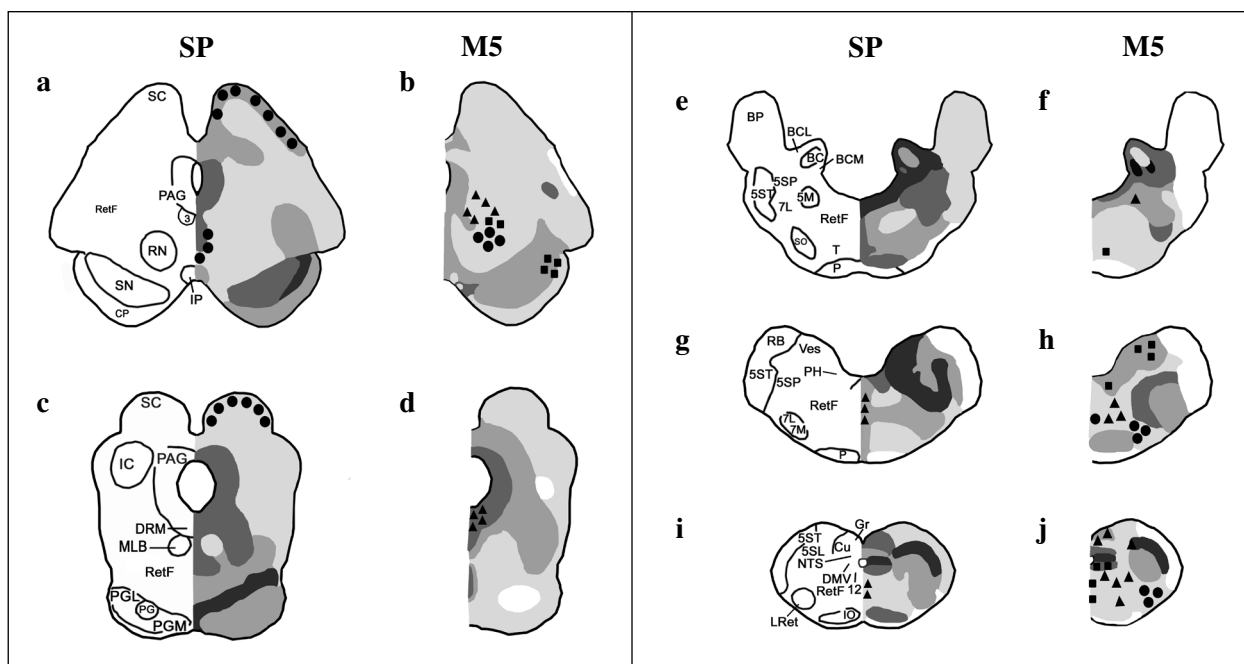


Figure 1. Distribution of substance P (SP) and methionine-enkephalin (M5)-immunoreactive fibers and cell bodies in frontal planes of the alpaca brainstem (a–j) from rostral (a) to caudal (j) levels. Cell bodies containing the peptides are represented by closed circles (high density), triangles (moderate density) and squares (low density), whereas immunoreactive fibers are represented by slightly dark (single axons), moderately dark (low density), strongly dark (moderate density), and black (high density). 3 — oculomotor nucleus; 4 — trochlear nucleus; 12 — hypoglossal nucleus; 5M — motor trigeminal nucleus; 5SL — laminar spinal trigeminal nucleus; 5SP — alaminar spinal trigeminal nucleus, parvocellular division; 5ST — spinal trigeminal tract; 7L — facial nucleus, lateral division; 7M — facial nucleus, medial division; AP — area postrema; BC — brachium conjunctivum; BCL — marginal nucleus of the brachium conjunctivum, lateral division; BCM — marginal nucleus of the brachium conjunctivum, medial division; BP — brachium pontis; CAE — locus coeruleus; CP — cerebral peduncle; Cu — cuneate nucleus; Cx — external cuneate nucleus; Cuc — cuneate nucleus, caudal division; DMV — motor dorsal nucleus of the vagus; DRM — dorsal nucleus of the raphe; Gr — gracile nucleus; IC — inferior colliculus; IO — inferior olive; IP — interpeduncular nucleus; LRet — lateral reticular nucleus; MLB — medial longitudinal bundle; NTS — nucleus of the solitary tract; P — pyramidal tract; PAG — periaqueductal gray; PG — pontine gray; PGL — pontine gray, lateral division; PGM — pontine gray, medial division; PH — nucleus praepositus hypoglossi; RB — restiform body; RetF — reticular formation; RN — red nucleus; S — solitary tract; SC — superior colliculus; SN — substantia nigra; SO — superior olive; T — nucleus of the trapezoid body; Ves — vestibular nuclei.

7 nuclei (53.84%); in the pons no immunoreactive cell body containing SP was observed, whereas in 5 nuclei (38.46%) MET-immunoreactive perikarya were visualized, and in the medulla oblongata cell bodies were found in one nucleus (for SP, 5.55%) and in 10 nuclei (for MET, 55.55%). Thus, in the alpaca brainstem the distribution and number of cell bodies containing MET is higher than those containing SP. The morphological characteristics of the MET- and SP-immunoreactive cell bodies (size, shape, number of dendrites) are shown in Table 2. In general, in the five alpacas studied the density and distribution of the MET- and SP-immunoreactive cell bodies and fibers observed in the brainstem were quite similar.

It is important to note that in different regions of the same nucleus, two densities (e.g., moderate and high; single and low) can be observed (Table 1). In

these cases, to obtain the percentages appearing below the highest density was chosen.

Mesencephalon

MET-immunoreactive cell bodies were observed in the oculomotor nucleus, trochlear nucleus, dorsal nucleus of the raphe, periaqueductal gray, reticular formation, red nucleus and substantia nigra, whereas SP-immunoreactive cell bodies were found in the superior colliculus and reticular formation (Figs. 1, 2b, c, g, 3b; Table 1).

Fibers containing SP or MET were observed in all mesencephalic tracts/nuclei and hence a similar distribution of both immunoreactive fibers was visualized (Figs. 1, 2d–f, 3c–g; Table 1). Single SP- and MET-immunoreactive fibers were respectively found in 2 (15.38%) and 4 (30.76%) tract/nuclei; a low density in 3 tracts/nuclei (for both neuropeptides,

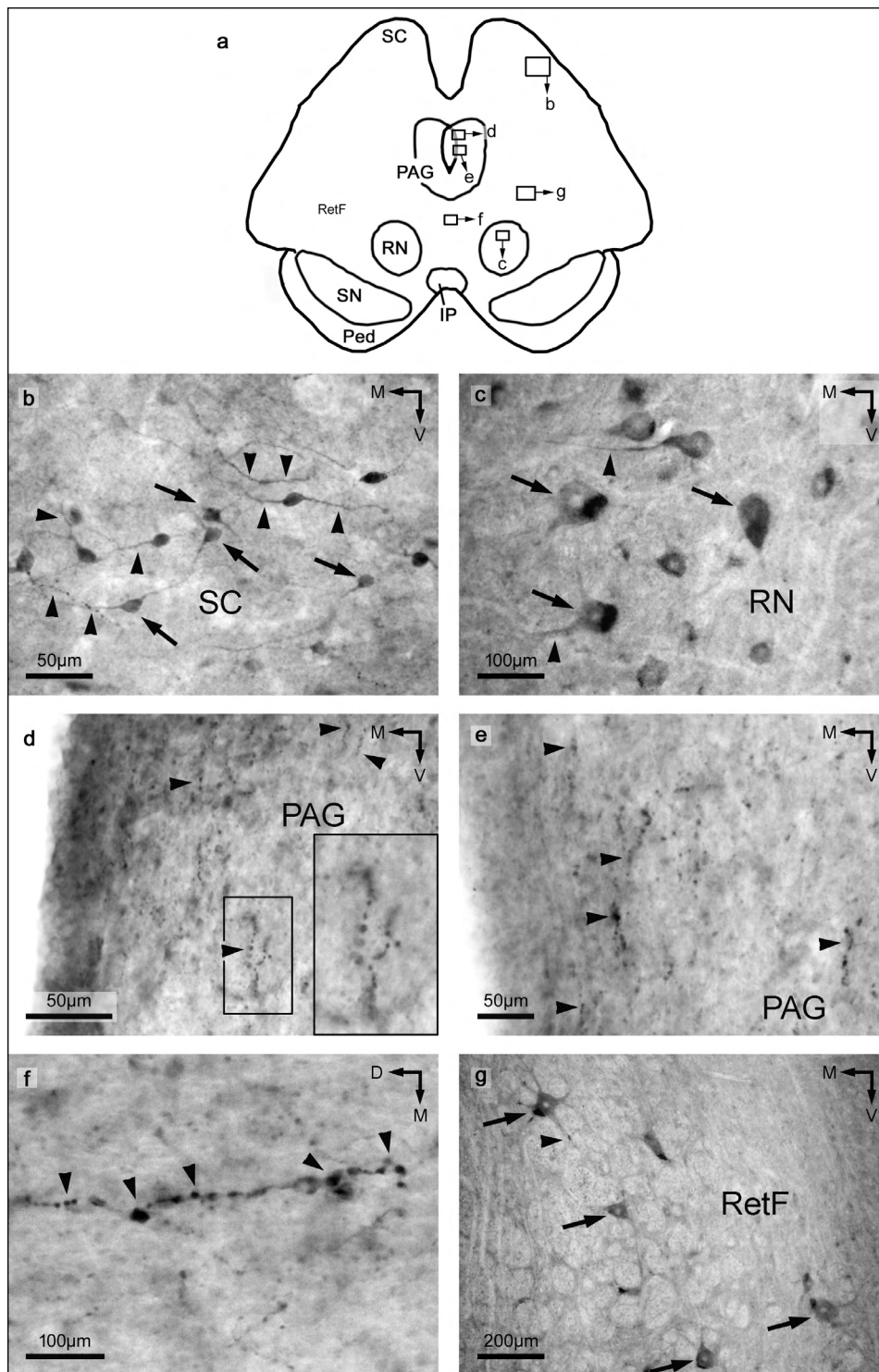


Figure 2. SP- and MET-immunoreactive (Ir) cell bodies and fibers/dendrites in the alpaca mesencephalon. **A.** Frontal section of the alpaca mesencephalon. For the nomenclature of the nuclei, see Figure 1. The photographs shown in b–g were taken from the regions delimited by the rectangles in a (indicated as Fig. b, c, d, e, f and g). **B.** SP-Ir cell bodies (arrows) located in the superior colliculus (SC). Arrowheads: fibers or dendrites. **C.** MET-Ir cell bodies (arrows) located in the red nucleus (RN). Arrowheads: dendrites. **D.** SP-Ir fibers (arrowheads) located in the periaqueductal gray (PAG). The region delimited by the left rectangle is shown at higher magnification. **E.** MET-Ir fibers (arrowheads) in the periaqueductal gray (PAG). **F.** SP-Ir fibers (arrowheads) located in the midline. **G.** MET-Ir cell bodies (arrows) in the reticular formation (RetF). Arrowhead: dendrite. D — dorsal; M — medial. V — ventral.

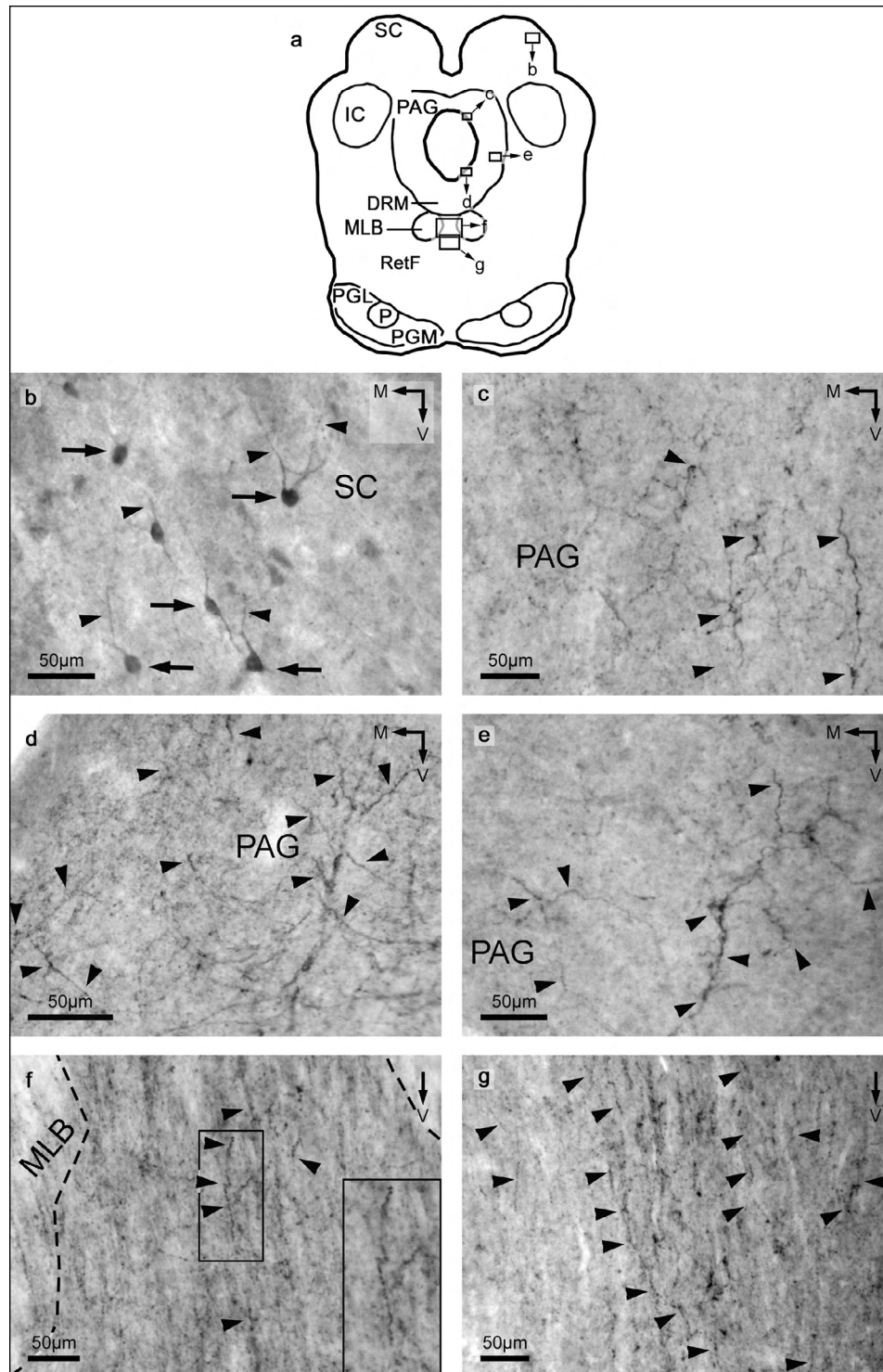


Figure 3. Immunoreactive (Ir) fibers/dendrites and cell bodies containing SP or MET in the alpaca mesencephalon. **A.** Frontal section of the alpaca mesencephalon. For the nomenclature of the nuclei, see Figure 1. The photographs shown in b–g were taken from the regions delimited by the rectangles in a (indicated as Fig. b, c, d, e, f and g). **B.** SP-Ir cell bodies (arrows) located in the superior colliculus (SC). Arrowheads: dendrites. **C.** MET-Ir fibers (arrowheads) in the periaqueductal gray (PAG). **D.** SP-Ir fibers (arrowheads) located in the periaqueductal gray (PAG). **E.** MET-Ir fibers (arrowheads) located in the periaqueductal gray (PAG). **F.** SP-immunoreactive fibers (arrowheads) in the upper midline. The region delimited by the left rectangle is shown at higher magnification. MLB: medial longitudinal bundle. **G.** MET-Ir fibers (arrowheads) in the midline. M — medial. V — ventral.

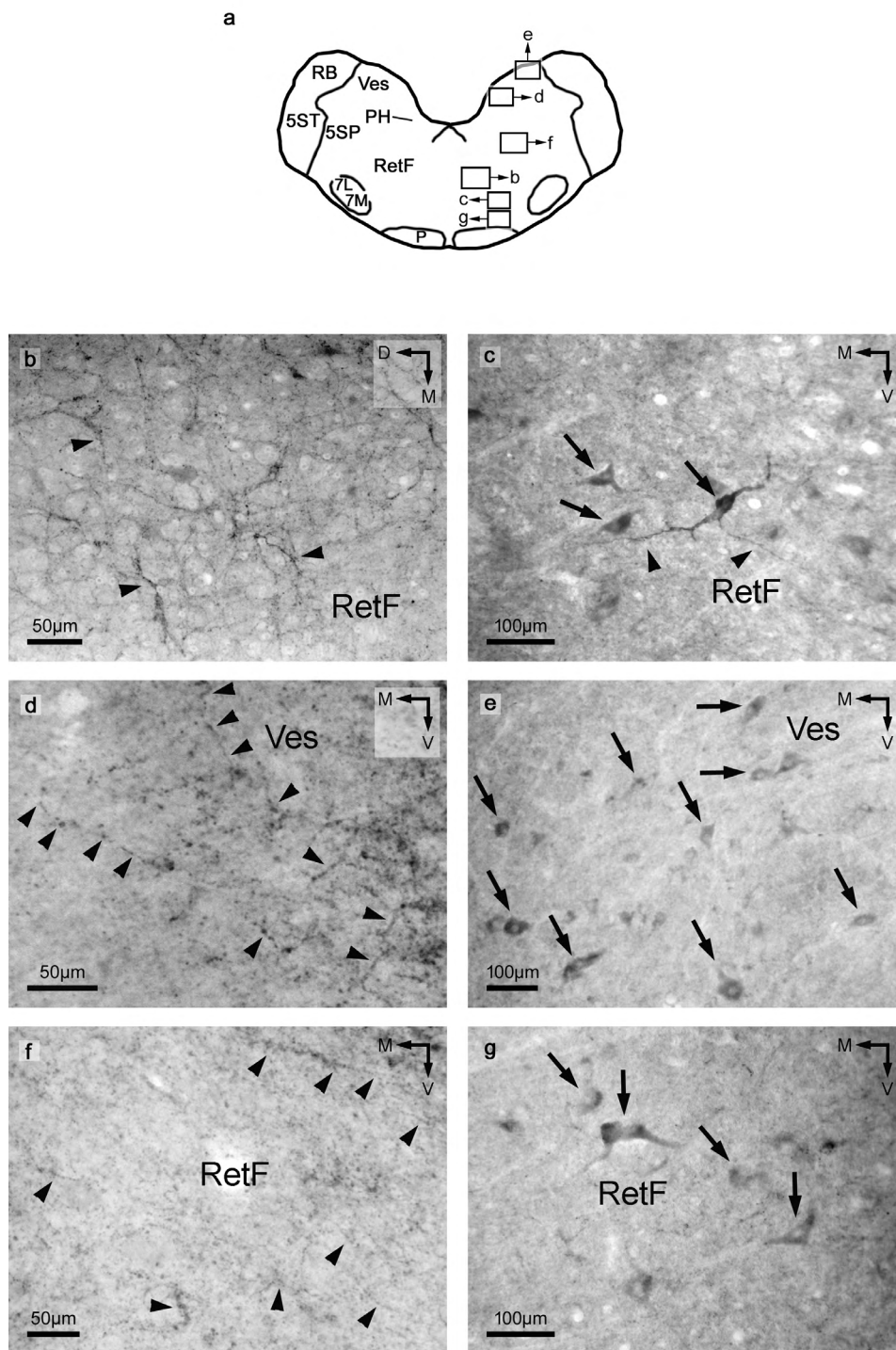


Figure 4. SP- and MET-immunoreactive (Ir) fibers/dendrites and cell bodies in the alpaca medulla oblongata. **A.** Frontal section of the alpaca medulla oblongata. For the nomenclature of the nuclei, see Figure 1. The photographs shown in b-g were taken from the regions delimited by the rectangles in a (indicated as Fig. b, c, d, e, f and g). **B.** SP-Ir fibers (arrowheads) located in the reticular formation (RetF). **C.** MET-Ir cell bodies (arrows) in the reticular formation (RetF). Arrowheads: dendrites. **D.** SP-Ir fibers (arrowheads) located in the vestibular nuclei (Ves). **E.** MET-Ir cell bodies (arrows) located in the vestibular nuclei (Ves). **F.** SP-Ir fibers (arrowheads) in the reticular formation (RetF). **G.** MET-Ir cell bodies (arrows) in the reticular formation (RetF). D — dorsal. M — medial. V — ventral.

Table 1. Alpaca brainstem: distribution and density of SP- and MET-immunoreactive cell bodies and fibers

Mesencephalon				
Nucleus	SP		MET	
	CB	Fibers	CB	Fibers
3	-	++	++	s/+
4	-	++	+++	s
BC	-	+	-	s
BCL	-	+++	-	++
BCM	-	+++	-	++/+++
DRM	-	++	++	++
IC	-	s	-	s/+
IP	-	+	-	s/+++
PAG	-	++	+ /+++	+ /+++
RetF	+++	s/++	+ /+++	s/+
RN	-	s	+++	s
SC	+++	s/+	-	s
SN	-	++ /+++	++	+ /++
Pons				
Nucleus	SP		MET	
	CB	Fibers	CB	Fibers
5M	-	++	+	+
5SP	-	+ /+++	++	s/++
7L	-	+ /++	+++	s
7M	-	+	+++	s
BP	-	s	-	-
CAE	-	++ /+++	-	s
MLB	-	s	-	s
PG	-	+	-	s
PGL	-	+	-	s

→

Nucleus	SP		MET	
	CB	Fibers	CB	Fibers
12	-	++	++	+ /+++
5SL	-	+++	+	s/+++
5ST	-	s	-	s
AP	-	++	-	+++
Cu	-	++	+	s
Cuc	-	+	+++	s
Cx	-	++	++	s
DMV	-	+++	-	+++
Gr	-	++	+	+
IO	-	++	-	s
LRet	-	+	+++	s
NTS	-	+	-	++
P	-	-	-	-
PH	-	++	++	+
RB	-	-	-	-
RetF	+ /+++	s/+++	+ /+++	s/++
S	-	s	-	s
Ves	-	+ /+++	+ /+++	s/+

CB — cell bodies (+++: high density; ++: moderate density; +: low density; -: no immunoreactivity). Fibers (+++: high density; ++: moderate density; +: low density; s: single; -: no immunoreactivity). For nomenclature of the nuclei, see list of abbreviations.

23.07%); a moderate density in 5 (38.46%) and 4 (30.76%) mesencephalic nuclei, and a high density in 3 (23.07%) and 2 (15.38%) nuclei (Table 1).

Pons

No immunoreactive cell body containing SP was observed, whereas perikarya containing MET were found in the motor trigeminal nucleus, alaminar spinal trigeminal nucleus (parvocellular division), lateral and medial divisions of the facial nucleus and nucleus of the trapezoid body (Fig. 1; Table 1).

SP- and MET-immunoreactive fibers showed a similar distribution in the alpaca pons, although the density of the fibers containing MET was lower than that observed for SP (Fig. 1; Table 1). Thus, single SP- and MET-immunoreactive fibers were respectively found in 2 (15.38%) and 8 (61.53%) tracts/nuclei;

a low density in 5 (38.46%) and 1 (7.69%) nuclei; a moderate density in 3 pons nuclei (for both neuropeptides, 23.07%), and a high density in 3 (23.07%) and 0 nuclei (Fig. 1; Table 1).

Medulla oblongata

Cell bodies containing SP were only observed in the reticular formation, whereas MET-immunoreactive perikarya were found in the external cuneate nucleus, lateral reticular nucleus, reticular formation, vestibular nuclei, cuneate nucleus, hypoglossal nucleus, laminar spinal trigeminal nucleus, caudal division of the cuneate nucleus, gracilis nucleus and nucleus praepositus hypoglossi (Figs. 1, 4c, e, g; Table 1).

The distribution of fibers containing SP or MET was similar. Both peptides were absent in the pyramidal tract and restiform body, but in the other 16 tracts/

Table 2. Alpaca brainstem: morphological characteristics of the MET- and SP-immunoreactive cell bodies

Nucleus	Density	Size	Shape	Dendritic processes
MET- immunoreactive cell bodies				
3	++	Medium	Pyriform, oval	0–1
4	+++	Medium	Pyriform, oval	0–1
5M	+	Large	Polygonal	2–3
5SL	+	Large	Polygonal	2
5SP	++	Large	Oval	1
7L	+++	Medium	Oval	1
7M	+++	Medium	Oval	1
12	++	Medium	Oval	1
Cu	+	Medium	Polygonal, oval	1–2
Cuc	+++	Medium	Polygonal, oval	1–2
Cx	++	Medium	Polygonal, oval	1–2
DRM	+++	Small	Oval	0–1
Gr	+	Medium	Oval	0–1
LRet	+++	Large	Polygonal	2–3
PAG	++	Small	Pyriform, oval	1
PH	++	Large	Polygonal	2–3
RetF	+++	Large	Polygonal, oval	1–4
RN	+++	Large	Pyriform	1
SN	++	Medium	Oval	1–2
T	++	Medium	Oval	1
Ves	+++	Medium	Oval	1–2
SP- immunoreactive cell bodies				
RetF	+ / + + / + + + +	Large	Pyriform, polygonal	1–4
SC	+++	Small	Oval	2

+++ : high density; ++ : moderate density; + : low density. For nomenclature of the nuclei, see list of abbreviations.

/nuclei immunoreactive fibers containing SP or MET were observed (Figs. 1, 4b, d, f; Table 1). Single SP- and MET-immunoreactive fibers were respectively found in 2 (11.11%) and 7 (38.88%) tracts/nuclei; a low density in 3 nuclei (for both neuropeptides, 16.66%); a moderate density in 7 (38.88%) and 3 (16.66%) tracts/nuclei, and a high density in 4 (22.22%) and 3 (16.66%) nuclei (Fig. 1; Table 1).

Discussion

SP and MET in the alpaca brainstem

For the first time, this study shows the mapping of the SP- and MET-immunoreactive cell bodies and fibers in the alpaca brainstem. The study increases the knowledge on the enkephalinergic and tachykinergic systems in the alpaca CNS, since a previous study has been reported on the distribution of SP and MET in the alpaca diencephalon

[5]. In both alpaca brainstem and diencephalon [5] a close neuroanatomical relationship between the tachykinergic (SP) and the enkephalinergic (MET) systems has been observed. This means that a functional relationship between both systems could also occur in both regions of the alpaca CNS and that mechanisms of intercellular communication (e.g., paracrine mechanism and/or synaptic contacts) between the enkephalinergic and tachykinergic systems, controlling many brainstem physiological actions, are possible. Moreover, in the mesencephalon, pons and medulla oblongata the presence of MET-immunoreactive perikarya is more widespread than that observed for cell bodies containing SP. This is in agreement with that reported in the alpaca diencephalon, in which the distribution of MET-immunoreactive cell bodies was also more widespread than that observed for cell bodies containing SP [5]. In addition, in the alpaca brainstem and diencephalon

the number of cell bodies containing MET was higher than those containing SP.

The widespread distribution of the SP- and MET-immunoreactive structures in the alpaca brainstem suggests that both neuropeptides are involved in many physiological actions, in which SP and MET could interact. To date, the mechanisms of possible intercellular mechanisms between SP and MET are unknown, but this could occur through synaptic contacts and/or paracrine (volume transmission) mechanisms [5]. In the latter, neuropeptides are released into the extracellular region and diffuse longer distances until reaching their receptors; this is a slow mode of communication showing a high divergence degree [27]. In addition, neuropeptides could exert an autocrine mechanism. The brainstem has a key role in the relay of information between the brain and the spinal cord and it is known that some nuclei (*e.g.*, periaqueductal gray, reticular formation, spinal trigeminal nucleus) are essential in the transmission of the nociceptive perception [28, 29]. In these nuclei both SP- and MET-immunoreactive structures have been observed and hence a neuroanatomical linkage between the transmission of pain via SP and the control of the pain stimuli via MET could occur. Moreover, the observation of cell bodies containing SP or MET in the rat lateral mammillary nucleus suggests that the neuropeptides are involved in head-direction and angular velocity [30], whereas the presence of a high density of SP-immunoreactive fibers in the locus coeruleus and superior colliculus indicates that SP is involved in arousal, anxiety, memory and in visual mechanisms [31–34]. Finally, the presence of SP- and MET-immunoreactive fibers in the alpaca area postrema, nucleus of the solitary tract, marginal nucleus of the brachium conjunctivum and motor dorsal nucleus of the vagus suggests that the neuropeptides studied here could be involved in emesis and in cardiovascular/respiratory mechanisms.

Neuropeptides in the alpaca brainstem

In the alpaca brainstem, the presence of immunoreactive structures containing leucine-enkephalin, calcitonin gene-related peptide, neurotensin, somatostatin, alpha-neo-endorphin, beta-endorphin or adrenocorticotrophic hormone has been previously reported [17–20, 22]. Peptidergic immunoreactive fibers (including those containing SP or MET) showed a widespread distribution in the whole brainstem. In addition, the location of the previous nine neuropeptides is similar. Thus, in many nuclei of the alpaca mesencephalon, pons and medulla oblongata (*e.g.*, laminar spinal trigeminal nucleus, parvocellular division of the alaminar spinal trigeminal nucleus, medial

division of the facial nucleus, marginal nucleus of the brachium conjunctivum, nucleus of the solitary tract, periaqueductal gray, superior colliculus, substantia nigra), the presence of immunoreactive fibers containing the nine neuropeptides has been reported [17–20, 22]. Although the distribution of the peptidergic fibers observed in the alpaca brainstem is widespread, it is important to note that in most of the brainstem nuclei single fibers containing beta-endorphin or adrenocorticotrophic hormone were observed [22]. To date, our study shows the most widespread presence of peptidergic cell bodies found in the alpaca brainstem: MET-immunoreactive perikarya were located in 22 nuclei. No immunoreactive cell body containing alpha-neo-endorphin, beta-endorphin or adrenocorticotrophic hormone has been reported in the alpaca brainstem [22]. Peptidergic immunoreactive cell bodies containing somatostatin or calcitonin gene-related peptide were observed in 13 and 12 brainstem nuclei, respectively; those containing neurotensin in five of them and those containing SP or leucine-enkephalin in two brainstem nuclei [17–20]. In the periaqueductal gray and in the reticular formation, the presence of five neuropeptides (leucine-enkephalin, somatostatin, neurotensin, MET, calcitonin gene-related peptide or SP) has been observed in cell bodies [17–20]. Because colchicine was not used in this and previous studies, it seems that the distribution of the peptidergic cell bodies in the alpaca brainstem may be more widespread. To know this distribution, other neuroanatomical studies applying for example *in situ* hybridization techniques should be performed.

SP and MET in the mammalian brainstem

Many studies focused on the distribution of SP and MET in the mammalian brainstem have been carried out [1, 2, 10–13, 25, 35, 36]. In general, the widespread distribution of the MET-immunoreactive fibers found in the alpaca brainstem is quite similar to that reported in other mammals in the same CNS region. However, some differences occur. The presence of fibers containing MET was similar in the alpaca, minipig [10] and monkey [25] brainstem and this distribution was a slight more widespread than that found in the dog [13] brainstem. Many differences can be observed when comparing the location of the MET-immunoreactive perikarya in the mammalian brainstem. These differences are due to the methodology applied (administration of colchicine; as indicated above, this drug is used to increase the number of peptidergic cell bodies). In general, in animals treated with colchicine a widespread presence of immunoreactive cell bodies was observed. For example, in rats [37] and dogs [13] treated with colchicine, a widespread distribution of

cell bodies containing MET was observed in both species. However, here, this widespread distribution was not observed in the brainstem of alpacas not treated with colchicine. When comparing the presence of MET-immunoreactive perikarya in the brainstem of animals not treated with colchicine, for example, alpaca, minipig and monkey [10, 25], this distribution was also different. In this case, the alpaca brainstem showed a more widespread distribution of cell bodies containing MET than that observed in the minipig [10] and the latter species showed a more widespread distribution than that found in the monkey brainstem [25]. In summary, in comparison with other mammals, the presence of MET-immunoreactive cell bodies is moderate in the alpaca brainstem (MET-immunoreactive perikarya were observed in 22 of the 44 brainstem nuclei of the alpaca). Finally, in the alpaca and human brainstem, the presence of SP-immunoreactive fibers was widespread and similar, whereas the distribution of perikarya containing SP was a slightly more widespread in humans [38].

In summary, this study increases the knowledge on the neuroanatomical distribution of the tachykinergic (SP) and enkephalergic (MET) peptidergic systems in the alpaca brainstem. SP- and MET-immunoreactive fibers showed a widespread and similar distribution in the brainstem. This close neuroanatomical relationship suggests multiple physiological interactions between both neuropeptides. The presence of cell bodies containing SP was very restricted, whereas MET-immunoreactive perikarya showed a moderate widespread distribution in the mesencephalon, pons and medulla oblongata. The mapping of SP and MET will help to understand their functional relationships with other neuropeptides previously studied in the alpaca brainstem and this knowledge will serve to better understand the involvement of the peptidergic systems in multiple brainstem physiological functions (*e.g.*, the adaptation to a high altitude). Moreover, our study increases the knowledge on the peptidergic chemical neuroanatomy (enkephalergic and tachykinergic systems) in the alpaca CNS, since as indicated above, the presence of both neuropeptides has previously been reported in the alpaca diencephalon [5].

Acknowledgements

The authors wish to thank Professor Gérard Tramu (Université de Bordeaux I, Bordeaux, France) for the gift of primary antibodies and the Language Service of the Universidad de Salamanca (Spain) for supervising the English text. This work has been supported by “Programa XI: Financiación de Unidades de Excelencia de la Universidad de Salamanca” (Spain).

References

1. Coveñas R, Belda M, Marcos P, et al. Neuropeptides in the cat brainstem. *Curr Top Pept Protein Res.* 2003; 5: 41–61.
2. Graefe S, Mohiuddin SS. *Biochemistry, substance P.* StatPearls Publishing: Treasure Island; 2021., indexed in Pubmed: [32119470](#).
3. Ebner K, Muigg P, Singewald G, et al. Substance P in stress and anxiety: NK-1 receptor antagonism interacts with key brain areas of the stress circuitry. *Ann N Y Acad Sci.* 2008; 1144: 61–73, doi: [10.1196/annals.1418.018](#), indexed in Pubmed: [19076365](#).
4. Mashaghi A, Marmalidou A, Tehrani M, et al. Neuropeptide substance P and the immune response. *Cell Mol Life Sci.* 2016; 73(22): 4249–4264, doi: [10.1007/s00018-016-2293-z](#), indexed in Pubmed: [27314883](#).
5. Sánchez P, Sánchez ML, Mangas A, et al. A close neuroanatomical relationship between the enkephalergic (methionine-enkephalin) and tachykinergic (substance P) systems in the alpaca diencephalon. *Folia Histochem Cytobiol.* 2020; 58(2): 135–146, doi: [10.5603/FHC.a2020.0007](#), indexed in Pubmed: [32412087](#).
6. Duque-Díaz E, Coveñas R. Distribution of somatostatin-28 (1-12), calcitonin gene-related peptide, and substance P in the squirrel monkey brainstem: an immunocytochemical study. *Anat Sci Int.* 2019; 94(1): 86–100, doi: [10.1007/s12565-018-0453-y](#), indexed in Pubmed: [30051271](#).
7. Polgár E, Bell AM, Gutierrez-Mecinas M, et al. Substance P-expressing neurons in the superficial dorsal horn of the mouse spinal cord: insights into their functions and their roles in synaptic circuits. *Neuroscience.* 2020; 450: 113–125, doi: [10.1016/j.neuroscience.2020.06.038](#), indexed in Pubmed: [32634530](#).
8. Luu A, Oberdoerster Z, Grignol G, et al. Presence of substance P positive terminals on hypothalamic somatostatinergic neurons in humans: the possible morphological substrate of the substance P-modulated growth hormone secretion. *Brain Struct Funct.* 2020; 225(1): 241–248, doi: [10.1007/s00429-019-01990-x](#), indexed in Pubmed: [31807924](#).
9. Peinado JR, Li H, Johanning K, et al. Cleavage of recombinant proenkephalin and blockade mutants by prohormone convertases 1 and 2: an in vitro specificity study. *J Neurochem.* 2003; 87(4): 868–878, doi: [10.1046/j.1471-4159.2003.02043.x](#), indexed in Pubmed: [14622118](#).
10. Sánchez ML, Vecino E, Coveñas R. Distribution of methionine-enkephalin in the minipig brainstem. *J Chem Neuroanat.* 2013; 50-51: 1–10, doi: [10.1016/j.jchemneu.2013.03.002](#), indexed in Pubmed: [23538385](#).
11. Duque E, Mangas A, Díaz-Cabiale Z, et al. Neuropeptides in the monkey brainstem. In: Williams RM, ed. *Monkeys: Biology, Behavior and Disorders.* Nova Science Publisher: New York; 2011: 151–166.
12. Marcos P. Neuropeptides in the cat brainstem. In: Coveñas R, Mangas A, Narváez JA, eds. *Focus on Neuropeptide Research.* Transworld Research Network: Trivandrum; 2007: 57–101.
13. Pesini P, Pego-Reigosa R, Tramu G, et al. Distribution of met-enkephalin immunoreactivity in the diencephalon and the brainstem of the dog. *J Chem Neuroanat.* 2000; 19(4): 243–258, doi: [10.1016/s0891-0618\(00\)00071-5](#), indexed in Pubmed: [11036241](#).
14. Cullen JM, Cascella M. *Physiology, enkephalin.* StatPearls Publishing: Treasure Island; 2021, indexed in Pubmed: [32491696](#).

15. Ratto MH, Huanca W, Singh J, et al. Local versus systemic effect of ovulation-inducing factor in the seminal plasma of alpacas. *Reprod Biol Endocrinol*. 2005; 3: 29, doi: [10.1186/1477-7827-3-29](https://doi.org/10.1186/1477-7827-3-29), indexed in Pubmed: [16018817](https://pubmed.ncbi.nlm.nih.gov/16018817/).
16. Ratto M, Huanca W, Singh J, et al. Comparison of the effect of natural mating, LH, and GnRH on interval to ovulation and luteal function in llamas. *Anim Reprod Sci*. 2006; 91(3-4): 299–306, doi: [10.1016/j.anireprosci.2005.03.015](https://doi.org/10.1016/j.anireprosci.2005.03.015), indexed in Pubmed: [15896931](https://pubmed.ncbi.nlm.nih.gov/15896931/).
17. de Souza, Yi P, Aguilar LA, et al. et al. Mapping of leucine-enkephalin in the alpaca (*Lama pacos*) brainstem. In: Coveñas R, Mangas A, Narváez JA, eds. *Focus on Neuropeptide Research*. Transworld Research Network: Trivandrum; 2007: 103–114.
18. de Souza E, Coveñas R, Yi P, et al. Mapping of CGRP in the alpaca (*Lama pacos*) brainstem. *J Chem Neuroanat*. 2008; 35(4): 346–355, doi: [10.1016/j.jchemneu.2008.02.004](https://doi.org/10.1016/j.jchemneu.2008.02.004), indexed in Pubmed: [18420379](https://pubmed.ncbi.nlm.nih.gov/18420379/).
19. de Souza E, Aguilar LA, Díaz-Cabiale Z, et al. Mapping of neurotensin in the alpaca (*Lama pacos*) brainstem. *Anat Histol Embryol*. 2014; 43(4): 245–256, doi: [10.1111/ahc.12067](https://doi.org/10.1111/ahc.12067), indexed in Pubmed: [23692174](https://pubmed.ncbi.nlm.nih.gov/23692174/).
20. de Souza E, Sánchez ML, Aguilar LA, et al. Mapping of somatostatin-28 (1-12) in the alpaca (*Lama pacos*) brainstem. *Microsc Res Tech*. 2015; 78(5): 363–374, doi: [10.1002/jemt.22482](https://doi.org/10.1002/jemt.22482), indexed in Pubmed: [25754727](https://pubmed.ncbi.nlm.nih.gov/25754727/).
21. Marcos P, Arroyo-Jiménez MM, Lozano G, et al. Mapping of tyrosine hydroxylase in the alpaca (*Lama pacos*) brainstem and colocalization with CGRP. *J Chem Neuroanat*. 2011; 41(2): 63–72, doi: [10.1016/j.jchemneu.2010.10.002](https://doi.org/10.1016/j.jchemneu.2010.10.002), indexed in Pubmed: [21050884](https://pubmed.ncbi.nlm.nih.gov/21050884/).
22. Sánchez ML, de Souza E, Aguilar LA, et al. Distribution of alpha-neoendorphin, ACTH (18-39) and beta-endorphin (1-27) in the alpaca brainstem. *Anat Histol Embryol*. 2018; 47(5): 481–492, doi: [10.1111/ahc.12387](https://doi.org/10.1111/ahc.12387), indexed in Pubmed: [30027642](https://pubmed.ncbi.nlm.nih.gov/30027642/).
23. Sánchez ML, Mangas A, Medina LE, et al. Immunohistochemical mapping of neurotensin in the alpaca diencephalon. *Folia Histochem Cytobiol*. 2018; 56(1): 49–58, doi: [10.5603/FHC.a2018.0003](https://doi.org/10.5603/FHC.a2018.0003), indexed in Pubmed: [29516445](https://pubmed.ncbi.nlm.nih.gov/29516445/).
24. Marcos P, Coveñas R, Narváez JA, et al. Immunohistochemical mapping of enkephalins, NPY, CGRP, and GRP in the cat amygdala. *Peptides*. 1999; 20(5): 635–644, doi: [10.1016/s0196-9781\(99\)00018-2](https://doi.org/10.1016/s0196-9781(99)00018-2), indexed in Pubmed: [10465517](https://pubmed.ncbi.nlm.nih.gov/10465517/).
25. Duque-Díaz E, Díaz-Cabiale Z, Narváez JA, et al. Mapping of enkephalins and adrenocorticotrophic hormone in the squirrel monkey brainstem. *Anat Sci Int*. 2017; 92(2): 275–292, doi: [10.1007/s12565-016-0333-2](https://doi.org/10.1007/s12565-016-0333-2), indexed in Pubmed: [26897373](https://pubmed.ncbi.nlm.nih.gov/26897373/).
26. Samsam M, Coveñas R, Csillik B, et al. Depletion of substance P, neurokinin A and calcitonin gene-related peptide from the contralateral and ipsilateral caudal trigeminal nucleus following unilateral electrical stimulation of the trigeminal ganglion; a possible neurophysiological and neuroanatomical link to generalized head pain. *J Chem Neuroanat*. 2001; 21(2): 161–169, doi: [10.1016/s0891-0618\(01\)00088-6](https://doi.org/10.1016/s0891-0618(01)00088-6), indexed in Pubmed: [11312057](https://pubmed.ncbi.nlm.nih.gov/11312057/).
27. Nusbaum M, Blitz D, Marder E. Functional consequences of neuropeptide and small-molecule co-transmission. *Nature Rev Neurosci*. 2017; 18(7): 389–403, doi: [10.1038/nrn.2017.56](https://doi.org/10.1038/nrn.2017.56), indexed in Pubmed: [28592905](https://pubmed.ncbi.nlm.nih.gov/28592905/).
28. Martins I, Tavares I. Reticular formation and pain: the past and the future. *Front Neuroanat*. 2017; 11: 51, doi: [10.3389/fnana.2017.00051](https://doi.org/10.3389/fnana.2017.00051), indexed in Pubmed: [28725185](https://pubmed.ncbi.nlm.nih.gov/28725185/).
29. Yoshida W, Seymour B, Koltzenburg M, et al. Uncertainty increases pain: evidence for a novel mechanism of pain modulation involving the periaqueductal gray. *J Neurosci*. 2013; 33(13): 5638–5646, doi: [10.1523/JNEUROSCI.4984-12.2013](https://doi.org/10.1523/JNEUROSCI.4984-12.2013), indexed in Pubmed: [23536078](https://pubmed.ncbi.nlm.nih.gov/23536078/).
30. Blair HT, Cho J, Sharp PE. Role of the lateral mammillary nucleus in the rat head direction circuit: a combined single unit recording and lesion study. *Neuron*. 1998; 21(6): 1387–1397, doi: [10.1016/s0896-6273\(00\)80657-1](https://doi.org/10.1016/s0896-6273(00)80657-1), indexed in Pubmed: [9883731](https://pubmed.ncbi.nlm.nih.gov/9883731/).
31. Bast N, Boxhoorn S, Supér H, et al. Atypical arousal regulation in children with autism but not with attention-deficit/hyperactivity disorder as indicated by pupillometric measures of locus coeruleus activity. *Biol Psychiatry Cogn Neurosci Neuroimaging*. 2021, doi: [10.1016/j.bpsc.2021.04.010](https://doi.org/10.1016/j.bpsc.2021.04.010), indexed in Pubmed: [33930603](https://pubmed.ncbi.nlm.nih.gov/33930603/).
32. Gong L, Shi M, Wang J, et al. The abnormal functional connectivity in the locus coeruleus-norepinephrine system associated with anxiety symptom in chronic insomnia disorder. *Front Neurosci*. 2021; 15: 678465, doi: [10.3389/fnins.2021.678465](https://doi.org/10.3389/fnins.2021.678465), indexed in Pubmed: [34093121](https://pubmed.ncbi.nlm.nih.gov/34093121/).
33. James T, Kula B, Choi S, et al. Locus coeruleus in memory formation and Alzheimer's disease. *Eur J Neurosci*. 2020 [Epub ahead of print], doi: [10.1111/ejn.15045](https://doi.org/10.1111/ejn.15045), indexed in Pubmed: [33190318](https://pubmed.ncbi.nlm.nih.gov/33190318/).
34. Basso MA, Bickford ME, Cang J. Unraveling circuits of visual perception and cognition through the superior colliculus. *Neuron*. 2021; 109(6): 918–937, doi: [10.1016/j.neuron.2021.01.013](https://doi.org/10.1016/j.neuron.2021.01.013), indexed in Pubmed: [33548173](https://pubmed.ncbi.nlm.nih.gov/33548173/).
35. Duque-Díaz E, Alvarez-Ojeda O, Coveñas R. Enkephalins and ACTH in the mammalian nervous system. *Vitam Horm*. 2019; 111: 147–193, doi: [10.1016/bs.vh.2019.05.001](https://doi.org/10.1016/bs.vh.2019.05.001), indexed in Pubmed: [31421699](https://pubmed.ncbi.nlm.nih.gov/31421699/).
36. Muñoz M, Coveñas R. Substance P. *Encyclopedia of endocrine diseases*. 2018: 571–578, doi: [10.1016/b978-0-12-801238-3.95886-0](https://doi.org/10.1016/b978-0-12-801238-3.95886-0).
37. Palkovits M. Neuropeptides in the brain. In: Ganong WF, Martini L, eds. *Frontiers in Neuroendocrinology*. Raven Press, New York: 1–44.
38. Bouras C, Vallet PG, Dobrinov H, et al. Substance P neuronal cell bodies in the human brain: complete mapping by immunohistofluorescence. *Neurosci Lett*. 1986; 69(1): 31–36, doi: [10.1016/0304-3940\(86\)90409-x](https://doi.org/10.1016/0304-3940(86)90409-x), indexed in Pubmed: [2427977](https://pubmed.ncbi.nlm.nih.gov/2427977/).

Submitted: 24 April, 2021

Accepted after reviews: 6 July, 2021

Available as AoP: 26 July, 2021

Distribution and neurochemical characteristic of the cardiac nerve structures in the heart of chinchilla (*Chinchilla laniger* Molina)

Malgorzata Radzimirska¹, Jacek Kuchinka¹, Tadeusz Kuder², Elzbieta Nowak¹,
Wojciech Trybus¹, Grzegorz Wrobel², Aleksander Szczurkowski¹

¹Department of Medical Biology, Institute of Biology, Jan Kochanowski University in Kielce, Kielce, Poland

²Department of Anatomy, Collegium Medicum, Jan Kochanowski University in Kielce, Kielce, Poland

Abstract

Introduction. The heart innervation is made up of plexo-ganglionic formation containing sympathetic, parasympathetic, and sensory components. We examined the distribution and neurochemical coding of the ganglia and nerve fibers in the chinchilla's heart.

Material and methods. The heart sections of 10 male and 10 female adult chinchillas were processed in accordance with the thiocholine method for acetylcholine esterase (AChE), and the SPG method for detecting the presence of adrenergic fibers was applied. The routine technique of immunohistochemical (IHC) staining with primary antibodies directed against ChAT, VAcHT, D β H, TH, CART, NPY, VIP, GAL and SOM was used. The secondary antibodies were conjugated with Alexa Fluor 488 and Alexa Fluor 555 fluorophores.

Results. The epicardium contained ganglia and nerve fibers, the myocardium had a few ganglion neurocytes and nerve fibers, and the endocardium contained only nerve fibers. In the epicardium, AChE-positive fibers were more prevalent than SPG-positive fibers. All the ganglion cells were immunopositive for ChAT and VAcHT. Some cells also had a positive reaction to D β H and TH. Fibers containing cholinergic and adrenergic markers were numerous, while many of them were ChAT/D β H- and VAcHT/TH-positive. CART/NPY and CART/VIP, as well as CART and GAL, were observed to be colocalized in ganglion neurocytes, as well as in individual cells. The nerve fibers were found to contain all the neurotransmitters we tested for, as well as the following co-occurrences: ChAT/D β H, VAcHT/TH, CART/NPY, CART/VIP, CART/GAL, and CART/SOM.

Conclusions. Our analysis of the neurochemical profile of the nerve structures in chinchilla's heart showed that, despite interspecies differences, the general pattern of the distribution of autonomic nervous system structures is similar to that of other mammals' species, including humans. (*Folia Histochemica et Cytobiologica* 2021, Vol. 59, No. 3, 157–166)

Key words: chinchilla; cardiac innervation; histochemistry; immunohistochemistry

Correspondence address: Aleksander Szczurkowski, PhD, DrSc.
Department of Medical Biology, Institute of Biology,
Jan Kochanowski University in Kielce,
7 Uniwersytecka St., 25-406 Kielce, Poland
tel.: +48 41 349 63 13
e-mail: aleksander.szczurkowski@ujk.edu.pl

Introduction

The cardiac nervous system is made up of a series of plexo-ganglionic formations and contains sympathetic, parasympathetic, and sensory components. The autonomic components, however, are the main components regulating functions of cardiomyocytes, the conductive system, and the blood vessels. The sympathetic components make up a system that stimulates the cardiomyocytes of the heart muscle and of

the heart conduction system through the release of neurotransmitters at nerve endings (noradrenaline — NA, neuropeptide Y — NPY, galanin — GAL, and nitric oxide synthase — NOS). The parasympathetic part acts with a different set of neurotransmitters (acetylcholine — ACh, cocaine- and amphetamine-regulated transcript — CART, and vasoactive intestinal polypeptide — VIP) to inhibit heart function [1–5].

The innervation of the heart has been studied in many species of animals from different taxonomic classes. The majority of studies have been carried out on the small mammals, particularly on laboratory rodents, and the intrinsic cardiac nervous system in rat has been studied at the molecular level [6]. Moreover, investigations have been carried out on farm species [7]. A few papers also described the morphology, topography, and physiology of the human cardiac ganglia [8–15].

The ganglia are mainly located in the strategic regions of the heart: around the sinoatrial and atrioventricular nodes, the main vessels of the heart, and the region of the coronary sulcus. In this respect, there is usually significant interspecific variation, but even so, the general pattern of distribution is similar in both humans and other mammalian species [11, 14, 16].

Our results indicate that there may be several subpopulations of neurocytes in myocardial ganglia, containing various combinations of neurotransmitters. The neurons of the cardiac ganglia are thus not phenotypically and functionally homogeneous but constitute a neurochemical complex that goes beyond the classical picture of parasympathetic ganglia [5, 17, 18].

The chinchilla often is used as an animal model for many types of investigations related to the dysfunction of human organs such as middle ear [19], uterus [20], digestive system and lungs [21]. But there is a lack of detailed data on the autonomic nervous system of its heart. Research to date has only provided incomplete information on the morphology and topography of the parasympathetic ganglia in this species [22]. There have also been descriptions of adrenergic and cholinergic innervation of the atrioventricular valves [23] and pancreas [24]. However, there is no data available on the neurochemical analysis of ganglionic cells, nor is there detailed information available on the innervation of the heart muscle (including the types of fiber) in the chinchilla. It thus seems advisable to carry out a thorough analysis of the neural structures of the chinchilla's heart, both in terms of topography and neurochemical profile. This is the first study of this specific topic. Our results are important in both their theoretical and practical aspects.

Material and methods

We investigated twenty adult (10 months old) chinchillas (*Chinchilla laniger* Molina, 1782) of both sexes (10 males and 10 females, weight 400–600 g). Animals were collected immediately after industrial slaughter. The research conformed to the requirements of Act for the Protection of Animals Used for Scientific or Educational Purposes (15 January 2015). Studies of tissues obtained post-mortem do not require the approval of an ethics committee. We performed morphological investigation of the atria and ventricles of the heart using the acetylcholinesterase (AChE) [25, 26] and SPG [27] histochemical techniques, as well as routine single and double staining immunohistochemistry.

Material sampling and histochemistry. Ten individuals (5 males and 5 females) were used for histochemical investigations. Immediately after slaughter, in appropriately adapted room, under stereo microscope control (Nikon SMA 800) the anterior wall of the chests was opened, and hearts were collected removing the pericardial sac. Next, heart tissues were rinsed in physiological solution and fixed for 30 minutes in 10% buffered formalin. During the fixation, collected material was transported to the Department of Medical Biology of Jan Kochanowski University in Kielce, Poland, where the other procedures were performed. A separate microdissection of the atria and ventricles was used to prepare whole mount specimens. Flat atrial preparation was carried out in the following manner. The atria and ventricles were separated along the atrioventricular groove and the aorta, and the pulmonary trunk was gently detached. Cholinergic positive structures were investigated with AChE method. The macro-morphological (whole mount) specimens were treated in the incubated solution at pH 6.4–6.8 and temperature 37°C (acetylthiocholine iodide, acetate buffer, sodium citrate, cooper sulfate, distilled water, potassium ferricyanide). The activity of the pseudocholine nonspecific esterase was blocked using iso-OMPA. Next, the tissues were rinsed in distilled water, and ammonium sulfide was added to intensify the reaction and the specimens were mounted in DPX.

The adrenergic structures were investigated using the SPG (sucrose-phosphate-glyoxylic acid) method. Briefly, whole-mount specimens were immersed in SPG solution for 5 seconds (reagents: glyoxylic acid monohydrate, sucrose, potassium phosphate monobasic), dried under a cold stream of air for 10 min, and heated to 95°C for 3 min. Specimens were observed using fluorescence microscope Nikon 90i (Nikon, Tokyo, Japan) and digital pictures were taken with Nikon Digital Sight SD-L1 system using NIS-Elements 3.22 software.

Immunohistochemistry. The chests of ten individuals (5 males and 5 females) were opened and the left ventri-

Table 1. Primary antisera used in the research

Antigen	Host	Type	Dilution	Catalog No.	Supplier
ChAT	Goat	Polyclonal	1:100	NBP1-30052	Novus Biologicals, Cambridge, UK
VAcHT	Rabbit	Polyclonal	1:1000	EUD261	Acris Antibodies, San Diego, CA, USA
DβH	Rabbit	Polyclonal	1:500	NBP1-78349	Novus Biologicals, Cambridge, UK
TH	Mouse	Monoclonal	1:500	MAB318	Millipore, Temecula, CA, USA
CART	Mouse	Monoclonal	1:2000	MAB163	R&D System, Minneapolis, MN, USA
NPY	Rabbit	Polyclonal	1:2000	AHP2189	AbD Serotec, Hercules, CA, USA
VIP	Rabbit	Polyclonal	1:2000	Ab22736	Abcam, Cambridge, UK
GAL	Rabbit	polyclonal	1:1000	AB2233	Millipore, Temecula, CA, USA
SOM	Rabbit	polyclonal	1:1500	8330-0154	AbD Serotec, Hercules, CA, USA

Abbreviations: ChAT — choline acetyltransferase, VAcHT — vesicular acetylcholine transporter, DβH — dopamine β-hydroxylase, TH — tyrosine hydroxylase, CART — cocaine- and amphetamine-regulated transcript, NPY — neuropeptide Y, VIP — vasoactive intestinal polypeptide, GAL — galanin, SOM — somatostatin

Table 2. Secondary antisera used in the research

Host	Fluorophore	Dilution	Catalog No.	Supplier
Donkey anti-rabbit	Alexa Fluor 488	1:500	A21206	Invitrogen, Carlsbad, CA, USA
Donkey anti-goat	Alexa Fluor 555	1:500	A21432	Invitrogen, Carlsbad, CA, USA
Donkey anti-mouse	Alexa Fluor 555	1:500	A31570	Invitrogen, Carlsbad, CA, USA

cles were incised to insert cannula into the aorta, and the right cardiac auricle was then transected. Perfusion was performed using 0.4 l of 4% ice-cold buffered paraformaldehyde (pH 7.4) with perfusion apparatus [28]. Hearts were collected and additionally postfixed by immersion in the same fixative for 15 min, rinsed with phosphate buffer, and transferred to and stored in 30% buffered sucrose solution for two weeks. Frozen slides (8–10 μm) were prepared with the microtome (Shandon Cryotome E; Thermo Scientific, USA). Next, the specimens (whole mount specimens and sections) were processed for the single and double-labelling immunofluorescence method. Tissues were incubated for 16–20 h at room temperature with primary antibodies against choline acetyltransferase (ChAT), vesicular acetylcholine transporter (VAcHT), dopamine β-hydroxylase (DβH), tyrosine hydroxylase (TH), cocaine- and amphetamine-regulated transcript (CART), neuropeptide Y (NPY), vasoactive intestinal polypeptide (VIP), galanin (GAL), and somatostatin (SOM) (Table 1). Tissues were then next incubated with proper secondary antibodies conjugated with fluorochrome Alexa Fluor 488 and Alexa Fluor 555 (Table 2). After incubation, the specimens were coverslipped with buffered glycerol and examined under a fluorescent microscope with a confocal Nikon Eclipse Ti-A1R (Nikon Instruments Inc., NY, USA) attachment.

Control over the specificity of staining was obtained by preabsorbing a diluted antiserum with 20 μg/ml of an appropriate antigen, which completely abolished the specific

immunoreactivity. In addition, we repeated the experiments with the primary antiserum replaced by nonimmune serum, or by phosphate buffered saline (PBS), in order to verify the specificity of particular immunoreactions.

Results

Histochemistry

Histochemical examination using the AChE method showed the presence of ganglia with different number of cells (from a dozen to several dozens) and individual ganglion cells in various regions of the epicardium of the atria of the heart. A smaller number of clusters of ganglionic neurocytes (7–10) were seen in the right atrium near the ostium of the cranial vena cava (Fig. 1A), and two dense clusters of cholinergic neurocytes were noted in the area of the right atrium auricle. On the other hand, several ganglia (3–5) composed of a few tens of cells were found on the surface of the left atrium near the ostia of the pulmonary veins (Fig. 1B). All these structures were connected to each other by a network of nerve fibers, which also showed a positive reaction to AChE. In this way, a kind of plexo-ganglionic cholinergic structure was formed, containing both larger structures and some structures of only a few cells mainly in the area of the sinoatrial node (Fig. 1C). We observed the connection of these plexo-ganglia with other similar structures located by the

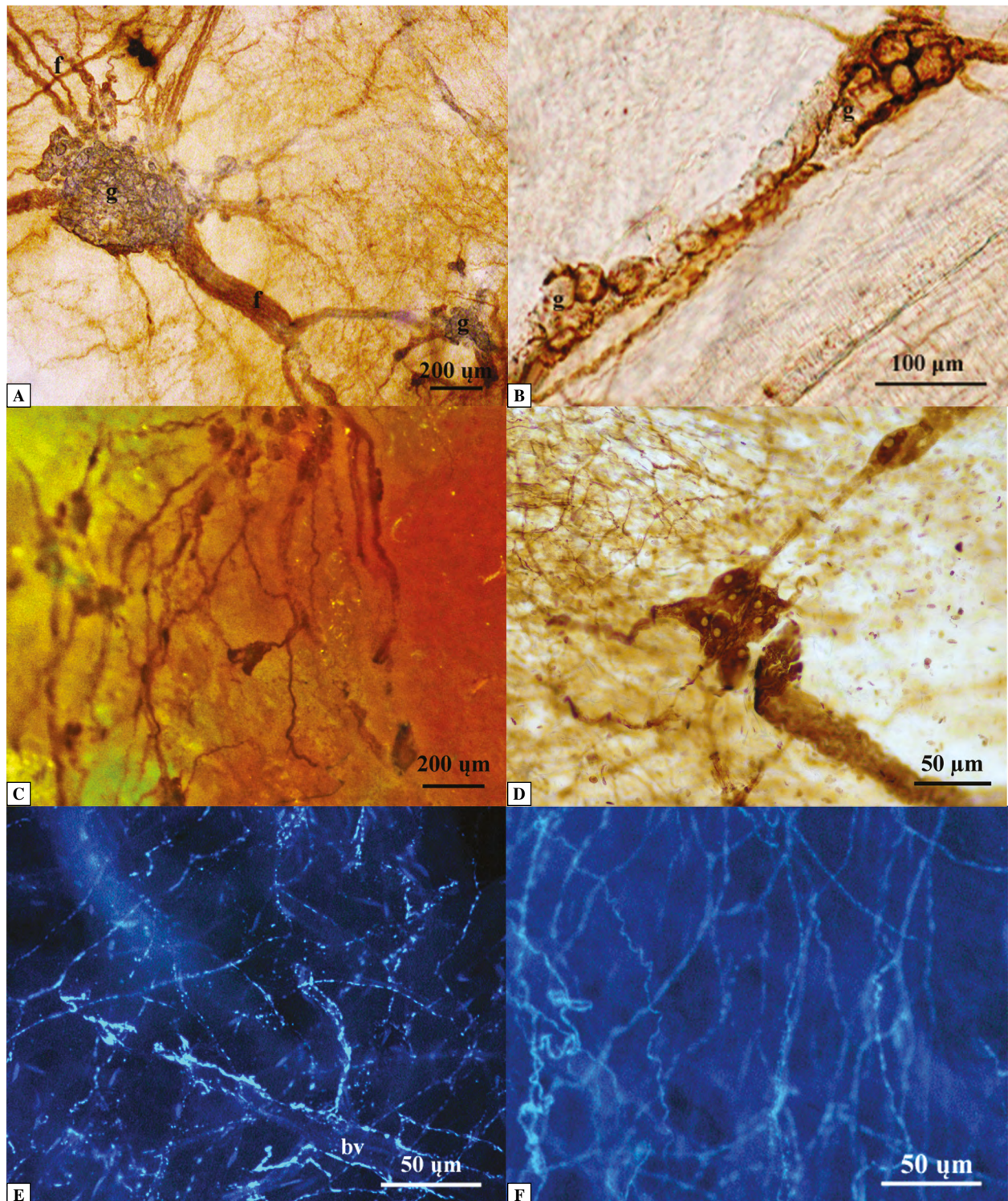


Figure 1. Structures of the autonomous nervous system in various regions of chinchilla's heart. **A.** The acetylcholinesterase (AChE)-positive ganglia in the epicardium of the right atrium near the ostium of the cranial vena cava. **B.** The elongated AChE-positive ganglion on the posterior surface of the left atrium near the ostia of the pulmonary veins. **C.** The AChE-positive plexo-ganglionic structures on the anterior surface of the right atrium in the area of the sinoatrial node. **D.** The AChE-positive fibers on the posterior surface of the right ventricle. **E.** The adrenergic nerve fibers in the epicardium of the left atrium along the blood vessels. **F.** The adrenergic plexus in the epicardium posterior wall of the right ventricle. Figures 1A–D were stained by histochemical AChE method, and Figs. 1E, F by the SPG-method as described in Methods. Legend: g — ganglion, bv — blood vessels, f — nerve fibers.

right and left coronary sulci on the atrial facies of the heart. In the case of the epicardium of the ventricles, the ganglionic clusters were smaller, usually with only a few cells (Fig. 1D). The thickest AChE-positive bundles of fibers (about 100 μm thickness) branched into thinner and thinner bundles (Fig. 1A). Significantly thinner fibers (below 50 μm thickness) were seen on the surface of the ventricles in the vicinity of the coronary sulcus (Fig. 1D). The myocardium of both the atria and the ventricles contained individual neurocytes, and numerous fibers, while the endocardium contained only tiny nerve fibers.

The SPG method only revealed numerous adrenergic fibers located in the atria and ventricles, with characteristic varicosities (Fig. 1E, F). These formed a three-dimensional network in all layers of the heart, which was well developed, especially in the epicardium and myocardium. A particularly high density of SPG-positive fibers was observed in the adventitia of blood vessels (Fig. 1E). A dense neuronal network was also observed around the papillary muscles in the ventricles of the heart.

Immunohistochemistry

Immunohistochemical (IHC) methods allowed for a more detailed analysis of the innervation of the heart. Ganglia immunopositive to ChAT and VAcHT were found, with various numbers of neurocytes (from a few to a few dozen) in the epicardium and myocardium of the atria and ventricles. The largest immunoreactive ChAT ganglia were observed near the ostium of the cranial vena cava in the epicardium of the right atrium (Fig. 2A) and on the surface of the left atrium in the vicinity ostia of the pulmonary veins. Strong immunopositivity to ChAT and VAcHT was observed in numerous nerve fibers in all layers of the heart, in both atria and ventricles (Fig. 2A–D). The cholinergic fibers ran singly and also formed bundles of varying thickness. In the case of the enzymes of the catecholamine pathway, D β H and TH immunoreactivity was observed in numerous fibers present in the epicardium, myocardium, and endocardium (Fig. 2B, D). Only a few ganglion cells (particularly those located in the atria) showed colocalization of ChAT and D β H (Fig. 2A). VAcHT and TH were colocalized in ganglion neurocytes (Fig. 2C), and numerous fibers showed ChAT/D β H and VAcHT/TH colocalization (Fig. 2B, D).

CART-immunopositive neural structure studies have shown the presence of this neuropeptide in numerous nerve fibers, in both the atria and in the ventricles of the heart (Fig. 3A–F). They were especially numerous in the epicardium and myocardium, where they formed a spatial network while in the

endocardium, they were thin and sparse. CART-immunoreactivity of numerous nerve cells in the ganglia of the epicardium of the right ventricle and the right and left atrium was observed (Fig. 3A, C, D). We also noted individual cells and small CART-positive clusters of them in the atrial myocardium.

NPY was seen in numerous nerve fibers, which usually form a three-dimensional network in all three layers of the heart (Fig. 3A, B). In addition, NPY positive cells were seen in the ganglia of the atrial epicardium (Fig. 3A). The most abundant VIP-positive and GAL-positive nerve fibers were found in the epicardium and myocardium of both the atria and ventricles (Fig. 3C, D). The VIP-immunopositive fibers formed a dense, very fine network. In the outer layer of the left atrium, presence of GAL was observed in the neurocytes that form small clusters there (Fig. 3D). Multiple SOM-positive fibers of varying thickness were seen in all layers of the atria, and ventricles (Fig. 3E, F). The most numerous were present in the epicardium and myocardium of the left atrium, along the walls of blood vessels (Fig. 3E).

The CART/NPY, CART/VIP and CART/GAL neuropeptides were found to be colocalized in the cytoplasm of ganglion cells in the atrial epicardium, atria and ventricles (Fig. 3A, C, D). CART-immunopositive nerve fibers also showed colocalization with NPY, especially in those along the blood vessels (Fig. 3B). The coexistence of CART and VIP, as well as of CART and GAL, was found in epicardial and myocardial fibers (Fig. 3D). We observed CART- and SOM-immunopositive nerve fibers in the myocardium of the left atrium and ventricle, particularly in the vicinity of blood vessels (Fig. 3E, F).

Discussion

The regulation of the heart function by the autonomic nervous system has two main components: an adrenergic component, which stimulates the heart and conduction system, and a cholinergic component, which inhibits them [29, 30]. It is also known that the sympathetic part consists mainly of nerve fibers, while the parasympathetic part involves both fibers and nerve cells. The situation is similar for the investigated species. However, despite numerous reports on the topic, the neurochemical nature of these neural structures in other mammals is not entirely clear. Some authors have indicated that there are several subpopulations of neurons in the ganglia of different neurochemical coding, and therefore also with different functional capabilities. The most common neurons are those with the classic cholinergic nature. A second group of cardiac neurons is of a dual neurochemical

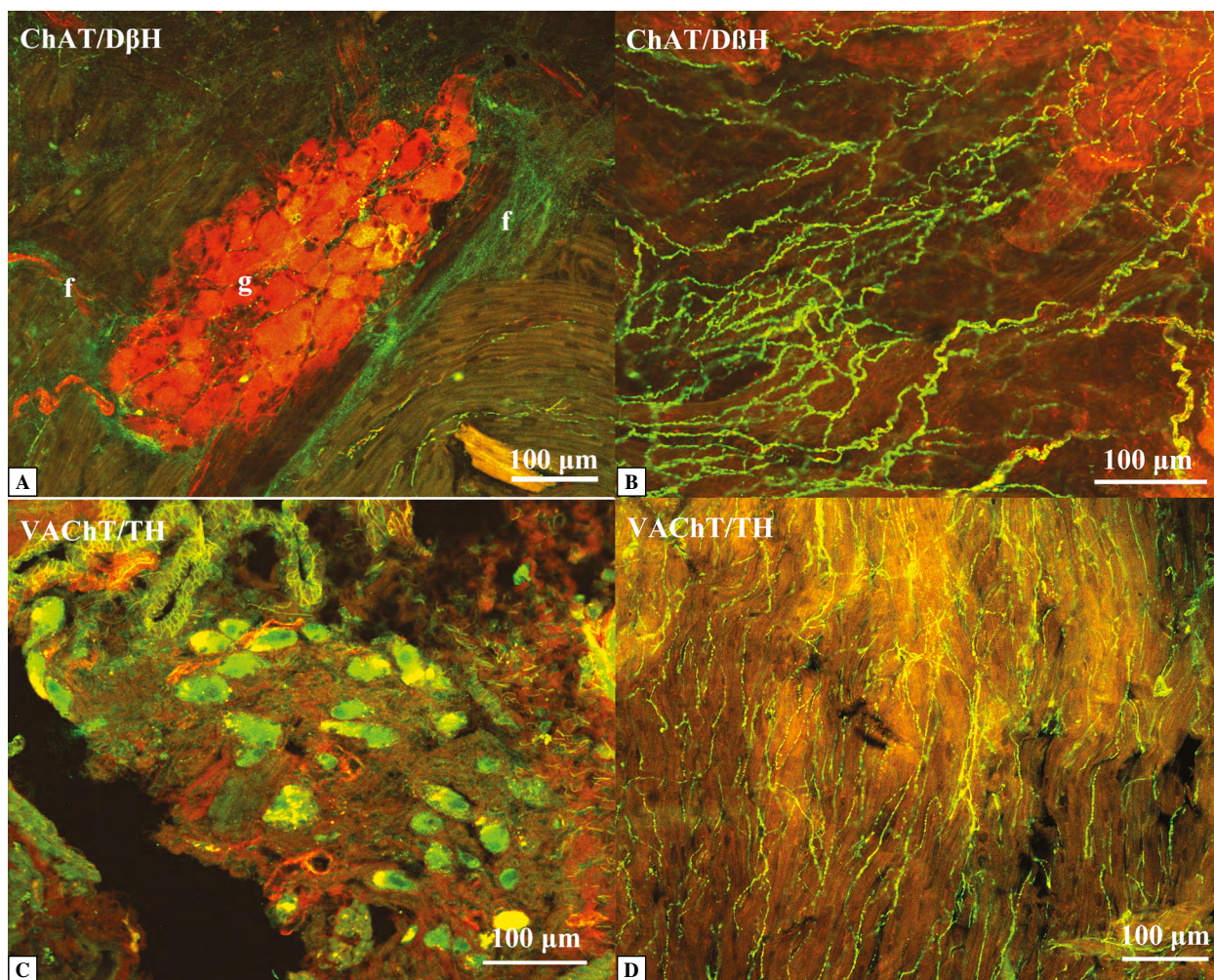


Figure 2. **A.** The autonomic ganglion and nerve fibers in the epicardium of chinchilla's right atrium (ChAT — red, D β H — green; colocalization — gold/yellow; whole mount specimen). **B.** The cholinergic and adrenergic fibers in the epicardium of the left ventricle (ChAT — red, D β H — green; colocalization — gold/yellow; whole mount specimen). **C.** The agglomeration of neurocytes in the epicardium of the right atrium (VAcHT — green, TH — red; colocalization — gold/yellow; frozen section). **D.** The distribution of the nerve fibers in the myocardium of the right ventricle (VAcHT — green, TH — red; colocalization — gold/yellow; whole mount specimen). Immunohistochemical staining was performed as described in Methods. Legend: g — ganglion, bv — blood vessels, f — nerve fibers. Abbreviations as in the description of Table 1.

type: the main neurotransmitter is acetylcholine, but enzymes belonging to the catecholamine pathway are also present. There is a disagreement in the literature on the relative abundances of cholinergic and noncholinergic cells: Weihe *et al.* [18] suggested that 40–50% of rhesus and human cardiac neurons may contain enzymes of the catecholamine pathway. Singh *et al.* [11] showed similar results for humans. Haberberger and Kummer [31] found that all guinea pig cardiac neurons contained both choline acetyltransferase and B-2 adrenoreceptors. Rysevaite *et al.* [32] found in mouse only 4% of TH-positive cells, and only 14% of ChAT and TH positive cells. Similar colocalization has been reported for rat and rabbit [33, 34].

A similar situation has been found for chinchilla, with only a small number of ganglionic neurocytes being immunoreactive to ChAT and D β H. Colocalization of these mediators was also found in nerve fibers where ChAT and TH were observed.

Recently, a number of papers have described the presence of the CART peptide in heart ganglia [35–38]. CART is known to be an anorexigenic peptide produced in brain, mainly in the hypothalamus. It has also been found in nerve endings in the digestive tract and in parasympathetic ganglia. Most reports have indicated that CART is present in the nerve fibers of the heart, although there have also been reports of its presence in cardiac neurons [35–37]. CART

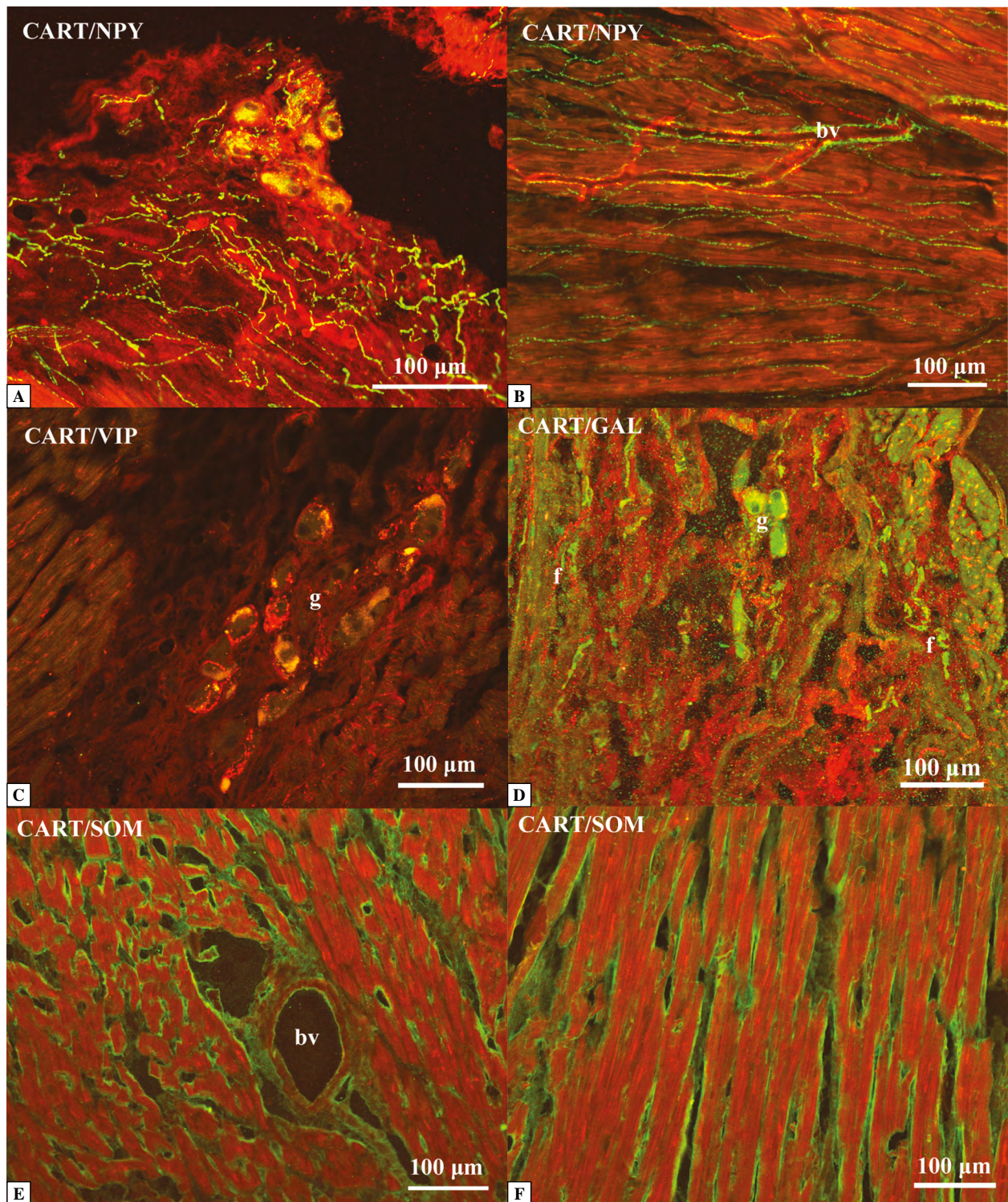


Figure 3. **A.** The agglomeration of the nerve cells and nerve fibers in the epicardium of chinchilla's right atrium (CART — red, NPY — green; colocalization — gold/yellow; frozen section). **B.** The nerve fibers along the blood vessels in the myocardium of the right atrium (CART — red, NPY — green; colocalization — gold/yellow; whole mount specimen). **C.** The small agglomeration of neurocytes in the myocardium of the left ventricle (CART — red, VIP — green; colocalization — gold/yellow; frozen section). **D.** The neurocytes and numerous nerve fibers in the epicardium of the left atrium (CART — red, GAL — green; colocalization — gold/yellow; frozen section). **E–F.** The numerous nerve fibers in the myocardium of the left atrium (E) and left ventricle (F) (CART — red, SOM — green; colocalization — gold/yellow; frozen section). IHC — method. Legend: g — ganglion, bv — blood vessels, f — nerve fibers. Abbreviations as in the description of Table 1.

raises the blood pressure in the coronary arteries and increases the heart rate. Calupa *et al.* [35] showed that most guinea pig cardiac ganglia were innervated with immunoreactive CART nerve fibers. A few ganglion neurocytes have been found to be CART positive; these also contained ChAT or NOS. Richardson *et al.* [37] noted the presence of CART-immunoreactivity in 46% of rat cardiac neuron bodies, some of which also contained NOS or calbindin. The present study found a positive response to CART in the chinchilla's atrial ganglia. The colocalization of CART with NPY and GAL has also been observed in nerve fibers, especially along blood vessels. Some authors have suggested that CART protects mitochondrial DNA from oxidative stress [38]. NPY is an important peptide neurotransmitter involved in sympathetic activation. According to Richardson *et al.* [33], all rat cardiac neurons other than ChAT-positive contain NPY. The present study also found NPY in both the cells and the nerve fibers of the heart.

The vasoactive intestinal peptide (VIP) mainly affects the intestinal nervous system. Nevertheless, its presence has also been demonstrated in the heart ganglia. Horackova *et al.* [39] noted its presence in guinea pig heart. About 10% of neurocytes dispersed throughout the heart muscle were VIP-positive. Moravec *et al.* [40] did not find it in rat ganglionic neurons, while Parsons *et al.* [41] and Steele *et al.* [42] noted the coexistence of VIP and other neurotransmitters (NPY, SP, NOS) in guinea pig heart. In the investigated species, we did not find VIP in nerve cells, though numerous fibers were VIP-immunoreactive.

Galanin (GAL) is a neuropeptide that affects the metabolism by affecting the frequency of food consumption; it reduces energy expenditure, which promotes obesity [43]. It also participates in cardiovascular regulation causing an increase in blood pressure and tachycardia [44]. As shown by physiological studies conducted in guinea pigs, the galanin released from sympathetic neurons controls the heart's rate. Herring *et al.* [45] indicate that galanin receptors are found only in the right atrium. Our results revealed GAL both in the nerve cells and fibers in the epicardium of the left atrium of chinchilla's heart.

Somatostatin (SOM) is a neuropeptide present in many organs that is also involved in the regulation of the heart. It can occur alone or with AChE. The inhibitory function of SOM has been demonstrated for contractions of human heart muscle [42]. Day *et al.* [8] demonstrated that different regions of the rat heart (right atrium, right ventricle, and atrioventricular node) contain high concentrations of somatostatin. Its presence has also been found in the few cardiac endings of the guinea pig vagal nerve and in numerous subsets of cardiac neurons [36, 42].

Our study also found SOM in nerve fibers, mainly in the epicardium.

The neural structures in the heart (ganglia and plexuses) are found in the epicardium, myocardium, and endocardium. Clusters of neurocytes are found mainly in the epicardium, while a few loosely spaced cells are found in the myocardium; only nerve fibers are present in the endocardium. There are divergent data in the literature regarding the density of nerve fibers in particular parts of the heart. Crick *et al.* [46] found in pig that the density of nerve fibers in the epicardium and myocardium was greater in the ventricles (particularly in the left ventricle) than in the atria. In the endocardium they also noted a higher density of nerve fibers in the right ventricle and right atrium. A similar distribution of density of nerve structures in human hearts was described by Marron *et al.* [9]. Gordon *et al.* [47] showed a different pattern of density in the hearts of pig and domestic cattle: there was a greater density in the atria than in the ventricles, and greater density in the epicardium than in the endocardium. In the chinchilla a richer neural network of atrial epicardium was found, and in the endocardium of ventricles — especially in the papillary muscles. Taking into account the density of nerve fibers networks in the epicardium, we can state that in chinchilla the cholinergic network is denser than the adrenergic network. In the work of Kuchinka *et al.* [23] concerning innervation of atrioventricular valves in chinchilla, the opposite was found, with adrenergic innervation predominating over cholinergic.

To summarize, taking into account the colocalization of ChAT/D β H, VAcHt/TH, CART/NPY, CART/VIP, CART/GAL, and CART/SOM, the analysis of the neurochemical nature of the nerve structures in chinchilla's heart fits with the current model of the chemical code of the mammalian cardiac nervous system, despite some differences in the details. At the same time, studies on various mammalian species cardiac ganglia allow us to conclude that the pattern of innervation and neurochemical characteristics may serve as a model for human heart. An important piece of information in this context would seem to be provided by the relatively high proportion of neurotransmitters associated with sympathetic activation, which may contribute to an increase in catecholamine concentration in the heart, especially in people with cardiomyopathy [48, 49].

References

1. Forsgren S, Moravec M, Moravec J. Catecholamine-synthesizing enzymes and neuropeptides in rat heart epicardial ganglia; an immunohistochemical study. *Histochem J.* 1990; 22(12): 667–676, doi: [10.1007/BF01047451](https://doi.org/10.1007/BF01047451), indexed in PubMed: 1706694.

2. Kuder T, Tekieli A. Gross and light microscopic studies on the mouse cardiac parasympathetic nervous system. *Zool. Pol.* 2000; 45: 157-167. Not indexed in Pubmed.
3. Rysevaite K, Saburkina I, Pauziene N, et al. Morphologic pattern of the intrinsic ganglionated nerve plexus in mouse heart. *Heart Rhythm.* 2011; 8(3): 448-454, doi: [10.1016/j.hrthm.2010.11.019](https://doi.org/10.1016/j.hrthm.2010.11.019), indexed in Pubmed: [21075216](https://pubmed.ncbi.nlm.nih.gov/21075216/).
4. Hasan W. Autonomic cardiac innervation: development and adult plasticity. *Organogenesis.* 2013; 9(3): 176-193, doi: [10.4161/org.24892](https://doi.org/10.4161/org.24892), indexed in Pubmed: [23872607](https://pubmed.ncbi.nlm.nih.gov/23872607/).
5. Kuder T, Nowak E. Autonomic cardiac nerves: literature review. *Folia Morphol (Warsz).* 2015; 74(1): 1-8, doi: [10.5603/FM.2015.0003](https://doi.org/10.5603/FM.2015.0003), indexed in Pubmed: [25792389](https://pubmed.ncbi.nlm.nih.gov/25792389/).
6. Achanta S, Gorky J, Leung C, et al. A comprehensive integrated anatomical and molecular atlas of rat intrinsic cardiac nervous system. *iScience.* 2020; 23(6): 101140, doi: [10.1016/j.isci.2020.101140](https://doi.org/10.1016/j.isci.2020.101140), indexed in Pubmed: [32460006](https://pubmed.ncbi.nlm.nih.gov/32460006/).
7. Saburkina I, Rysevaite K, Pauziene N, et al. Epicardial neural ganglionated plexus of ovine heart: anatomic basis for experimental cardiac electrophysiology and nerve protective cardiac surgery. *Heart Rhythm.* 2010; 7(7): 942-950, doi: [10.1016/j.hrthm.2010.02.036](https://doi.org/10.1016/j.hrthm.2010.02.036), indexed in Pubmed: [20197118](https://pubmed.ncbi.nlm.nih.gov/20197118/).
8. Day SM, Gu J, Polak JM, et al. Somatostatin in the human heart and comparison with guinea pig and rat heart. *Br Heart J.* 1985; 53(2): 153-157, doi: [10.1136/hrt.53.2.153](https://doi.org/10.1136/hrt.53.2.153), indexed in Pubmed: [2857086](https://pubmed.ncbi.nlm.nih.gov/2857086/).
9. Marron K, Wharton J, Sheppard MN, et al. Human endocardial innervation and its relationship to the endothelium: an immunohistochemical, histochemical, and quantitative study. *Cardiovasc Res.* 1994; 28(10): 1490-1499, doi: [10.1093/cvr/28.10.1490](https://doi.org/10.1093/cvr/28.10.1490), indexed in Pubmed: [8001036](https://pubmed.ncbi.nlm.nih.gov/8001036/).
10. Edwards FR, Hirst GD, Klemm MF, et al. Different types of ganglion cell in the cardiac plexus of guinea-pigs. *J Physiol.* 1995; 486 (Pt 2): 453-471, doi: [10.1113/jphysiol.1995.sp020825](https://doi.org/10.1113/jphysiol.1995.sp020825), indexed in Pubmed: [7473210](https://pubmed.ncbi.nlm.nih.gov/7473210/).
11. Singh S, Johnson P, Lee R, et al. Topography of cardiac ganglia in the adult human heart. *J Thoracic Cardiovasc Surgery.* 1996; 112(4): 943-953, doi: [10.1016/s0022-5223\(96\)70094-6](https://doi.org/10.1016/s0022-5223(96)70094-6), indexed in Pubmed: [8873720](https://pubmed.ncbi.nlm.nih.gov/8873720/).
12. Armour JA, Murphy DA, Yuan BX, et al. Gross and microscopic anatomy of the human cardiac nervous system. *Anat Rec.* 1997; 247: 289-298, doi: [10.1002/\(SICI\)1097-0185\(199702\)247:2<289::AID-AR15>3.0.CO;2-N](https://doi.org/10.1002/(SICI)1097-0185(199702)247:2<289::AID-AR15>3.0.CO;2-N), indexed in Pubmed: [9026008](https://pubmed.ncbi.nlm.nih.gov/9026008/).
13. Pauza D, Skripkiene G, Skripka V, et al. Morphological study of neurons in the nerve plexus on heart base of rats and guinea pigs. *J Auton Nerve Syst.* 1997; 62(1-2): 1-12, doi: [10.1016/s0165-1838\(96\)00102-6](https://doi.org/10.1016/s0165-1838(96)00102-6), indexed in Pubmed: [9021644](https://pubmed.ncbi.nlm.nih.gov/9021644/).
14. Pauza D, Skripka V, Pauziene N, et al. Morphology, distribution, and variability of the epicardial neural ganglionated subplexuses in the human heart. *The Anatomical Record.* 2000; 259(4): 353-382, doi: [10.1002/1097-0185\(20000801\)259:4<353::aid-ar10>3.0.co;2-r](https://doi.org/10.1002/1097-0185(20000801)259:4<353::aid-ar10>3.0.co;2-r), indexed in Pubmed: [10903529](https://pubmed.ncbi.nlm.nih.gov/10903529/).
15. Batulevicius D, Pauziene N, Pauza D. Topographic morphology and age-related analysis of the neuronal number of the rat intracardiac nerve plexus. *Ann Anat - Anatomischer Anzeiger.* 2003; 185(5): 449-459, doi: [10.1016/s0940-9602\(03\)80105-x](https://doi.org/10.1016/s0940-9602(03)80105-x), indexed in Pubmed: [14575272](https://pubmed.ncbi.nlm.nih.gov/14575272/).
16. Pauza D, Pauziene N, Pakeltyte G, et al. Comparative quantitative study of the intrinsic cardiac ganglia and neurons in the rat, guinea pig, dog and human as revealed by histochemical staining for acetylcholinesterase. *Ann Anat - Anatomischer Anzeiger.* 2002; 184(2): 125-136, doi: [10.1016/s0940-9602\(02\)80005-x](https://doi.org/10.1016/s0940-9602(02)80005-x), indexed in Pubmed: [11936191](https://pubmed.ncbi.nlm.nih.gov/11936191/).
17. Singh S, Johnson PI, Javed A, et al. Monoamine- and histamine-synthesizing enzymes and neurotransmitters within neurons of adult human cardiac ganglia. *Circulation.* 1999; 99(3): 411-419, doi: [10.1161/01.cir.99.3.411](https://doi.org/10.1161/01.cir.99.3.411), indexed in Pubmed: [9918529](https://pubmed.ncbi.nlm.nih.gov/9918529/).
18. Weihe E, Schütz B, Hartschuh W, et al. Coexpression of cholinergic and noradrenergic phenotypes in human and nonhuman autonomic nervous system. *J Comp Neurol.* 2005; 492(3): 370-379, doi: [10.1002/cne.20745](https://doi.org/10.1002/cne.20745), indexed in Pubmed: [16217790](https://pubmed.ncbi.nlm.nih.gov/16217790/).
19. Martin L. Chinchillas as experimental models. The laboratory rabbit, guinea pig, hamster, and other rodents. 2012: 1009-1028, doi: [10.1016/b978-0-12-380920-9.00043-2](https://doi.org/10.1016/b978-0-12-380920-9.00043-2).
20. Mikkelsen E, Lauridsen H, Nielsen PM, et al. The chinchilla as a novel animal model of pregnancy. *R Soc Open Sci.* 2017; 4(4): 161098, doi: [10.1098/rsos.161098](https://doi.org/10.1098/rsos.161098), indexed in Pubmed: [28484627](https://pubmed.ncbi.nlm.nih.gov/28484627/).
21. Suckow MA, Stevens KA, Wilson RP. The laboratory rabbit, guinea pig, hamster, and other rodents. 1st ed Saunders: Elsevier 2012.
22. Kuder T, Nowak E, Szczurkowski A, et al. A comparative study on cardiac ganglia in midday gerbil, Egyptian spiny mouse, chinchilla laniger and pigeon. *Anat Histol Embryol.* 2003; 32(3): 134-140, doi: [10.1046/j.1439-0264.2003.00445.x](https://doi.org/10.1046/j.1439-0264.2003.00445.x), indexed in Pubmed: [12823098](https://pubmed.ncbi.nlm.nih.gov/12823098/).
23. Kuchinka J, Chrzanowska M, Kuder T. Adrenergic and cholinergic innervation of the atrioventricular valves in chinchilla (*Chinchilla laniger*). *Folia Morphol (Warsz).* 2017; 76(4): 590-595, doi: [10.5603/FM.a2017.0041](https://doi.org/10.5603/FM.a2017.0041), indexed in Pubmed: [28553858](https://pubmed.ncbi.nlm.nih.gov/28553858/).
24. Radzimirska M, Kuchinka J, Nowak E, et al. Cholinergic and adrenergic innervation of the pancreas in chinchilla (*Chinchilla Laniger Molina*). *Folia Histochem Cytobiol.* 2020; 58(1): 54-60, doi: [10.5603/FHC.a2020.0005](https://doi.org/10.5603/FHC.a2020.0005), indexed in Pubmed: [32202307](https://pubmed.ncbi.nlm.nih.gov/32202307/).
25. Karnovsky MJ, Roots L. A „direct-coloring” thiocholine method for cholinesterases. *J Histochem Cytochem.* 1964; 12: 219-221, doi: [10.1177/12.3.219](https://doi.org/10.1177/12.3.219), indexed in Pubmed: [14187330](https://pubmed.ncbi.nlm.nih.gov/14187330/).
26. Tsuji S, Larabi Y. A modification of thiocholine-ferricyanide method of Karnovsky and Roots for localization of acetylcholinesterase activity without interference by Koelle's copper thiocholine iodide precipitate. *Histochemistry.* 1983; 78(3): 317-323, doi: [10.1007/BF00496619](https://doi.org/10.1007/BF00496619), indexed in Pubmed: [6193086](https://pubmed.ncbi.nlm.nih.gov/6193086/).
27. Torre JCD. An improved approach to histofluorescence using the SPG method for tissue monoamines. *J Neurosci Methods.* 1980; 3(1): 1-5, doi: [10.1016/0165-0270\(80\)90029-1](https://doi.org/10.1016/0165-0270(80)90029-1), indexed in Pubmed: [6164878](https://pubmed.ncbi.nlm.nih.gov/6164878/).
28. Gage GJ, Kipke DR, Shain W. Whole animal perfusion fixation for rodents. *J Vis Exp.* 2012(65), doi: [10.3791/3564](https://doi.org/10.3791/3564), indexed in Pubmed: [22871843](https://pubmed.ncbi.nlm.nih.gov/22871843/).
29. Slaviková J, Kuncová J, Reischig J, et al. Catecholaminergic neurons in the rat intrinsic cardiac nervous system. *Neurochem Res.* 2003; 28: 593-598, doi: [10.1023/a:1022837810357](https://doi.org/10.1023/a:1022837810357), indexed in Pubmed: [12675149](https://pubmed.ncbi.nlm.nih.gov/12675149/).
30. Hasan W, Smith PG. Modulation of rat parasympathetic cardiac ganglion phenotype and NGF synthesis by adrenergic nerves. *Auton Neurosci.* 2009; 145(1-2): 17-26, doi: [10.1016/j.autneu.2008.10.012](https://doi.org/10.1016/j.autneu.2008.10.012), indexed in Pubmed: [19019738](https://pubmed.ncbi.nlm.nih.gov/19019738/).
31. Haberberger R, Kummer W. beta 2-adrenoreceptor immunoreactivity in cardiac ganglia of the guinea pig. *Histochem J.* 1996; 28(11): 827-833, doi: [10.1007/BF02272155](https://doi.org/10.1007/BF02272155), indexed in Pubmed: [8968734](https://pubmed.ncbi.nlm.nih.gov/8968734/).
32. Rysevaite K, Saburkina I, Pauziene N, et al. Immunohistochemical characterization of the intrinsic cardiac neural plexus

- in whole-mount mouse heart preparations. *Heart Rhythm*. 2011; 8(5): 731–738, doi: [10.1016/j.hrthm.2011.01.013](https://doi.org/10.1016/j.hrthm.2011.01.013), indexed in Pubmed: [21232628](https://pubmed.ncbi.nlm.nih.gov/21232628/).
33. Richardson RJ, Grkovic I, Anderson CR. Immunohistochemical analysis of intracardiac ganglia of the rat heart. *Cell Tissue Res*. 2003; 314(3): 337–350, doi: [10.1007/s00441-003-0805-2](https://doi.org/10.1007/s00441-003-0805-2), indexed in Pubmed: [14523644](https://pubmed.ncbi.nlm.nih.gov/14523644/).
 34. Pauziene N, Alaburda P, Rysevaite-Kyguoliene K, et al. Innervation of the rabbit cardiac ventricles. *J Anat*. 2016; 228(1): 26–46, doi: [10.1111/joa.12400](https://doi.org/10.1111/joa.12400), indexed in Pubmed: [26510903](https://pubmed.ncbi.nlm.nih.gov/26510903/).
 35. Calupca MA, Locknar SA, Zhang L, et al. Distribution of cocaine- and amphetamine-regulated transcript peptide in the guinea pig intrinsic cardiac nervous system and colocalization with neuropeptides or transmitter synthetic enzymes. *J Comp Neurol*. 2001; 439(1): 73–86, doi: [10.1002/cne.1336](https://doi.org/10.1002/cne.1336), indexed in Pubmed: [11579383](https://pubmed.ncbi.nlm.nih.gov/11579383/).
 36. Scruggs P, Dun SL, Dun NJ. Cocaine- and amphetamine-regulated transcript peptide attenuates phenylephrine-induced bradycardia in anesthetized rats. *Am J Physiol Regul Integr Comp Physiol*. 2003; 285(6): R1496–R1503, doi: [10.1152/ajpregu.00183.2003](https://doi.org/10.1152/ajpregu.00183.2003), indexed in Pubmed: [12933358](https://pubmed.ncbi.nlm.nih.gov/12933358/).
 37. Richardson RJ, Grkovic I, Anderson CR. Cocaine- and amphetamine-related transcript peptide and somatostatin in rat intracardiac ganglia. *Cell Tissue Res*. 2006; 324(1): 17–24, doi: [10.1007/s00441-005-0087-y](https://doi.org/10.1007/s00441-005-0087-y), indexed in Pubmed: [16374620](https://pubmed.ncbi.nlm.nih.gov/16374620/).
 38. Mao P, Meshul C, Thuillier P, et al. CART Peptide is a potential endogenous antioxidant and preferentially localized in mitochondria. *PLoS ONE*. 2012; 7(1): e29343, doi: [10.1371/journal.pone.0029343](https://doi.org/10.1371/journal.pone.0029343), indexed in Pubmed: [22235287](https://pubmed.ncbi.nlm.nih.gov/22235287/).
 39. Horackova M, Armour JA, Byczko Z. Distribution of intrinsic cardiac neurons in whole-mount guinea pig atria identified by multiple neurochemical coding. A confocal microscope study. *Cell Tissue Res*. 1999; 297(3): 409–421, doi: [10.1007/s004410051368](https://doi.org/10.1007/s004410051368), indexed in Pubmed: [10460488](https://pubmed.ncbi.nlm.nih.gov/10460488/).
 40. Moravec M, Moravec J, Forsgren S. Catecholaminergic and peptidergic nerve components of intramural ganglia in the rat heart. An immunohistochemical study. *Cell Tissue Res*. 1990; 262(2): 315–327, doi: [10.1007/BF00309887](https://doi.org/10.1007/BF00309887), indexed in Pubmed: [1706221](https://pubmed.ncbi.nlm.nih.gov/1706221/).
 41. Parsons RL, Locknar SA, Young BA, et al. Presence and co-localization of vasoactive intestinal polypeptide with neuronal nitric oxide synthase in cells and nerve fibers within guinea pig intrinsic cardiac ganglia and cardiac tissue. *Cell Tissue Res*. 2006; 323(2): 197–209, doi: [10.1007/s00441-005-0074-3](https://doi.org/10.1007/s00441-005-0074-3), indexed in Pubmed: [16220273](https://pubmed.ncbi.nlm.nih.gov/16220273/).
 42. Steele PA, Gibbins IL, Morris JL, et al. Multiple populations of neuropeptide-containing intrinsic neurons in the guinea-pig heart. *Neuroscience*. 1994; 62(1): 241–250, doi: [10.1016/0306-4522\(94\)90327-1](https://doi.org/10.1016/0306-4522(94)90327-1), indexed in Pubmed: [7816202](https://pubmed.ncbi.nlm.nih.gov/7816202/).
 43. Odorizzi M, Fernetto B, Angel E, et al. Galanin receptor antagonists decrease fat preference in Brattleboro rat. *Neuropharmacology*. 2002; 42(1): 134–141, doi: [10.1016/s0028-3908\(01\)00115-0](https://doi.org/10.1016/s0028-3908(01)00115-0), indexed in Pubmed: [11750923](https://pubmed.ncbi.nlm.nih.gov/11750923/).
 44. Diaz Z, Narváez J, Hedlund P, et al. Centrally infused galanin-(1–15) but not galanin-(1–29) reduces the baroreceptor reflex sensitivity in the rat. *Brain Research*. 1996; 741(1–2): 32–37, doi: [10.1016/s0006-8993\(96\)00883-9](https://doi.org/10.1016/s0006-8993(96)00883-9), indexed in Pubmed: [9001701](https://pubmed.ncbi.nlm.nih.gov/9001701/).
 45. Herring N, Cranley J, Lokale MN, et al. The cardiac sympathetic co-transmitter galanin reduces acetylcholine release and vagal bradycardia: implications for neural control of cardiac excitability. *J Mol Cell Cardiol*. 2012; 52(3): 667–676, doi: [10.1016/j.yjmcc.2011.11.016](https://doi.org/10.1016/j.yjmcc.2011.11.016), indexed in Pubmed: [22172449](https://pubmed.ncbi.nlm.nih.gov/22172449/).
 46. Crick SJ, Anderson RH, Ho SY, et al. Localisation and quantitation of autonomic innervation in the porcine heart II: endocardium, myocardium and epicardium. *J Anat*. 1999; 195 (Pt 3): 359–373, doi: [10.1046/j.1469-7580.1999.19530359.x](https://doi.org/10.1046/j.1469-7580.1999.19530359.x), indexed in Pubmed: [10580851](https://pubmed.ncbi.nlm.nih.gov/10580851/).
 47. Gordon L, Wharton J, Gaer JA, et al. Quantitative immunohistochemical assessment of bovine myocardial innervation before and after cryosurgical cardiac denervation. *Cardiovasc Res*. 1993; 27(2): 318–326, doi: [10.1093/cvr/27.2.318](https://doi.org/10.1093/cvr/27.2.318), indexed in Pubmed: [8097135](https://pubmed.ncbi.nlm.nih.gov/8097135/).
 48. Anker SD. Catecholamine levels and treatment in chronic heart failure. *Eur Heart J*. 1998; 19 Suppl F: F56–F61, indexed in Pubmed: [9651737](https://pubmed.ncbi.nlm.nih.gov/9651737/).
 49. Adameova A, Abdellatif Y, Dhalla NS. Role of the excessive amounts of circulating catecholamines and glucocorticoids in stress-induced heart disease. *Can J Physiol Pharmacol*. 2009; 87(7): 493–514, doi: [10.1139/y09-042](https://doi.org/10.1139/y09-042), indexed in Pubmed: [19767873](https://pubmed.ncbi.nlm.nih.gov/19767873/).

Submitted: 2 June, 2021

Accepted after reviews: 23 September, 2021

Available as AoP: 28 September, 2021

Short-term fenofibrate treatment improves ultrastructure of hepatocytes of old rats

Adrian Zubrzycki, Agata Wronska, Agata Zauszkiewicz-Pawlak, Zbigniew Kmiec

Department of Histology, Medical University of Gdansk, Gdansk

Abstract

Introduction. Fenofibrate (FN) is a hypolipemic drug used for the treatment of mixed dyslipidemia. Since in our previous study FN administration to young and old rats adversely affected the serum activity of liver marker enzymes, we decided to examine the effects of FN on liver ultrastructure of young and old animals.

Material and methods. Young and old rats were fed standard rodent chow supplemented with 0.1% FN for 30 days. Liver samples obtained from animals under full anesthesia were processed by routine methods to obtain ultrathin and histological sections for the examination by light microscopy (LM) and transmission electron microscopy (TEM). Furthermore, liver lysates were analyzed by Western blotting for the expression of the autophagy-related proteins LC3A/B and beclin 1.

Results. The ultrastructure of hepatocytes in both age groups was well-preserved, with the presence of abundant mitochondria, numerous peroxisomes and lysosomes, glycogen stored in the form of rosettes, and occasionally autolysosomes. However, hepatocytes of old control rats contained less mitochondria and peroxisomes, and more lipid droplets than cells of young animals. The effects of FN on liver ultrastructure were age-dependent. FN increased the relative number of mitochondria and peroxisomes in the hepatocytes of old, and did not affect their number in young rats. Moreover, FN decreased and increased the relative number of lipid droplets in the hepatocytes of old and young rats, respectively. At the LM level, Oil Red O staining revealed smaller and larger lipid droplets within hepatocytes and non-parenchymal liver cells. In the livers of young and old rats lipid droplets were distributed mainly in the periportal zones of hepatic lobules. Morphometric analysis confirmed that livers of control old rats contained more lipid-stainable areas than those of young ones; however, no effect of FN was observed either in young or old rats. Despite larger size of autolysosomes and autophagic vacuoles in hepatocytes of old rats, the expression of autophagy-related proteins did not differ in the livers of control and fenofibrate-treated young and old animals.

Conclusions. The results of our study suggest that fenofibrate, apart from its hypolipemic action, may have beneficial effect on the energy metabolism in the liver of old individuals by increasing the number of mitochondria and peroxisomes in hepatocytes. (*Folia Histochemica et Cytobiologica* 2021, Vol. 59, No. 3, 167–177)

Key words: fenofibrate; aging; rat; liver; hepatocyte; lipid droplets; LC3A/B; beclin 1; TEM

Introduction

Fenofibrate (FN) has been used to correct lipid abnormalities in patients with dyslipidemias [1, 2].

Hypolipemic effects of FN are related to the activation of a class of intracellular receptors, known as peroxisome proliferator-activated receptors (PPARs), especially PPAR α in the liver [3]. These receptors modulate carbohydrate and lipid metabolism by the up- or downregulation of the transcription of multiple genes that are responsible for the regulation of hepatic lipid metabolism [4, 5].

Depending on the dose, FN can induce adverse side effects in the liver [6, 7]. In our previous work we showed that, apart from beneficial effects on the

Correspondence address: Adrian Zubrzycki, MSc
Medical University of Gdansk,
Department of Histology,
1 Debinki Str., 80–211 Gdansk, Poland
e-mail: adrian.zubrzycki@gumed.edu.pl

levels of serum lipids, FN administration for 30 days to young and old rats was associated with alterations of liver histological structure and increased blood serum activity of alkaline phosphatase [8]. Other studies showed that PPAR α activation by fibrates induces in rodents strong proliferation of peroxisomes, resulting in hyperplasia and hypertrophy of hepatocytes [9–12]. In liver-specific humanized PPAR α transgenic mice, FN caused proliferation of liver cells and hepatocyte hypertrophy, dependent on the dose and duration of FN treatment [12]. Moreover, PPAR α activation decreased apoptosis in an experimental rat cholestasis model [9]. However, the effects of PPAR α ligands, such as FN, on hepatocyte and peroxisome proliferation differ between rodents and humans [13].

Even though biological effects of FN have been studied almost for forty years, there is scarcity of data on age-dependent effects of the drug. In our previous study performed on old and young rats we found, beside the expected hypolipemic action of FN, also some indices of adverse effects of FN on the liver function and structure at the light-microscopic level. Therefore, in the present study we decided to compare FN's effects on hepatocytes' ultrastructure in young and old healthy Wistar-Han rats, and on the expression of autophagy-related proteins, *i.e.* LC3A/B which is related to autophagosome formation, and beclin 1, a common regulator of autophagy and apoptosis [14].

Materials and methods

Animals. The experiment was carried out on young (4-month-old) and old (24-month-old) male Wistar-Han rats, bred in the Academic Animal Experimental Center in Gdansk, Poland, and housed one *per* cage in standard breeding conditions (22 \pm 2°C, humidity 55 \pm 10%, 12h/12h light/dark cycle). The experimental procedures were approved by the Local Ethics Committee in Bydgoszcz, Poland (protocols No. 41/2017, 58/2017, 40/2018, and 5/2019), and carried out accordingly.

Administration of FN and material sampling for electron and light microscopy. Young and old rats were fed either standard rodent chow (Labofeed H, Wytworknia Pasz Morawski, Kcynia, Poland) (control animals) or the same chow supplemented with 0.1% FN (Glentham Life Sciences, Corsham, UK) (FN-treated group). For electron microscopy studies, two young and two old animals from each group were anesthetized using ketamine 90 mg/kg and xylazine 10 mg/kg, *i.p.* The heart was exposed by slitting the chest and a perfusion needle was inserted into the left ventricle of the heart. At the same time, the continuity of veins falling into the right atrium of the heart was broken. First, a 0.9% NaCl solution with 500 units of heparin to prevent

blood clotting was injected in order to rinse blood from the circulatory system. Then, a fixative (2.5% glutaraldehyde in 0.1 M phosphate buffer (pH 7.4)) was administered (approx. 400 ml per 250 g of animal weight). In the first phase, the fixer was pressed in faster mode (10 ml/min), and then the pump flow was halved. After perfusion, the fixative was removed from the pump tubing by rinsing it with saline solution. Liver samples (approx. 1 mm³) were collected and immediately placed in the same fixative solution before further processing. For light microscopy examination, three animals per group were sacrificed under full anesthesia (ketamine 90 mg/kg and xylazine 10 mg/kg, *i.p.*) through exsanguination from heart puncture, followed by decapitation. Liver samples were collected and immediately frozen in liquid nitrogen for further processing.

Transmission electron microscopy. For ultrastructural examination of hepatocytes, the liver samples of two rats from each group were analyzed. After overnight fixation in 2.5% glutaraldehyde in 0.1 M phosphate buffer (pH 7.4), tissues were treated with 1% osmium tetroxide in 0.12 M phosphate buffer and embedded in epon resin (Sigma-Aldrich, St. Louis, MO, USA). Ultrathin sections (70 nm) were cut and, after dehydration, stained with uranyl acetate (Plano GmbH, Wetzlar, Germany) and lead citrate (Electron Microscopy Sciences, Hatfield, PA, USA). Samples were analyzed with a transmission electron microscope (JEOL JEM-1200 EX II, University Park, PA, USA) at an acceleration voltage of 80 kV.

Oil Red O staining. Seven- μ m-thick frozen liver sections of three rats per group were obtained using a cryostat (Leica CM1950, Kawaska, Warsaw, Poland), and mounted on glass slides (SuperFrost Ultra Plus, Thermo Scientific, Vantaa, Finland). The sections were briefly washed in dH₂O, PBS-buffered 4% paraformaldehyde for 1 min, and briefly in absolute alcohol. Then, the sections were incubated in fresh-diluted 0.5% Oil Red O solution in isopropyl alcohol (Sigma-Aldrich) for 12 min, briefly washed in dH₂O, and incubated in Harris's hematoxylin solution (Sigma-Aldrich) for 5 s, briefly washed in dH₂O and 80% ethanol solution, and embedded in glycerol (Sigma-Aldrich).

Morphometric studies. In the samples of the liver from each group of animals the cytoplasm of randomly selected hepatocytes located in various regions of the ultrathin sections was outlined and its area was measured with the use of the ImageJ software (NIH, Bethesda, MD, USA). Thereafter, the number of mitochondria, peroxisomes, and lipid droplets in chosen area was counted. Basically, the morphometry was performed at the magnification of 10,000 \times and 15,000 \times . The results are shown as the number of the listed structures *per* unit area of the cytoplasm expressed in square micrometers.

For the measurement of relative content of lipid droplets in liver samples, two non-contiguous sections from three rats *per* each group were analyzed, in three to five randomly-selected view fields at the 20× objective magnification in each section. Microphotographs were obtained using Olympus BX43 microscope equipped with an Olympus UC 90 digital camera (Olympus, Tokyo, Japan).

The relative area occupied in the Oil Red O stained sections by the lipid droplets were analyzed using the cellSens Dimension Software (Olympus, Tokyo, Japan).

Western blotting. The semi-quantification of LC3A/B and beclin 1 proteins in the liver was performed by Western blotting (WB) in 4 samples from every group. Whole-cell lysates were obtained using the Mammalian Cell Extraction Kit (BioVision, Milpitas, CA, USA) and 20 µg protein samples were separated on 10% SDS-PAGE gels, transferred to PVDF membranes (Bio-Rad, Warsaw, Poland), and blocked with 7% non-fat milk in TBS with 0.1% Tween20 (TBST) for 1.5 h. The membranes were incubated overnight at 4°C with anti-LC3A/B (Santa Cruz Biotechnology, Dallas, Texas) or anti-beclin 1 (Santa Cruz Biotechnology, Dallas, TX, USA) rabbit polyclonal antibodies at 1:1,000 dilution in 3% non-fat milk in TBST. Thereafter, the membranes were incubated with HRP-conjugated anti-rabbit secondary antibodies (Sigma-Aldrich) at 1:10,000 dilution in 3% non-fat milk in TBST for 2 h at room temperature. Bands were visualized using Clarity Western ECL Substrate (Bio-Rad) and developed using ImageQuant LAS 500 Chemiluminescence CCD Camera (GE Healthcare Life Sciences, Pittsburgh, PA, USA). LC3A/B and beclin1 protein levels were analyzed relative to glyceraldehyde 3-phosphate dehydrogenase (GAPDH) levels (1:50,000 antibody dilution in 3% non-fat milk in TBST; Sigma-Aldrich) using QuantityOne Software (Bio-Rad).

Statistical analysis. Statistical analyses were performed using GraphPad Prism v. 3.0 software (GraphPad Inc., San Diego, CA, USA). After applying Shapiro-Wilk test for normality and Grubbs test for outliers, statistical analyses were performed using Student *t*-test (for relative area density of organelles and relative area of lipid droplets) or non-parametric Kruskal-Wallis ANOVA (for proteins' expression in WB). Data are presented as mean ± SD. Statistical significance was set at $p < 0.05$.

Results

Ultrastructure of hepatocytes of young and old rats

In control young rats, electron microscopy revealed well-preserved ultrastructure of hepatocytes. The cells presented normal structure of numerous mitochondria, abundant rough endoplasmic reticulum (RER), and numerous peroxisomes and lysosomes (Figs. 1B and 2B; [Suppl. Figs. 2 and 4](#)), glycogen stored in a form of 'rosettes' (Figs. 1B and 2A; [Suppl. Fig. 4](#)) and

lipid droplets ([Suppl. Figs. 1 and 3](#)). Some hepatocytes in the liver of young rats were binucleated (Fig. 1A; [Suppl. Fig. 2](#)).

In control old rats, electron microscopy revealed, similarly to young ones, well-preserved ultrastructure of hepatocytes (Figs. 1C, 1D, 2C, and 2D). However, in comparison to young animals, hepatocytes of old control animals contained relatively more electron-dense mitochondria (Figs. 1C, 1D, 2C, and 2D), well-developed RER (Figs. 1D, 2C; [Suppl. Figs. 5 and 6](#)), and some autolysosomes (Figs. 1C and 2D; [Suppl. Figs. 6 and 8](#)). Moreover, hepatocytes of control old rats appeared to have more lipid droplets (Fig. 1D), peroxisomes (Fig. 2D; [Suppl. Fig. 8](#)) and glycogen 'rosettes' (Figs. 2C and 2D; [Suppl. Figs. 6 and 7](#)) than hepatocytes of young animals. Binucleated and polyploid hepatocytes seemed to occur more often in the liver of old rats (Fig. 1C).

In comparison to young control animals, hepatocytes of FN-treated young rats revealed numerous mitochondria with more electron-dense matrix (Fig. 3A; [Suppl. Figs. 9 and 10](#)), more peroxisomes and lysosomes (Figs. 3A, 3B, and 4B; [Suppl. Figs. 9 and 10](#)) and occasionally autophagosomes ([Suppl. Fig. 9](#)) and autophagic vacuoles (Fig. 4A). Some lipid droplets were also seen (Fig. 4A). Interestingly, the intercellular spaces were distended (Fig. 3A).

In comparison to old control animals, hepatocytes of FN-treated old rats appeared to have more mitochondria, peroxisomes, lysosomes, RER cisternae (Figs. 3C and 3D; [Suppl. Figs. 11](#)) and glycogen 'rosettes' (Figs. 4C and 4D). Compared with the hepatocytes of control rats, the number of lipid droplets seemed to be lower in the cells of FN-treated old animals (Fig. 3C; [Suppl. Fig. 11](#)) whereas the content of autophagosomes and autolysosomes seemed to be more variable (Figs. 4C and 4D).

In the livers of both control and FN-treated young and old rats, hepatocytes were connected by numerous junctional complexes with prominent desmosomes (Figs. 1D and 3C; [Suppl. Figs. 5 and 11](#)).

Morphometric analysis at the electron microscopic level

Because the qualitative analysis of electron-microscopic photographs suggested the presence of some age- or FN-related changes in the number of hepatocytes' organelles, we performed semi-quantitative morphometric analysis to determine relative area density of mitochondria, peroxisomes, and lipid droplets in hepatocytes of each experimental group.

We found that in the hepatocytes of old control rats the relative number of mitochondria and peroxisomes was lower by 29% ($p < 0.05$) and 57% ($p < 0.05$), respectively, than in hepatocytes of con-

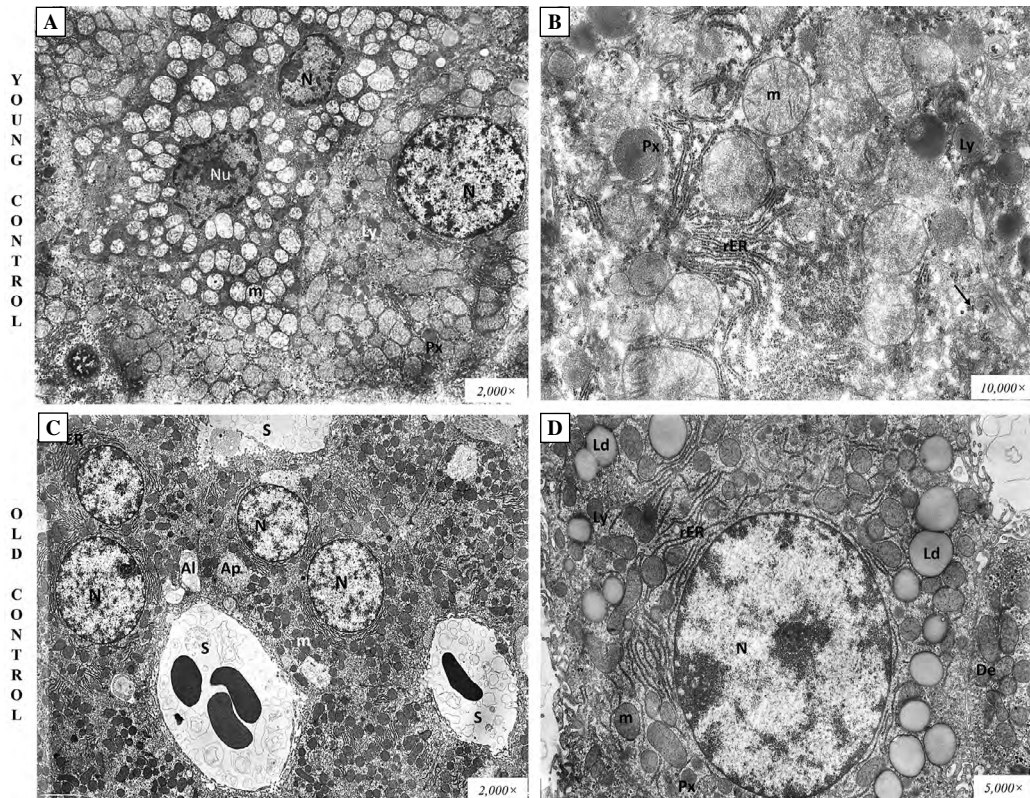


Figure 1. EM micrographs of hepatocytes of control young and old rats at lower magnifications. Abbreviations: Al — autolysosome; Ap — autophagosome; col — collagen fibers; De — desmosome; Ld — lipid droplet; Ly — lysosome; m — mitochondrion; N — nucleus; Px — peroxisome; rER — rough endoplasmic reticulum; S — sinusoid; arrow, glycogen rosette.

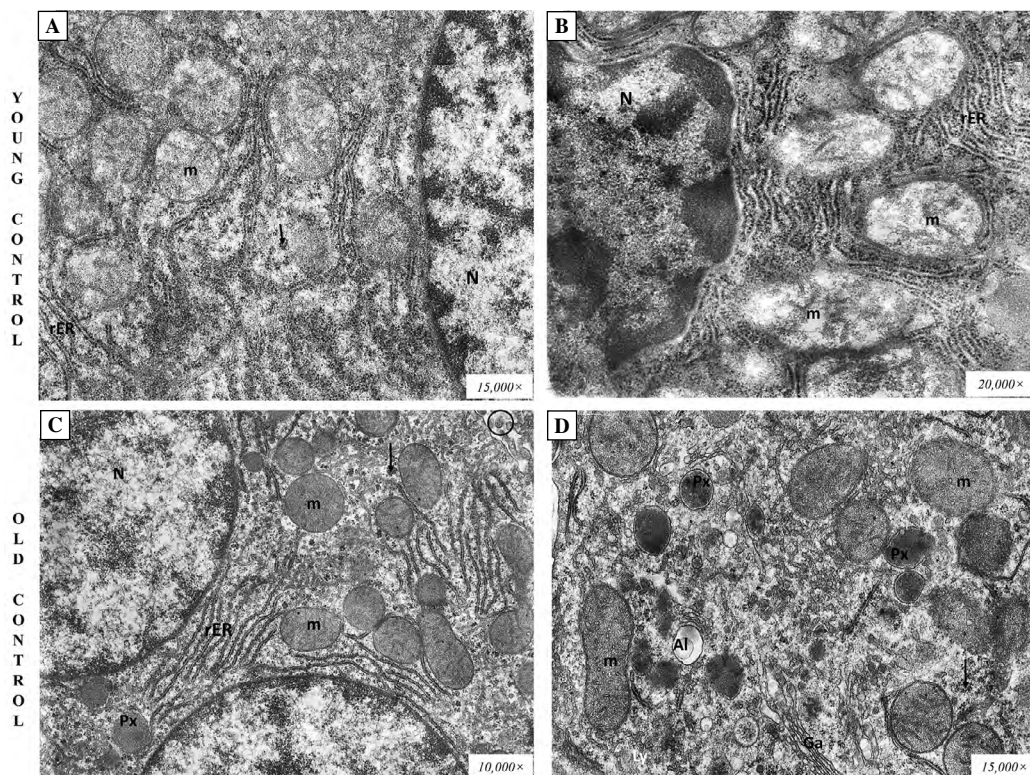


Figure 2. EM micrographs of hepatocytes of control young and old rats at higher magnifications. Abbreviations as in the description of Figure 1 and: Ga — Golgi apparatus, black circle — bile canaliculus.

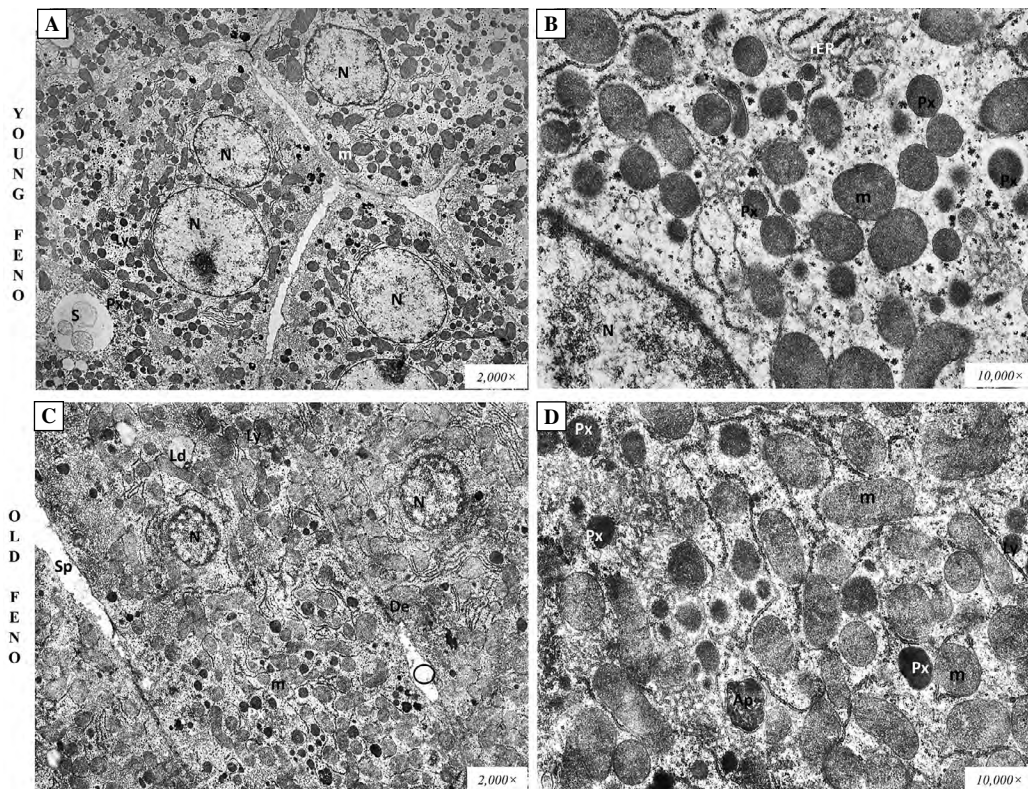


Figure 3. EM micrographs of hepatocytes of FN-treated (feno) young and old rats at lower magnifications. Abbreviations as in the description of Figure 1 & 2: Ap — autophagosome; Sp — lateral recess of the space of Disse.

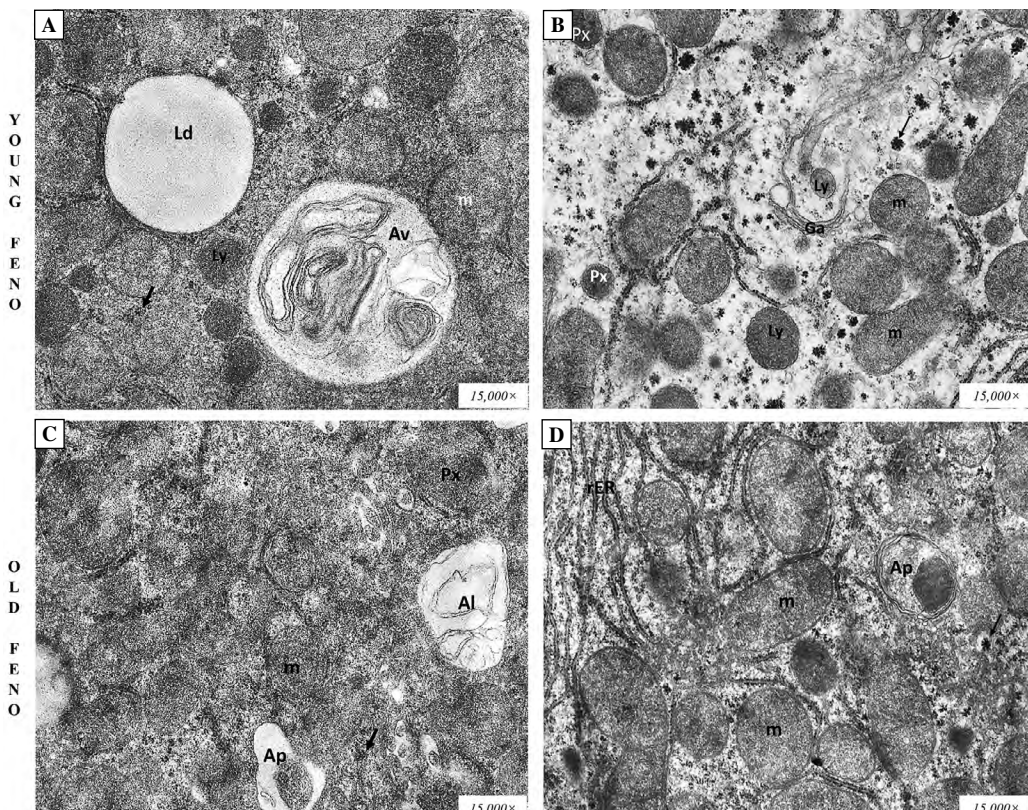


Figure 4. EM micrographs of hepatocytes of FN-treated (feno) young and old rats at higher magnification. Abbreviations as in the description of Figures 1, 2 and 3.

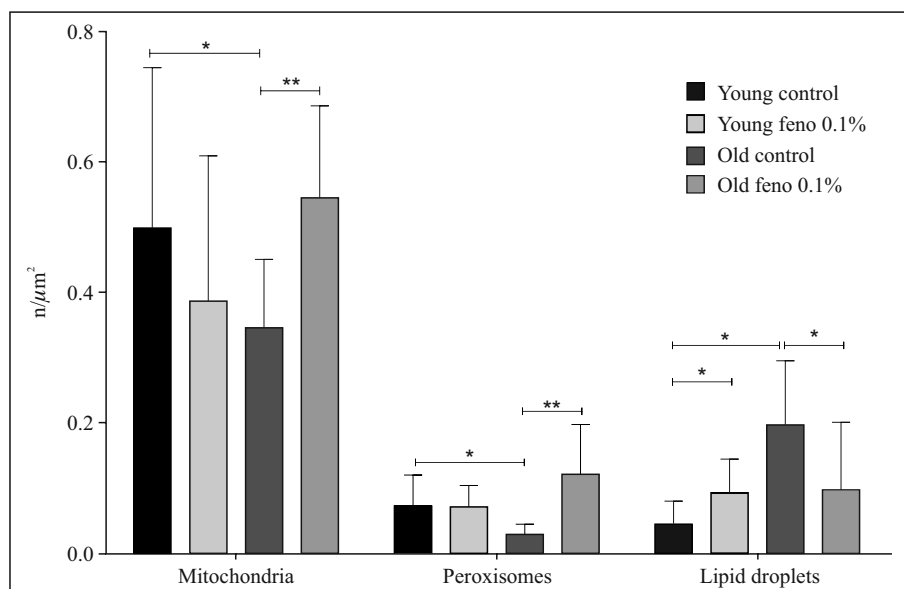


Figure 5. Relative area density of mitochondria, peroxisomes, and lipid droplets in hepatocytes of young and old control and FN-treated (feno) rats measured at the ultrastructural level and expressed as number of organelles per μm^2 . Data are presented as mean \pm SD, $n = 2$ per group, * $p < 0.05$, ** $p < 0.01$ (Student's *t*-test).

trol young rats. FN treatment increased the number of mitochondria and peroxisomes in hepatocytes of old rats by 57% and 300%, respectively ($p < 0.05$ and $p < 0.01$). However, FN did not affect the number of mitochondria or peroxisomes in hepatocytes of young rats (Fig. 5).

We also found that in hepatocytes of control old rats the relative number of lipid droplets was 3-fold higher than in cells of young animals ($p < 0.01$) (Fig. 5). FN treatment decreased the number of lipid droplets by 50% ($p < 0.05$) in hepatocytes of old rats, and increased it by 50% in cells of young animals (Fig. 5).

Relative content of lipid droplets measured in liver sections stained by Oil Red O

The heterogeneity of the liver lobule has been described for some basic metabolic pathways [15, 16]. Since our EM study had basically qualitative character and the sampled pieces of liver tissue were derived from the middle part of classic hepatic lobules (zone 2 of portal lobule), we decided to test the expression of lipid droplets across the liver lobule in cryostat sections stained with Oil Red O. This method made it possible to assess semi-quantitatively the relative area occupied by lipid droplets in the liver sections. In the livers of control both young and old rats, Oil Red O staining revealed the presence of lipid droplets mainly in the hepatocytes of the periportal zone of the classic hepatic lobule (zone 1 of portal lobule); however, the intensity of the staining reaction was much higher in the liver of old rats (Fig. 6).

The FN treatment resulted in more homogenous distribution of lipid droplets within hepatic lobules and seemingly lower staining intensity (Fig. 6B, D) which prompted us to assess drug's action by a morphometric method. It revealed that the relative area density of lipid droplets was higher in the liver of control old rats by 371% ($p < 0.01$) than in young ones. The treatment of both young and old rats with 0.1% FN did not cause any significant changes in the area density of lipid droplets in young and old rats ($p > 0.05$) (Fig. 6E).

Expression of pro-autophagic proteins LC3A/B and beclin 1

One of the features of cell senescence is decreased number of autophagic structures/vacuoles [17]. Western blot method was used to assess the relative levels of LC3A/B and beclin 1 proteins in the homogenates of rat livers. We did not observe any age-related changes, although there was a notable tendency towards lower expression of LC3A/B and increased expression of beclin 1 in control old rats as compared to young ones. The FN treatment was not associated with any significant changes in the expression levels of autophagy-related proteins LC3A/B and beclin 1 in the liver of either young and old rats (Fig. 7).

Discussion

Fenofibrate has been approved for treating dyslipidemias; however, its effects on the liver ultrastructure in

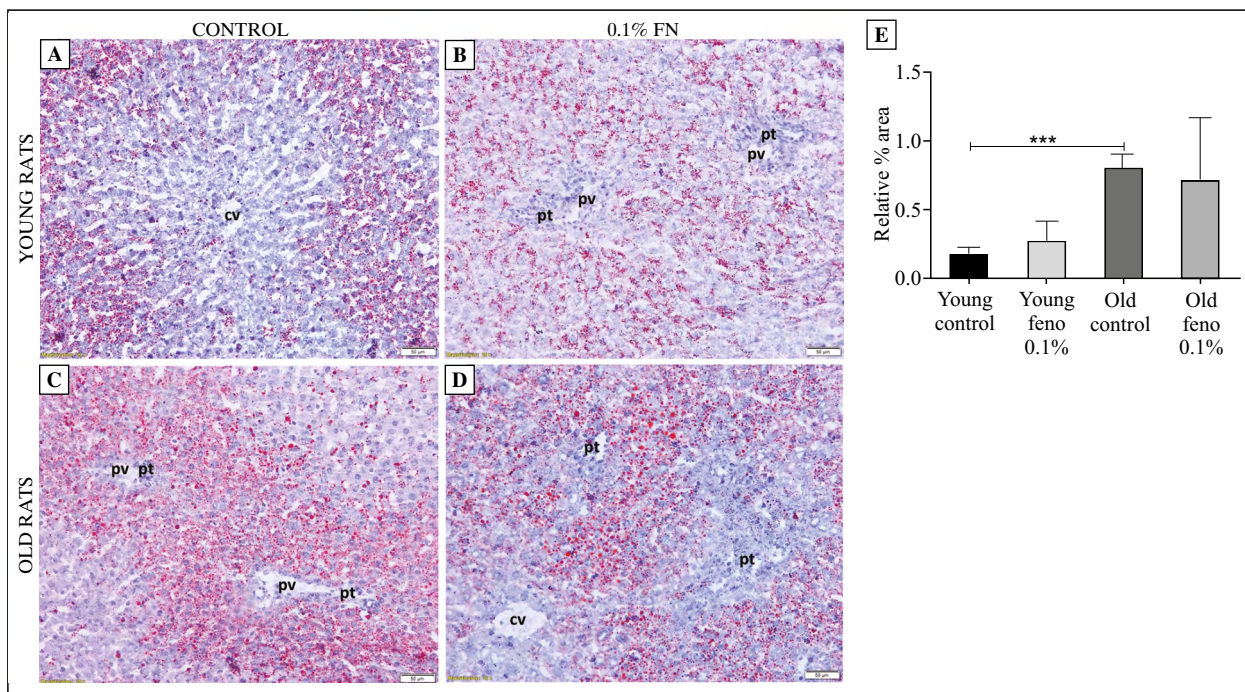


Figure 6. Oil Red O staining of the liver of control and FN-treated (feno) young and old rats. The most representative microphotographs at 200× magnification are shown (A–D). Relative area of lipid droplets (E) was assessed; data are presented as mean ± SD of 3 animals per group, ***p < 0.01 (Student *t*-test).

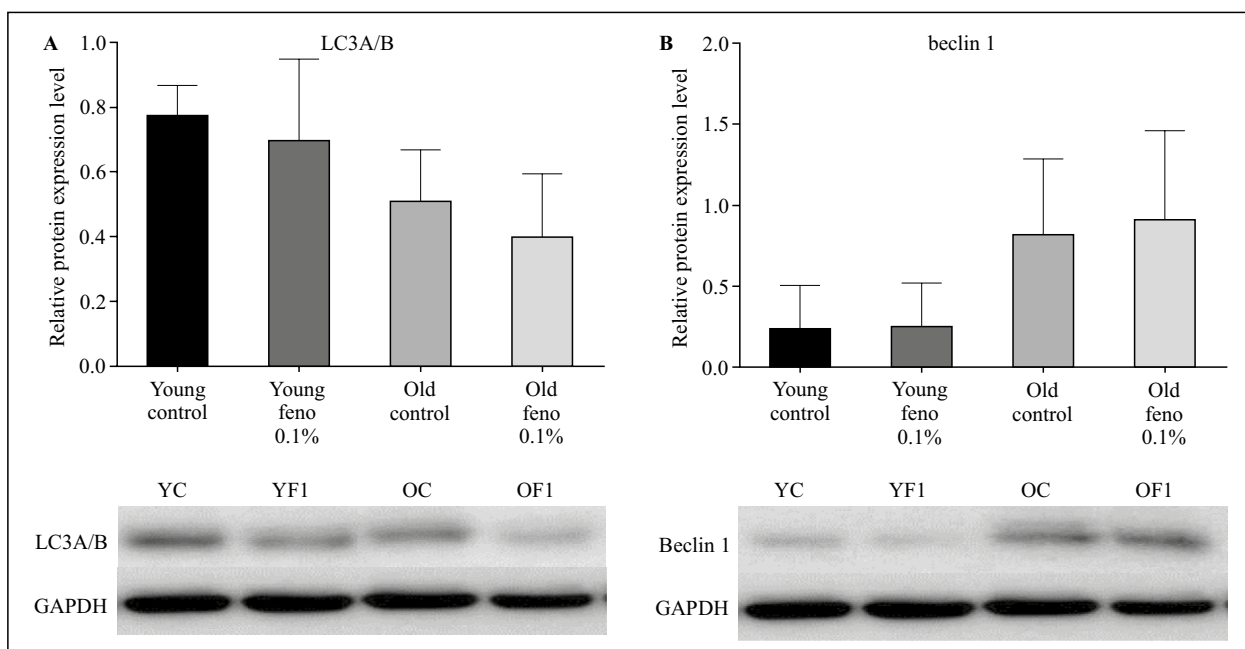


Figure 7. Protein expression of LC3A/B and beclin 1 in the liver of control and FN-treated (feno) young and old rats. Relative protein levels were determined by Western blotting. Representative blots are shown. Data are presented as mean ± SD, 4 animals per group. No significant changes were found ($p > 0.05$). Abbreviations: YC — control young rats; YF1 — young rats treated with 0.1% FN; OC — control old rats; OF1 — old rats treated with 0.1% FN (Kruskal-Wallis ANOVA).

the context of aging have not been thoroughly investigated. Our study revealed some important differences in the submicroscopic structure of hepatocytes of

young and old male rats which were subjected to short-term, 30-day-long FN treatment. We suggest that it may reflect changes in liver function, as indicated by

changes in biochemical serum parameters and liver morphology described in our previous report [8].

It has been showed that aging in rodents is associated with some decline of mitochondrial function with mitochondria from old mice characterized by less regular and more heterogeneous cristae not arranged in parallel stacks [18], and increased content of oxidation products of phospholipids, proteins and DNA, decreased membrane potential, and increased mitochondrial size and fragility [19]. It was revealed that aging in rodents [20–22] and humans [22] is associated with the increase in individual mitochondrial volume and decline in the number of mitochondria in the liver. These findings are supported by our observation of the increased matrix electron density of mitochondria in hepatocytes of old rats. Our finding of the lower relative number of mitochondria in hepatocytes of control old rats as compared to young ones was reported by some, however not all, investigators. *E.g.* much higher decline (3.5 times) was found in the relative number of mitochondrial profiles in the livers of 24-month-old control mice as compared with 6-month old animals [23]. In hepatocytes isolated from 22–23 and 32–36 month-old Wistar rats the number of mitochondria per cell was similar; however, mitochondria of old animals were larger than mitochondria in hepatocytes of 3–4 month-old rats that was explained by age-related increase in mitochondrial matrix volume [24]. Electron cryotomography showed that in the mitochondria isolated from the livers of old (80–96-week-old) mice mitochondrial cristae were less regular and not arranged in parallel stacks, less interconnected, generally wider and not spanning the entire mitochondrion in comparison with mitochondria from livers of 20-week-old animals [18]. Łysek-Gładysińska *et al.* observed increased number of damaged mitochondria in the hepatocytes of 17-month-old mice as compared to 6-month old animals [21]. Interestingly, no age-dependent increase in hydrogen peroxide release relative to the amount of oxygen consumed was observed in the isolated murine liver mitochondria [18].

The short-term FN treatment of old rats resulted in the appearance more electron-dense mitochondria in hepatocytes of both young and old animals than in control ones. Moreover, FN increased relative number of mitochondria only in hepatocytes of old rats that was lower in control old animals as compared to young ones. Since mitochondria play a major role in the energy homeostasis, this novel observation may indicate beneficial effect of FN that upregulated age-related decline of the number of mitochondria in rat hepatocytes.

Peroxisomes, abundant in cells that are involved in lipid and xenobiotics metabolism, play a major role

in the breakdown of long-chain fatty acids, thereby complementing mitochondrial fatty-acid oxidation [25]. In our study we demonstrated that the age is associated with the decrease in relative number of peroxisomes in hepatocytes, and FN administration increases the relative number of peroxisomes only in hepatocytes of old rats. Together with the effect of FN on the relative number of mitochondria in hepatocytes of old rats this finding suggests beneficial effects of FN on the hepatic lipid and energy metabolism in aged rodents. Although FN was shown to increase the number of peroxisomes in the liver of juvenile (5-week-old) male Wistar rats after two weeks of 0.1% FN administration [26], this effect was not observed by us in the liver of adult, sexually mature animals. The discrepancy between our data and those of the other authors could be attributed to differences between rat strains [26, 27]. For example, in the liver of 27-month-old male Fischer 344 rats, clofibrac acid, one of the model fibrates, induced only slight proliferation of peroxisomes [28]. Moreover, FN did not cause proliferation of peroxisomes in the liver of rhesus monkeys (treatment with 200 mg/kg body weight/day FN for 12 months) [29]. It is also possible that the chosen dose of FN or the duration of its administration were too short to induce proliferation of peroxisomes in hepatocytes of young and old rat.

It is widely known that aging is associated with lipid accumulation in the liver [30]. In our study we reveal that old age of rats was associated with the increase in relative number of lipid droplets within single hepatocytes and in liver sections at the light microscopy level. Similar increase in lipid droplets were found in the liver of aging mice [21, 31]. Interestingly, in Fischer 344 male rats the volume of lipid droplets in hepatocytes undergoes a biphasic response during aging, *i.e.* gradual post-maturational increase is followed by the decline during late senescence [22, 32]. The beneficial effect of FN on the relative number of lipid droplets in hepatocytes of old rats was not observed in young animals in whom only a slight increase was found. This discrepancy may be caused by originally higher content of lipid droplets in old hepatocytes and, probably, increased sensitivity of old rats' hepatocytes to the action of FN, as observed also for the relative number of mitochondria and peroxisomes. In contrast to these ultrastructural observations, FN did not alter the relative area occupied by lipid droplets detected by Oil Red O staining at the light microscopy level. This may be due to the accumulation of lipid vacuoles in hepatic stellate cells which were not analyzed by electron-microscopy morphometry. We are not aware of any studies that investigated effects of FN on the liver fat-storing (or Ito) cells. Similar effect was observed

in hyperlipidemic patients with the presence of lipid droplets in the liver cells and numerous hepatocytes containing medium- or large-size lipid droplets in 6 out of 28 FN-treated patients [33].

Autophagosomes and autolysosomes play a critical role in maintaining normal intracellular homeostasis in response to various stresses, and autophagy, the process associated with the formation of this structures, controls the quality and quantity of cellular organelles and macromolecules [34]. The liver presents high levels of metabolic-stress-induced autophagy that is under the regulation of hormones and amino acids' concentrations. Liver autophagy provides starved cells with amino acids, glucose and free fatty acids for use in energy production and synthesis of new macromolecules. It is also known that liver autophagy contributes to basic hepatic functions, including glycogenolysis, gluconeogenesis and β -oxidation, through selective turnover of specific cargos controlled by a series of transcription factors, e.g. CREB (cAMP response element) or PPAR α [17, 34]. Impaired or deficient autophagy is believed to be associated with aging, and several age-related pathologies [17].

In our study, ultrastructural examination of hepatocytes revealed the presence of autophagosomes and autolysosomes in both age groups. It was showed that in C57BL/6 female mice the number of autophagic structures/vacuoles in hepatocytes decreased with age, and suggested that the age-related decrease in autophagy in the liver may induce accumulation of cellular materials in the liver of aged mice [17]. The study on 26-month-old male Fisher rats showed that there was no effect of age on the fractional volume of autophagic vacuoles [35]. In our study we did not found age-related differences in hepatic expression of LC3A/B (related to autophagosome formation) and beclin 1 proteins (a common regulator of autophagy and apoptosis). Other authors reported that in old compared to young rats, expression of beclin 1, LC3-1 and procathepsin D was decreased, and expression of cathepsin D (a product of procathepsin D proteolytic activation in lysosomes) was increased [35].

Our examination of hepatocytes ultrastructure revealed the presence of autophagosomes and autolysosomes in young and old FN-treated rats. Recent studies showed that hepatic autophagy is activated via PPAR α after short-term treatment with PPAR α agonists both *in vivo* and *in vitro* [36, 37]. There are some data suggesting that treatment with FN may have various effects on autophagy in hepatocytes. In neonate, 5-day-old G6pc^{-/-} mice (autosomal mutation in glucose-6-phosphatase; a model of neonatal glycogen storage disease type Ia) 5-day-long treatment with FN induced autophagy in the liver accompanied

by increased hepatic LC3-II and beclin 1 protein expression, and TEM analyses revealed numerous autophagosomes with electron-dense glycogen granules [14]. In hepatocytes isolated from 8-week-old male C57BL/6J mice treated with FN (0.5–5 μ g/ml for 24 hours), the drug exerted a protective effect against acetaminophen (APAP)-induced hepatotoxicity by enhancing autophagy via elevation of LC3-II and degradation of p62 proteins [23]. In contrast, Zhu *et al.* observed no effect of FN on the process of autophagy in monosodium glutamate (MSG)-induced obese mice that were treated with FN for 5 weeks at dose 45 mg/kg [38].

In summary, the obtained results suggest that fenofibrate may have beneficial effects on the energy metabolism of old rats by increasing the number of mitochondria and peroxisomes in hepatocytes.

Acknowledgments

The authors are grateful to Drs. M. Szaryńska and A. Olejniczak-Kęder for kind supply of anti-LC1/II and anti-beclin1 antibodies.

Funding

The research was financed by the statutory grant (ST-12) of the Medical University of Gdansk, Gdansk, Poland.

Declaration of competing interest

The authors report no declarations of interest.

Authors' contribution

Adrian Zubrzycki: conceptualization, methodology, formal analysis, investigation, resources, writing — original draft, visualization, project administration. **Agata Wronska:** conceptualization, methodology, formal analysis, investigation, resources, writing — original draft, visualization, project administration. **Agata Zauszkiewicz-Pawlak:** methodology, investigation, resources. **Zbigniew Kmiec:** conceptualization, formal analysis, resources, writing — original draft, writing — review & editing, supervision, project administration, funding acquisition.

References

1. Mancini G, Hegele R, Leiter L. Dyslipidemia. *Can J Diabetes*. 2018; 42: S178–S185, doi: [10.1016/j.cjcd.2017.10.019](https://doi.org/10.1016/j.cjcd.2017.10.019), indexed in Pubmed: [29650093](https://pubmed.ncbi.nlm.nih.gov/29650093/).
2. Sahebkar A, Simental-Mendía LE, Watts GF, et al. Lipid and Blood Pressure Meta-analysis Collaboration (LBPMC) Group. Comparison of the effects of fibrates versus statins on

- plasma lipoprotein(a) concentrations: a systematic review and meta-analysis of head-to-head randomized controlled trials. *BMC Med.* 2017; 15(1): 22, doi: [10.1186/s12916-017-0787-7](https://doi.org/10.1186/s12916-017-0787-7), indexed in Pubmed: [28153024](https://pubmed.ncbi.nlm.nih.gov/28153024/).
3. Sairyo M, Kobayashi T, Masuda D, et al. A novel selective PPAR α modulator (SPPARM α), K-877 (Pemafibrate), attenuates postprandial hypertriglyceridemia in mice. *J Atheroscler Thromb.* 2018; 25(10): 1086, doi: [10.5551/jat.ER39693](https://doi.org/10.5551/jat.ER39693), indexed in Pubmed: [30197400](https://pubmed.ncbi.nlm.nih.gov/30197400/).
 4. Bougarne N, Weyers B, Desmet SJ, et al. Molecular actions of PPAR α in lipid metabolism and inflammation. *Endocr Rev.* 2018; 39(5): 760–802, doi: [10.1210/er.2018-00064](https://doi.org/10.1210/er.2018-00064), indexed in Pubmed: [30020428](https://pubmed.ncbi.nlm.nih.gov/30020428/).
 5. Pawlak M, Lefebvre P, Staels B. Molecular mechanism of PPAR α action and its impact on lipid metabolism, inflammation and fibrosis in non-alcoholic fatty liver disease. *J Hepatol.* 2015; 62(3): 720–733, doi: [10.1016/j.jhep.2014.10.039](https://doi.org/10.1016/j.jhep.2014.10.039), indexed in Pubmed: [25450203](https://pubmed.ncbi.nlm.nih.gov/25450203/).
 6. Livertox. LiverTox: Clinical and research information on drug-induced liver injury. Fenofibrate. 2015. Available at: <https://www.ncbi.nlm.nih.gov/books/NBK548607/>. Accessed August.; 5: 2021.
 7. Pettersen JC, Pruijboom-Brees I, Francone OL, et al. The PPAR α agonists fenofibrate and CP-778875 cause increased β -oxidation, leading to oxidative injury in skeletal and cardiac muscle in the rat. *Toxicol Pathol.* 2012; 40(3): 435–447, doi: [10.1177/0192623311431945](https://doi.org/10.1177/0192623311431945), indexed in Pubmed: [22301950](https://pubmed.ncbi.nlm.nih.gov/22301950/).
 8. Zubrzycki A, Wrońska A, Kotulak-Chrzęszcz A, et al. Fenofibrate impairs liver function and structure more pronounced in old than young rats. *Arch Gerontol Geriatr.* 2020 [Epub ahead of print]; 91: 104244, doi: [10.1016/j.archger.2020.104244](https://doi.org/10.1016/j.archger.2020.104244), indexed in Pubmed: [32927318](https://pubmed.ncbi.nlm.nih.gov/32927318/).
 9. Cindoruk M, Kerem M, Karakan T, et al. Peroxisome proliferators-activated alpha agonist treatment ameliorates hepatic damage in rats with obstructive jaundice: an experimental study. *BMC Gastroenterol.* 2007; 7: 44, doi: [10.1186/1471-230X-7-44](https://doi.org/10.1186/1471-230X-7-44), indexed in Pubmed: [18045488](https://pubmed.ncbi.nlm.nih.gov/18045488/).
 10. Colton HM, Falls JG, Ni H, et al. Visualization and quantitation of peroxisomes using fluorescent nanocrystals: treatment of rats and monkeys with fibrates and detection in the liver. *Toxicol Sci.* 2004; 80(1): 183–192, doi: [10.1093/toxsci/kfh144](https://doi.org/10.1093/toxsci/kfh144), indexed in Pubmed: [15084755](https://pubmed.ncbi.nlm.nih.gov/15084755/).
 11. Steinberg P, Schladt L, Dienes HP, et al. Microsomal and cytosolic epoxide hydrolases, the peroxisomal fatty acid beta-oxidation system and catalase. Activities, distribution and induction in rat liver parenchymal and non-parenchymal cells. *Eur J Biochem.* 1988; 176(1): 39–45, doi: [10.1111/j.1432-1033.1988.tb14248.x](https://doi.org/10.1111/j.1432-1033.1988.tb14248.x), indexed in Pubmed: [3416872](https://pubmed.ncbi.nlm.nih.gov/3416872/).
 12. Yang Q, Nagano T, Shah Y, et al. The PPAR alpha-humanized mouse: a model to investigate species differences in liver toxicity mediated by PPAR alpha. *Toxicol Sci.* 2008; 101(1): 132–139, doi: [10.1093/toxsci/kfm206](https://doi.org/10.1093/toxsci/kfm206), indexed in Pubmed: [17690133](https://pubmed.ncbi.nlm.nih.gov/17690133/).
 13. de la Rosa Rodriguez MA, Sugahara Go, Hooiveld GJ, et al. The whole transcriptome effects of the PPAR α agonist fenofibrate on livers of hepatocyte humanized mice. *BMC Genomics.* 2018; 19(1): 443, doi: [10.1186/s12864-018-4834-3](https://doi.org/10.1186/s12864-018-4834-3), indexed in Pubmed: [29879903](https://pubmed.ncbi.nlm.nih.gov/29879903/).
 14. Yavarow ZA, Kang HR, Waskowicz LR, et al. Fenofibrate rapidly decreases hepatic lipid and glycogen storage in neonatal mice with glycogen storage disease type Ia. *Hum Mol Genet.* 2020; 29(2): 286–294, doi: [10.1093/hmg/ddz290](https://doi.org/10.1093/hmg/ddz290), indexed in Pubmed: [31816064](https://pubmed.ncbi.nlm.nih.gov/31816064/).
 15. Halpern KB, Shenhav R, Matcovitch-Natan O, et al. Single-cell spatial reconstruction reveals global division of labour in the mammalian liver. *Nature.* 2017; 542(7641): 352–356, doi: [10.1038/nature21065](https://doi.org/10.1038/nature21065), indexed in Pubmed: [28166538](https://pubmed.ncbi.nlm.nih.gov/28166538/).
 16. Ben-Moshe S, Itzkovitz S. Spatial heterogeneity in the mammalian liver. *Nat Rev Gastroenterol Hepatol.* 2019; 16(7): 395–410, doi: [10.1038/s41575-019-0134-x](https://doi.org/10.1038/s41575-019-0134-x), indexed in Pubmed: [30936469](https://pubmed.ncbi.nlm.nih.gov/30936469/).
 17. Uddin MN, Nishio N, Ito S, et al. Autophagic activity in thymus and liver during aging. *Age (Dordr).* 2012; 34(1): 75–85, doi: [10.1007/s11357-011-9221-9](https://doi.org/10.1007/s11357-011-9221-9), indexed in Pubmed: [21387084](https://pubmed.ncbi.nlm.nih.gov/21387084/).
 18. Brandt T, Mourier A, Tain LS, et al. Changes of mitochondrial ultrastructure and function during ageing in mice and Drosophila. *Elife.* 2017; 6, doi: [10.7554/eLife.24662](https://doi.org/10.7554/eLife.24662), indexed in Pubmed: [28699890](https://pubmed.ncbi.nlm.nih.gov/28699890/).
 19. Shigenaga MK, Hagen TM, Ames BN. Oxidative damage and mitochondrial decay in aging. *Proc Natl Acad Sci U S A.* 1994; 91(23): 10771–10778, doi: [10.1073/pnas.91.23.10771](https://doi.org/10.1073/pnas.91.23.10771), indexed in Pubmed: [7971961](https://pubmed.ncbi.nlm.nih.gov/7971961/).
 20. de la Cruz J, Burón I, Roncero I. Morphological and functional studies during aging at mitochondrial level. Action of drugs. *Int J Biochem.* 1990; 22(7): 729–735, doi: [10.1016/0020-711x\(90\)90008-q](https://doi.org/10.1016/0020-711x(90)90008-q), indexed in Pubmed: [2401374](https://pubmed.ncbi.nlm.nih.gov/2401374/).
 21. Łysek-Gładysińska M, Wieczorek A, Józwick A, et al. Aging-related changes in the ultrastructure of hepatocytes and cardiomyocytes of elderly mice are enhanced in ApoE-deficient animals. *Cells.* 2021; 10(3), doi: [10.3390/cells10030502](https://doi.org/10.3390/cells10030502), indexed in Pubmed: [33652838](https://pubmed.ncbi.nlm.nih.gov/33652838/).
 22. Schmucker DL. Aging and the liver: An Update. *J Gerontol A Biol Sci Med Sci.* 1998; 53A(5): B315–B321, doi: [10.1093/gerona/53a.5.b315](https://doi.org/10.1093/gerona/53a.5.b315).
 23. Nagata T. Electron microscopic radioautographic study on protein synthesis in hepatocyte mitochondria of aging mice. *Scientific World Journal.* 2006; 6: 1583–1598, doi: [10.1100/tsw.2006.265](https://doi.org/10.1100/tsw.2006.265), indexed in Pubmed: [17173177](https://pubmed.ncbi.nlm.nih.gov/17173177/).
 24. Le Couteur DG, Warren A, Cogger VC, et al. Old age and the hepatic sinusoid. *Anat Rec (Hoboken).* 2008; 291(6): 672–683, doi: [10.1002/ar.20661](https://doi.org/10.1002/ar.20661), indexed in Pubmed: [18484614](https://pubmed.ncbi.nlm.nih.gov/18484614/).
 25. He A, Dean JM, Lodhi IJ. Peroxisomes as cellular adaptors to metabolic and environmental stress. *Trends Cell Biol.* 2021; 31(8): 656–670, doi: [10.1016/j.tcb.2021.02.005](https://doi.org/10.1016/j.tcb.2021.02.005), indexed in Pubmed: [33674166](https://pubmed.ncbi.nlm.nih.gov/33674166/).
 26. van Zutphen T, Ciapaite J, Bloks VW, et al. Malnutrition-associated liver steatosis and ATP depletion is caused by peroxisomal and mitochondrial dysfunction. *J Hepatol.* 2016; 65(6): 1198–1208, doi: [10.1016/j.jhep.2016.05.046](https://doi.org/10.1016/j.jhep.2016.05.046), indexed in Pubmed: [27312946](https://pubmed.ncbi.nlm.nih.gov/27312946/).
 27. Mitchell AM, Lhuguenot JC, Bridges JW, et al. Identification of the proximate peroxisome proliferator(s) derived from di(2-ethylhexyl) phthalate. *Toxicol Appl Pharmacol.* 1985; 80(1): 23–32, doi: [10.1016/0041-008x\(85\)90097-3](https://doi.org/10.1016/0041-008x(85)90097-3), indexed in Pubmed: [4024105](https://pubmed.ncbi.nlm.nih.gov/4024105/).
 28. Yamoto T, Ohashi Y, Teranishi M, et al. Age-related changes in the susceptibility to clofibrate, a hypolipidemic agent, of male rat liver. *Toxicol Lett.* 1995; 78(2): 141–145, doi: [10.1016/0378-4274\(94\)03247-5](https://doi.org/10.1016/0378-4274(94)03247-5), indexed in Pubmed: [7618179](https://pubmed.ncbi.nlm.nih.gov/7618179/).
 29. Blanc EF, Pinaroli F. Fenofibrate: animal toxicology in relation to side-effects in man (author's transl). *Nouv Presse Med* 1980; 9: 3737-3746. , indexed in Pubmed: [7208340](https://pubmed.ncbi.nlm.nih.gov/7208340/).
 30. Johnson AA, Stolzing A. The role of lipid metabolism in aging, lifespan regulation, and age-related disease. *Aging Cell.* 2019; 18(6): e13048, doi: [10.1111/accel.13048](https://doi.org/10.1111/accel.13048), indexed in Pubmed: [31560163](https://pubmed.ncbi.nlm.nih.gov/31560163/).
 31. Wan J, Wu X, Chen H, et al. Aging-induced aberrant RAGE/PPAR α axis promotes hepatic steatosis via dysfunctional mitochondrial β oxidation. *Aging Cell.* 2020; 19(10): e13238, doi: [10.1111/accel.13238](https://doi.org/10.1111/accel.13238), indexed in Pubmed: [32936538](https://pubmed.ncbi.nlm.nih.gov/32936538/).

32. Schmucker DL, Mooney JS, Jones AL. Stereological analysis of hepatic fine structure in the Fischer 344 rat. Influence of sublobular location and animal age. *J Cell Biol.* 1978; 78(2): 319–337, doi: [10.1083/jcb.78.2.319](https://doi.org/10.1083/jcb.78.2.319), indexed in Pubmed: [690169](https://pubmed.ncbi.nlm.nih.gov/690169/).
33. Blümcke S, Schwartzkopff W, Lobeck H, et al. Influence of fenofibrate on cellular and subcellular liver structure in hyperlipidemic patients. *Atherosclerosis.* 1983; 46(1): 105–116, doi: [10.1016/0021-9150\(83\)90169-7](https://doi.org/10.1016/0021-9150(83)90169-7), indexed in Pubmed: [6838687](https://pubmed.ncbi.nlm.nih.gov/6838687/).
34. Ueno T, Komatsu M. Autophagy in the liver: functions in health and disease. *Nat Rev Gastroenterol Hepatol.* 2017; 14(3): 170–184, doi: [10.1038/nrgastro.2016.185](https://doi.org/10.1038/nrgastro.2016.185), indexed in Pubmed: [28053338](https://pubmed.ncbi.nlm.nih.gov/28053338/).
35. Wohlgemuth SE, Julian D, Akin DE, et al. Autophagy in the heart and liver during normal aging and calorie restriction. *Rejuvenation Res.* 2007; 10(3): 281–292, doi: [10.1089/rej.2006.0535](https://doi.org/10.1089/rej.2006.0535), indexed in Pubmed: [17665967](https://pubmed.ncbi.nlm.nih.gov/17665967/).
36. Jo E, Li S, Liang Q, et al. Chronic activation of PPAR α with fenofibrate reduces autophagic proteins in the liver of mice independent of FGF21. *PLoS One.* 2017; 12(4): e0173676, doi: [10.1371/journal.pone.0173676](https://doi.org/10.1371/journal.pone.0173676), indexed in Pubmed: [28422956](https://pubmed.ncbi.nlm.nih.gov/28422956/).
37. Park JSu, Kang DH, Lee DaH, et al. Fenofibrate activates Nrf2 through p62-dependent Keap1 degradation. *Biochem Biophys Res Commun.* 2015; 465(3): 542–547, doi: [10.1016/j.bbrc.2015.08.056](https://doi.org/10.1016/j.bbrc.2015.08.056), indexed in Pubmed: [26282199](https://pubmed.ncbi.nlm.nih.gov/26282199/).
38. Zhu S, Wu Y, Ye X, et al. FGF21 ameliorates nonalcoholic fatty liver disease by inducing autophagy. *Mol Cell Biochem.* 2016; 420(1-2): 107–119, doi: [10.1007/s11010-016-2774-2](https://doi.org/10.1007/s11010-016-2774-2), indexed in Pubmed: [27435856](https://pubmed.ncbi.nlm.nih.gov/27435856/).

Submitted: 5 August, 2021

Accepted after reviews: 24 August, 2021

Available as AoP: 13 September, 2021

Growth factors in the initial stage of bone formation, analysis of their expression in chondrocytes from epiphyseal cartilage of rat costochondral junction

Anna Hyc, Stanislaw Moskalewski, Anna Osiecka-Iwan

Department of Histology and Embryology, Medical University of Warsaw, Warsaw, Poland

Abstract

Introduction. In endochondral ossification septoclasts and osteoclasts (also called chondroclasts) release growth factors deposited in non-calcified and calcified zones of the growth plate. They stimulate, within the metaphysis, initial stages of the bone formation. We have recently reported quantitation of several growth factors in calcified cartilage from calf costochondral junction. Data from the analogous human cartilage could possibly help to choose efficient combinations of growth factors for clinical applications, but the amount of the calcified cartilage needed for analysis of numerous growth factors would be difficult to collect. The estimation of growth factors expression in endochondral chondrocytes may, indirectly, indicate which of them play a leading role in the stimulation of osteoprogenitor cells in metaphysis. To test this hypothesis, we used rat chondrocytes to evaluate mRNA levels of several growth factors.

Materials and methods. Chondrocytes were isolated from proliferative and hypertrophic zones of the epiphyseal cartilage forming costochondral junctions of inbred Lewis rats. The total RNA was isolated from chondrocytes and the level of mRNA for bone morphogenetic proteins 1-7 (BMP-1-7), vascular endothelial growth factor A (VEGF-A), basic fibroblast growth factor (bFGF), growth/differentiation factor 5 (GDF-5), NELL-like protein 1 (NELL-1), transforming growth factor beta 1 (TGF- β 1), mesencephalic astrocyte-derived neurotrophic factor (MANF), connective tissue growth factor (CTGF), osteoclast-stimulating factor 1 (OSTF-1) and insulin-like growth factor 1 (IGF-1) was evaluated using real-time PCR method.

Results. All studied factors were expressed. The highest level of mRNA was detected for CTGF, MANF, VEGF-A and TGF- β 1. Expression was also quite high for BMP-1, BMP-2, BMP-5, BMP-6, BMP-7, IGF-1, GDF-5 and OSTF-1. Very low level of mRNA was detected for BMP-3, BMP-4 and NELL-1.

Conclusions. Chondrocytes from the proliferative and hypertrophic zones of the growth plate produce factors involved in the cartilage metabolism and bone formation. The determination of these growth factors in humans could help to choose their optimal composition necessary for stimulation of bone formation in clinical practice. In rat the best stimulation of bone formation would presumably be achieved with a mixture of BMP-2, BMP-5, BMP-6 and BMP-7. (*Folia Histochemica et Cytobiologica* 2021, Vol. 59, No. 3, 178–186)

Key words: rat; epiphyseal cartilage; costochondral junction; bone formation; growth factors; qPCR

Introduction

Epiphyseal growth plate composed of hyaline cartilage constitutes the dynamic structure with stem cells

present in the reserve zone which differentiate and rapidly divide in the proliferative zone, enlarge in the hypertrophic zone, and finally undergo apoptosis in the provisional calcification zone close to the metaphysis [1-8]. Calcification of the growth cartilage begins in the extracellular matrix (ECM) forming longitudinal septa and separating rows of chondrocytes. In the hypertrophic zone septa, roundish bodies appear that are produced by chondrocytes and called matrix vesicles. They serve as initiation sites of mineral dep-

Correspondence address: Anna Osiecka-Iwan Ph.D.
Department of Histology and Embryology,
Medical University of Warsaw,
Chalubinskiego 5, PL-02004 Warsaw, Poland
phone/fax: +48 22 629 52 82, e-mail: aiwan@wum.edu.pl

osition in the cartilage [9-11]. Calcified matrix vesicles join into larger structures, called globular units and finally into massive calcium phosphate deposits occupying most of the calcification zone territory [12].

The proliferation and differentiation of chondrocytes in the epiphyseal cartilage are regulated by numerous factors belonging to the TGF- β superfamily. In the immunocytochemical studies bone morphogenetic proteins 1-7 (BMPs 1-7) were demonstrated in proliferative, maturing and late hypertrophic chondrocytes of rat tibial growth plate [13]. BMPs 1-7 and vascular endothelial growth factor (VEGF) were also found in matrix vesicles isolated from rat growth plate, which could carry them from chondrocytes into the matrix [14]. BMP signalling is required for maintenance of the differentiated phenotype, control of cell proliferation, expression of hypertrophic phenotype of chondrocytes [15, 16] and skeletal development [17]. BMP-2 and BMP-6 are upregulated in hypertrophic zone compared with resting zone and proliferative zone from rat growth plate while signalling inhibitor BMP-3 is highly expressed in resting zone [18]. In turn, BMP-5 upregulated expression of hypertrophic zone markers - parathyroid receptor 1 and collagen type X alpha 1 in cell line ATDC5 serving as the growth plate model [19].

Vascular invasion into growth plate depends on the production of VEGF by hypertrophic chondrocytes [20] with invading endothelial cells as a target [21]. Moreover, VEGF acts also as a survival factor for growth plate chondrocytes [21], is instrumental for invasion of osteoclasts into the hypertrophic cartilage [22, 23], and serves as the mediator connecting angiogenesis with osteogenesis [24].

Gradients of BMPs across the growth plate form many local signaling pathways and may be a key mechanism responsible for spatial regulation of chondrocyte proliferation and differentiation. Due to cross-talks and feedback mechanisms, these interwoven pathways display a network-like structure. This network is able to capture the different states (resting, proliferating and hypertrophic) that chondrocytes go through as they progress within the growth plate and finally support vascular invasion [1, 8, 25, 26].

Both in our previous work [27] and in the present contribution, an advantage was taken of the similarity in the structure and function of epiphyseal growth plate and costochondral junctions [28-30]. It was possible to obtain sufficient amount of calcified cartilage from the zone of provisional calcification in costochondral junctions of calf ribs for quantitative determination by ELISA of deposited growth factors. It had high content of growth/differentiation factor 5 (GDF-5), BMP-7, and NEL-like protein 1 (NELL-1) [27] suggesting that these factors play a leading role in

the stimulation of bone formation within calf epiphyseal cartilage. Other factors, such as BMP-2, BMP-3, BMP-4; basic fibroblast growth factor (bFGF), VEGF and transforming growth factor beta 1 (TGF- β 1) occurred in lower quantities. Still others, BMP-1, BMP-5, BMP-6, insulin-like growth factor 1 (IGF-1), osteoclast-stimulating factor 1 (OSTF-1), mesencephalic astrocyte-derived neurotrophic factor (MANF) and connective tissue growth factor (CTGF) were not detected. Thus, it appears that epiphyseal chondrocytes not only produce growth factors as the regulators of their own growth and differentiation but also prepare considerable store of chosen factors for the initial period of bone deposition.

The initial enthusiasm for the use of bone morphogenetic factors in the clinical practice [31, 32] subsided due to the observations of unfavourable side effects such as postoperative inflammation, ectopic bone formation, osteoclast-mediated severe bone resorption and life-threatening cervical spine swelling [33, 34] as well as by apprehension of neoplastic growth stimulation [35]. There are also problems with the choice of proper carrier vehicle for BMPs. Sodium acetate buffer, bovine type I collagen matrix in combination with carboxymethyl-cellulose, absorbable collagen sponge, polymers or ceramic composites were tested.

Alternative BMP delivery systems include also viral vectors or genetically altered cells [36]. An absorbable collagen sponge as a carrier for BMP-2 has been approved by U.S. Food and Drug Administration (FDA) for the use in humans, but the optimal carrier vehicle for BMP-2 or other growth factors delivery has yet not been established [33]. Recently, gene delivery is a new option for achieving the sustained release of BMP-2 and stimulation of bone defects healing. It involves transferring a target gene encoding BMP-2 into the defect site using vectors carrying the gene. Then, the cells transfected by vectors carrying the gene produce the target molecules *in vivo* and secrete the target molecules into the defect site. The drug release period can be controlled by the vector carrying the gene [37, 38].

Another approach for the improvement of BMPs administration results involved construction of injectable bmp-2 delivery system based on collagen derived microspheres and alginate. This system, when tested in rats, considerably reduced BMP-2 dose needed for successful induction of ectopic bone formation in rats [39]. As a delivery system for BMP-2 a non-polymer hydrogel, based on the self-assembly of small amphiphilic glycosyl-nucleolipids into micellar structures was also tried. When tested in mice it stimulated ectopic bone formation at low doses of BMP-2 [40].

The formation of bone within growth plate is dependent on several growth factors which presumably

act synergistically and thus may be effective at low concentrations to allow harmonious osteogenesis. We have recently shown that in the bovine epiphyseal cartilage BMP-7, NELL-1 and GDF-5 may play a key role in early mineralization [27]. The question arises which other growth factors and at what concentration are deposited in calcified cartilage from human growth plate. In view of the similarity between the mechanisms of endochondral bone formation during development and healing of mature bone fractures [41] it is plausible that recognition of growth factors deposited in human calcified cartilage could help to choose optimal composition of growth factors for the stimulation of bone formation in clinical practice. Unfortunately, the amount of calcified human cartilage from growth plates needed for analysis of numerous growth factors would be difficult to collect. Analysis of growth factors expression at the mRNA level requires, however, a much lower number of chondrocytes than analysis of their presence as proteins in calcified cartilage. Human chondrocytes, for example, from the costochondral junctions of young transplant donors, could be accessible with maintaining ethical standards according to the Academy of Medical Royal Colleges, 2015; Recommendation 9: "When parents would like to donate their child's organs for transplantation, but this is not clinically possible, clinicians should attempt wherever possible to accept such organs for research, if this is an acceptable alternative to the parents" [42].

The aim of our study was to check whether the expression of genes encoding growth factors by growth plate chondrocytes may be related to the amount of the respective proteins in calcified cartilage. For the verification of this supposition, we evaluated the expression of growth factors at the mRNA level in growth plate chondrocytes in an animal model and tried to deduce which of them are essential for the stimulation of osteoprogenitor cells and, presumably, are deposited in calcified cartilage. Because in the previous work [27] we used calf cartilage, the best way to test this hypothesis would be to use calf chondrocytes, unfortunately they could be collected at the earliest 24 h after death of the animal. Therefore, we used rat chondrocytes from the proliferative and hypertrophic zone of epiphyseal cartilage of costochondral junction, to evaluate mRNA level of selected growth factors: BMPs 1-7, VEGF-A, bFGF, GDF-5, NELL-1, TGF- β 1, MANF, CTGF, OSTF-1 and IGF-1.

Materials and methods

Animals. Donors of chondrocytes were 6-week-old inbred Lewis male rats. Cartilages were taken from two rats for one experiment (number of experiments was 5, $n = 5$). The

study was approved by the Animal Ethics Committee of the Medical University of Warsaw, Poland (no 049/2016).

Preparation of cartilage. Ribs were dissected from costochondral junctions and cleared from the adhering tissues. The metaphysis was identified under dissecting microscope, separated from cartilage and about 1 mm in length of cartilage containing hypertrophic and proliferative zones was taken either for chondrocyte isolation or histological observations.

Isolation of chondrocytes. Cartilages taken from two rats for one experiment were left in 0.125% collagenase and 0.025% DNase solution dissolved in RPMI 1640 medium (Merck KGaA, Darmstadt, Germany) at 37°C for 18 hours. During the last hour of exposition, the suspension of partially digested cartilage fragments was stirred on the magnetic stirrer to facilitate dispersion into single cells. Non-digested (calcified) fragments were separated with 20 μ m mesh filter (Merck). Isolated chondrocytes were counted in the Bürger's chamber. About 2×10^6 chondrocytes was obtained from two rats. Chondrocytes were used for isolation of total RNA.

Total RNA isolation. RNA was isolated with NucleoSpin®-RNA II kit (Macherey-Nagel, Duren, Germany), according to manufacturer's protocol. The quantity and quality of the isolated total RNA was evaluated spectrophotometrically using ND-2000-Spectrophotometer NanoDrop 2000 with software for analysis of nucleic acids (Thermo Fisher Scientific, Wilmington, DE, USA).

Reverse transcription. Reverse transcription was performed using the High Capacity cDNA Reverse Transcription kit (Applied Biosystems, Warrington, UK), according to the manufacturer's protocol in Eppendorf Mastercycler gradient (10 min at 25°C, 120 min at 37°C and 5 sec. at 85°C). Briefly, 2 μ l of 10 \times RT buffer, 0.8 μ l of 25 \times dNTP Mix, 2 μ l of 10 \times Random Primers, 1 μ l of Multiscribe Reverse Transcriptase, 4.2 μ l of nuclease-free water and 10 μ l of mRNA (0.5 μ g) per one reaction. cDNA samples were stored at -20°C.

Real-time PCR. Real-time PCR was performed in the ABI-IPRISM 7500 (Applied Biosystems) using 96-well optical plates. Each sample was run in triplicate and was supplied with an endogenous control (Rat GAPDH endogenous control Rn01775763_g1). For gene expression analysis, proper TaqMan expression assays was used: Rn00686607_m1 for OSTF-1, Rn00563954_m1 for type II collagen, Rn01466014_m1 for BMP-1, Rn00567818_m1 for BMP-2, Rn00567346_m1 for BMP-3, Rn00432087_m1 for BMP-4, Rn01447676_m1 for BMP-5, Rn00432095_m1 for BMP-6, Rn01528889_m1 for BMP-7, Rn01511602_m1 for VEGF A, Rn00572010_m1 for TGF- β 1, Rn01445633_m1 for MANF, Rn00710306_m1 for IGF1, Rn00433564_m1 for GDF-5, Rn01537279_g1 for CTGF, Rn00570809_m1 for bFGF, and

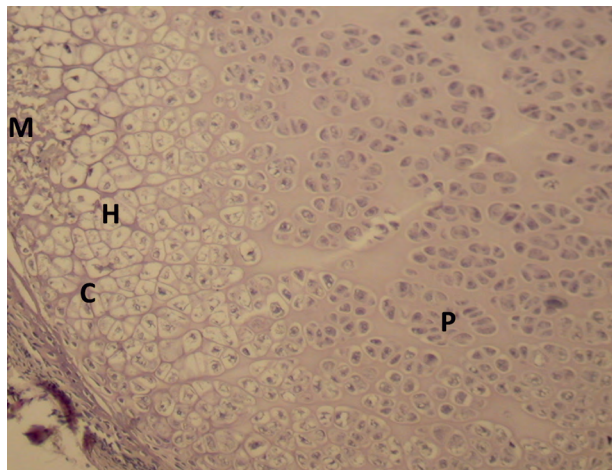


Figure 1. Fragment of rat rib costochondral junction. P — zone of proliferative chondrocytes; H — zone of hypertrophic chondrocytes; C — zone of provisional calcification; M — metaphysis; PC — perichondrium. In the section, chondrocytes from the proliferative zone are predominant; hypertrophic chondrocytes are considerably shrunken due to fixation and embedding. H&E staining. Total magnification 100 \times .

Rn00675924_m1 for NELL-1. All probes were stained with FAM (Applied Biosystems). Reactions were run in 25 μ l with TaqMan Universal Master Mix, appropriate primer set, MGB probe and 50 ng of cDNA template. Universal thermal conditions, 10 min at 95 $^{\circ}$ C, 40 cycles of 15 sec at 95 $^{\circ}$ C and 1 min at 60 $^{\circ}$ C, were used. Data analysis was done with sequence detection software version 1.2 (Applied Biosystems). Relative expression was calculated against the reference gene, GAPDH. This reference gene is acceptable in studies on gene expression in normal chondrocytes and bone cells [43–45]. Analysis was conducted as a Δ CT values using sequence detection software ver. 1.2 (Applied Biosystems).

Histology. Ribs were fixed in 10% buffered formalin, dehydrated, embedded in paraffin, sectioned at 6 μ m thick slices and stained with haematoxylin and eosin.

Results

Morphology of the epiphyseal cartilage sections

Fragment of rat rib costochondral junction is shown at Figure 1. It is a tissue section from the fragment of cartilage used for enzymatic digestion and further isolation of cells. Section demonstrates zone of proliferative chondrocytes (P), zone of hypertrophic chondrocytes (H), zone of provisional calcification (C), metaphysis (M) and perichondrium (PC). Predominate chondrocytes are present in the proliferative zone, hypertrophic chondrocytes are considerably shrunken due to fixation and embedding. Fragments of cartilage dissected for chondrocyte isolation con-

tained mainly cells from the proliferative zone since the zone of hypertrophic chondrocytes was narrow and cells from provisional calcification were not isolated because calcium deposits prevented access of collagenase.

The expression of the studied growth factors at the mRNA level

The relative expression of the genes encoding the studied growth factors in chondrocytes from the digested epiphyseal cartilage was calculated against the reference gene, GAPDH, and presented as the Δ CT values at Figure 2. The obtained results indicate that mRNA for all studied factors were expressed but the level of the expression considerably differed. The highest levels of mRNA were detected for CTGF, MANF, VEGF-A and TGF- β 1. The expression was also quite high for BMP-1, BMP-2, BMP-5, BMP-6, BMP-7, IGF-1, GDF-5, and OSTF-1. Very low level of mRNA was detected for BMP-3, BMP-4, and NELL-1 (Fig. 2).

Discussion

As we have reported previously [27], growth factors present in calcified and small amount of adhering non-calcified matrix of calf rib costochondral junction could form a depot released by septoclasts and osteoclasts and are involved in early stages of bone formation. From the 16 growth factors studied in calf epiphyseal cartilage only nine (BMP-2, BMP-3, BMP-4, BMP-7, GDF-5, NELL-1, TGF- β 1, bFGF and VEGF) were identified by ELISA [27], however, all of them were expressed at the mRNA level by rat epiphyseal chondrocytes. The highest expression showed CTGF, cytokine which participates in the matrix turnover by binding to ECM proteins [46, 47] and MANF. The role of MANF in skeletal tissue homeostasis is currently unknown but in transgenic *Manf* null mice the growth of long bones was reduced [48]. Both factors do not appear to have prominent function in the stimulation of bone growth, thus their absence in calf calcified matrix is not surprising [27]. OSTF1 was identified as a factor involved in the indirect activation of osteoclasts [49] but its role, if any, in early stages of osteogenesis remains unknown.

BMP-1, BMP-5, BMP-6 and IGF-1, also not detected by ELISA in bovine calcified cartilage [27], are known to take part in various stages of bone formation. BMP-1 participates in the formation of mammalian extracellular matrix (ECM), and in the formation of bone through activation of TGF- β [50, 51]. BMP-5 is expressed in chondrocytes of proliferating zone and its expression increased sharply with hypertrophic differentiation in tibial growth plates

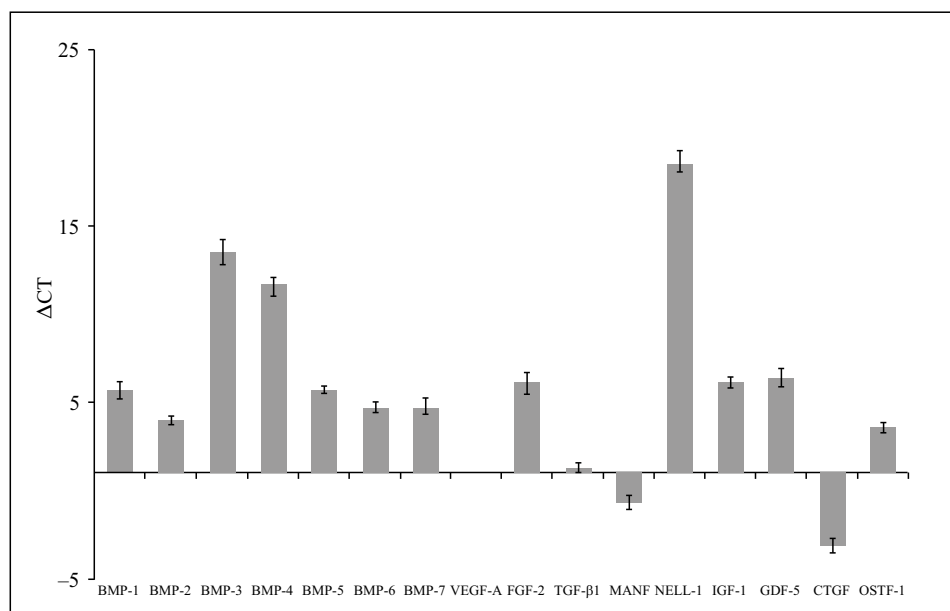


Figure 2. Average Δ CT values (\pm SE) as determined by real-time PCR by subtracting the average GAPDH CT value from the average growth CT values ($n = 5$) calculated using sequence detection software ver. 1.2 (Applied Biosystems).

from normal rats [52]. BMP-6 is highly expressed during proliferation and differentiation of chondrocytes from shanks of 15-day-old chicken embryos. When its expression decreases, the proliferation and differentiation of chondrocytes are blocked [53]. BMP-5 and BMP-6 induce the formation of cartilage and bone in the rat subcutaneous transplant model, but the former requires higher doses for similar osteoinduction [31]. IGF-1 regulates bone length of the skeleton acting on chondrocytes of the proliferative and hypertrophic zones of the growth plate [8, 54, 55].

From growth factors found in bovine epiphyseal calcified cartilage [27] and expressed, as shown in this study at the mRNA level in rat chondrocytes, BMP-2 not only stimulates bone formation [56] but significantly enhances osteoclastogenesis [57]. Moreover, BMP-2 also regulates chondrogenic and osteogenic differentiation of mesenchymal stem cells *in vitro* and *in vivo* [58]. BMP-3 is an inhibitor of osteogenesis *in vitro* and of bone formation *in vivo* and may antagonize BMP-2 signalling [59, 60]. BMP-4 acts synergistically with VEGF to increase recruitment of mesenchymal stem cells and to augment cartilage formation in the early stages of endochondral bone formation [61]. BMP-4 promotes cartilage growth, matrix deposition and chondrocyte proliferation as well as alkaline phosphatase and collagen type X expression in hypertrophic chondrocytes [62] but was less efficient than BMP-2 in promoting bone formation in a calvarial defect model [63]. Both BMP-2 and BMP-7 (also known as osteogenic protein-1) seem to induce bone formation at the same level in rat subcutaneous transplant model [56].

GDF-5 (BMP 14) is predominantly found at the stage of precartilaginous mesenchymal condensation and throughout the cartilaginous cores of the developing calf long bones [64]. In transgenic mice model it is responsible for mesenchymal cell recruitment and chondrocyte differentiation [65] as well as for proper skeletal patterning and joint development in the vertebrate limb [66, 67].

NELL-1 is not a member of TGF- β superfamily, but it is highly specific to the osteochondral lineage and can promote orthotopic bone regeneration [68–70]. The chondrocyte-specific NELL-1 inactivation in knockout mice significantly impedes appendicular skeletogenesis [71]. The low level of NELL-1 gene expression in rat epiphyseal chondrocytes contrasts with data from bovine calcified cartilage [27] in which considerable amount of NELL-1 protein is deposited. TGF- β 1, highly expressed in rat chondrocytes, is involved in formation, maturation, and mineralization of cartilage as well as skeletal development [72, 73].

FGF-2 was detected immunohistochemically in the cytoplasm of proliferating chondrocytes and upper hypertrophic chondrocytes in human vertebrae [7] and mouse tibial growth plate [74]. It stimulated endosteal and endochondral bone formation and depressed periosteal bone formation in growing rats [75].

VEGF is expressed by hypertrophic chondrocytes [21, 76, 77]. Members of the VEGF family are essential coordinators of chondrocyte death, chondrocyte function, extracellular matrix remodelling, angiogenesis and endochondral ossification cooperating with other growth factors in differentiation

of osteoblasts and osteoclasts [3, 78, 79]. The high expression of VEGF by rat epiphyseal chondrocytes well corresponds with the data presented by above quoted authors.

It is evident from the data presented above that formation, maturation and differentiation of endochondral cartilage is under control of numerous growth factors. Moreover, some growth factors necessary for stimulation of endochondral ossification are stored in calcified and also in attached to it non-calcified cartilage. They are transported in matrix vesicles together with alkaline phosphatase and substrates for calcium phosphate deposition into cartilage matrix [11, 14]. Thus, the assumption that the amount of growth factors deposited in calcified cartilage is related to their expression in chondrocytes from proliferative and hypertrophic zones seems justified.

Comparison of growth factors expression by rat and human growth plate chondrocytes is difficult due to the scarcity of data of the latter. Anderson *et al.* [13] in the histochemical study found that proliferating chondrocytes from human growth plate express BMP-1, BMP-2, BMP-5, BMP-6 at moderate (marked ++) and BMP-3, BMP-7 at the minimal level (marked + or ±). In hypertrophic chondrocytes all studied BMPs were expressed at the moderate or maximal (+++) level. Thus, evaluation of the histochemical data from growth plate cartilage does not allow predicting which of the BMPs dominate in the initial stages of bone formation in metaphysis. Expression of GDF-5 and NELL-1 in human growth plate, as far as we could establish, was never studied.

Comparison of the results of Iwan *et al.* [27] and those in this work indicates a distinct species difference between calf and rat. In calf epiphyseal cartilage depot of bone growth factors consisted mainly of NELL-1, BMP-7 and GDF-5. Taking into consideration osteogenic activity of some growth factors and based on rat growth factors mRNA level, we can suppose that in the rat depot of these growth factors, presumably predominate BMP-2 with participation of BMP-6, BMP-7 and possible TGF-β1.

We have also compared results of our Real-time PCR study with results of immunochemical observations of other authors. Nillson *et al.* [18] microdissected chondrocytes from resting zone, proliferative zone, proliferative-hypertrophic transition zone, and hypertrophic zone of proximal tibial epiphyses of 7-day-old rats and used them to isolate RNA. Expression of BMP-2, BMP-3, BMP-4, BMP-6 and BMP-7 was studied; mRNAs of BMP-2; BMP-6 and BMP-7 predominated in all zones. The high level of BMP-2; BMP-6 and BMP-7 mRNAs was also evident in our work [27], in which chondrocytes from 6-week-old rats

were used. Thus, the sophisticated microdissection study and our tissue culture experiments gave similar results suggesting that the expression of BMPs in chondrocytes is not age-dependent, at least within 7-day – 6-week period. Mailhot *et al.* [52] studied expression of BMP-5 in tibial growth plates from 2- and 4-week-old rats by immunohistochemistry and found that its expression is upregulated in hypertrophic zone chondrocytes when compared with those in the proliferating zone. The expression of BMP-5 was also observed in our study at the mRNA level.

Horner *et al.* [20] immunolocalised VEGF in human neonatal growth plates. Immunoreactivity was absent in chondrocytes from the resting zone and only weakly expressed by occasional chondrocytes in the proliferating region. In the hypertrophic zone the number of chondrocytes stained and the intensity of staining for VEGF increased with chondrocytes' hypertrophy, maximum expression of VEGF being observed in chondrocytes in the lower hypertrophic and mineralised regions of the cartilage. The authors concluded that VEGF produced by hypertrophic chondrocytes may play a key role in the regulation of vascular invasion of the growth plate. Marked expression of VEGF was also observed in the rat growth plate chondrocytes in our study.

In another paper Horner *et al.* [80] detected by immunolocalisation TGF-β1 in human epiphyseal cartilage. Its expression was restricted to the proliferative and upper hypertrophic zones, *i.e.*, approximately in the same areas in which we detected TGF-β1 in rat cartilage. Wezeman and Bollnow [74] in mouse tibial growth plate detected by immunostaining bFGF in the extracellular matrix immediately adjacent to the chondrocytes of the proliferating and upper hypertrophic zones. We have detected expression of bFGF in chondrocytes from the same zones of rat growth plates. Evidently, mouse chondrocytes secreted most of the product and the amount left in cells was too low for immunodetection.

Our study describes expression of growth factors in chondrocytes from rat growth plate at the mRNA level. The number of chondrocytes used in the present study is insufficient for determination of the quantity of growth factors produced by the expressed genes. The results of the study encourage, however, their continuation with mass isolation of chondrocytes from large number of rats followed by ELISA tests.

We hope that the similar studies with human material (for example using costochondral junctions of young organ donors) will allow to determine which growth factors predominate in endochondral ossification in humans so that the composition of these factors will be useful in the treatment of bone disorders.

Acknowledgements

Not applicable.

Funding

This research was supported by the National Science Centre, Poland (grant no. 2016/21/B/NZ1/00289).

Availability of data and materials

The datasets used and/or analysed during the present study are available from the corresponding author on reasonable request.

Authors' contributions

SM designed the study. AH and AI performed the experiments. AH, SM and AI analysed the data. AH, SM and AI wrote the manuscript. All authors have read and approved the final manuscript. AI, SM and AH confirmed the authenticity of all the raw data.

Ethics approval and consent to participate

The study was approved by the Animal Ethical Committee of the Medical University of Warsaw.

Conflict of interests

All authors declare no conflicts of interest in this work.

References

- Adams SL, Cohen AJ, Lassová L. Integration of signaling pathways regulating chondrocyte differentiation during endochondral bone formation. *J Cell Physiol.* 2007; 213(3): 635–641, doi: [10.1002/jcp.21262](https://doi.org/10.1002/jcp.21262), indexed in Pubmed: 17886256.
- Amizuka N, Hasegawa T, Oda K, et al. Histology of epiphyseal cartilage calcification and endochondral ossification. *Front Biosci (Elite Ed).* 2012; 4: 2085–2100, doi: [10.2741/526](https://doi.org/10.2741/526), indexed in Pubmed: 22202021.
- Patil AS, Sable RB, Kothari RM. Occurrence, biochemical profile of vascular endothelial growth factor (VEGF) isoforms and their functions in endochondral ossification. *J Cell Physiol.* 2012; 227(4): 1298–1308, doi: [10.1002/jcp.22846](https://doi.org/10.1002/jcp.22846), indexed in Pubmed: 21604271.
- Burdan F, Szumiło J, Korobowicz A, et al. Morphology and physiology of the epiphyseal growth plate. *Folia Histochem Cytobiol.* 2009; 47(1): 5–16, doi: [10.2478/v10042-009-0007-1](https://doi.org/10.2478/v10042-009-0007-1), indexed in Pubmed: 19419931.
- Brochhausen C, Lehmann M, Halstenberg S, et al. Signaling molecules and growth factors for tissue engineering of cartilage-what can we learn from the growth plate? *J Tissue Eng Regen Med.* 2009; 3(6): 416–429, doi: [10.1002/term.192](https://doi.org/10.1002/term.192), indexed in Pubmed: 19575393.
- Mackie EJ, Tatarczuch L, Mirams M. The skeleton: a multi-functional complex organ: the growth plate chondrocyte and endochondral ossification. *J Endocrinol.* 2011; 211(2): 109–121, doi: [10.1530/JOE-11-0048](https://doi.org/10.1530/JOE-11-0048), indexed in Pubmed: 21642379.
- Marino R. Growth plate biology: new insights. *Curr Opin Endocrinol Diabetes Obes.* 2011; 18(1): 9–13, doi: [10.1097/MED.0b013e3283423df9](https://doi.org/10.1097/MED.0b013e3283423df9), indexed in Pubmed: 21157322.
- Lui JC, Nilsson O, Baron J. Recent research on the growth plate: Recent insights into the regulation of the growth plate. *J Mol Endocrinol.* 2014; 53(1): T1–T9, doi: [10.1530/JME-14-0022](https://doi.org/10.1530/JME-14-0022), indexed in Pubmed: 24740736.
- Bonucci E. Fine structure of early cartilage calcification. *J Ultrastruct Res.* 1967; 20(1): 33–50, doi: [10.1016/s0022-5320\(67\)80034-0](https://doi.org/10.1016/s0022-5320(67)80034-0), indexed in Pubmed: 4195919.
- Ali SY, Sajdera SW, Anderson HC. Isolation and characterization of calcifying matrix vesicles from epiphyseal cartilage. *Proc Natl Acad Sci U S A.* 1970; 67(3): 1513–1520, doi: [10.1073/pnas.67.3.1513](https://doi.org/10.1073/pnas.67.3.1513), indexed in Pubmed: 5274475.
- Anderson H. Vesicles associated with calcification in the matrix of epiphyseal cartilage. *J Cell Biol.* 1969; 41(1): 59–72, doi: [10.1083/jcb.41.1.59](https://doi.org/10.1083/jcb.41.1.59), indexed in Pubmed: 5775794.
- Jaroszewicz J, Bazarnik P, Osiecka-Iwan A, et al. From matrix vesicles to miniature rocks: evolution of calcium deposits in calf costochondral junctions. *Cartilage.* 2020 [Epub ahead of print]: 1947603520941225, doi: [10.1177/1947603520941225](https://doi.org/10.1177/1947603520941225), indexed in Pubmed: 32672056.
- Anderson HC, Hodges PT, Aguilera XM, et al. Bone morphogenetic protein (BMP) localization in developing human and rat growth plate, metaphysis, epiphysis, and articular cartilage. *J Histochem Cytochem.* 2000; 48(11): 1493–1502, doi: [10.1177/002215540004801106](https://doi.org/10.1177/002215540004801106), indexed in Pubmed: 11036092.
- Nahar NN, Missana LR, Garimella R, et al. Matrix vesicles are carriers of bone morphogenetic proteins (BMPs), vascular endothelial growth factor (VEGF), and noncollagenous matrix proteins. *J Bone Miner Metab.* 2008; 26(5): 514–519, doi: [10.1007/s00774-008-0859-z](https://doi.org/10.1007/s00774-008-0859-z), indexed in Pubmed: 18758911.
- Enomoto-Iwamoto M, Iwamoto M, Mukudai Y, et al. Bone morphogenetic protein signaling is required for maintenance of differentiated phenotype, control of proliferation, and hypertrophy in chondrocytes. *J Cell Biol.* 1998; 140(2): 409–418, doi: [10.1083/jcb.140.2.409](https://doi.org/10.1083/jcb.140.2.409), indexed in Pubmed: 9442116.
- Tsumaki N, Yoshikawa H. The role of bone morphogenetic proteins in endochondral bone formation. *Cytokine & Growth Factor Reviews.* 2005; 16(3): 279–285, doi: [10.1016/j.cytogfr.2005.04.001](https://doi.org/10.1016/j.cytogfr.2005.04.001), indexed in Pubmed: 15869898.
- Salazar VS, Gamer LW, Rosen V. BMP signalling in skeletal development, disease and repair. *Nat Rev Endocrinol.* 2016; 12(4): 203–221, doi: [10.1038/nrendo.2016.12](https://doi.org/10.1038/nrendo.2016.12), indexed in Pubmed: 26893264.
- Nilsson O, Parker EA, Hegde A, et al. Gradients in bone morphogenetic protein-related gene expression across the growth plate. *J Endocrinol.* 2007; 193(1): 75–84, doi: [10.1677/joe.1.07099](https://doi.org/10.1677/joe.1.07099), indexed in Pubmed: 17400805.
- Snelling SJB, Hulley PA, Loughlin J. BMP5 activates multiple signaling pathways and promotes chondrogenic differentiation in the ATDC5 growth plate model. *Growth Factors.* 2010; 28(4): 268–279, doi: [10.3109/08977191003752296](https://doi.org/10.3109/08977191003752296), indexed in Pubmed: 20402566.
- Horner A, Bishop NJ, Bord S, et al. Immunolocalisation of vascular endothelial growth factor (VEGF) in human neonatal growth plate cartilage. *J Anat.* 1999; 194 (Pt 4): 519–524, doi: [10.1046/j.1469-7580.1999.19440519.x](https://doi.org/10.1046/j.1469-7580.1999.19440519.x), indexed in Pubmed: 10445820.
- Carlevaro MF, Cermelli S, Cancedda R, et al. Vascular endothelial growth factor (VEGF) in cartilage neovascularization and chondrocyte differentiation: auto-paracrine role during endochondral bone formation. *J Cell Sci.* 2000; 113 (Pt 1): 59–69, doi: [org/10.1242/jcs.113.1.59](https://doi.org/10.1242/jcs.113.1.59), indexed in Pubmed: 10591625.
- Engsig MT, Chen QJ, Vu TH, et al. Matrix metalloproteinase 9 and vascular endothelial growth factor are essential for osteoclast recruitment into developing long bones. *J Cell Biol.* 2000; 151(4): 879–889, doi: [10.1083/jcb.151.4.879](https://doi.org/10.1083/jcb.151.4.879), indexed in Pubmed: 11076971.

23. Ortega N, Wang Ke, Ferrara N, et al. Complementary interplay between matrix metalloproteinase-9, vascular endothelial growth factor and osteoclast function drives endochondral bone formation. *Dis Model Mech.* 2010; 3(3-4): 224–235, doi: [10.1242/dmm.004226](https://doi.org/10.1242/dmm.004226), indexed in Pubmed: [20142327](https://pubmed.ncbi.nlm.nih.gov/20142327/).
24. Yang YQ, Tan YY, Wong R, et al. The role of vascular endothelial growth factor in ossification. *Int J Oral Sci.* 2012; 4(2): 64–68, doi: [10.1038/ijos.2012.33](https://doi.org/10.1038/ijos.2012.33), indexed in Pubmed: [22722639](https://pubmed.ncbi.nlm.nih.gov/22722639/).
25. Kerkhofs J, Roberts SJ, Luyten FP, et al. Relating the chondrocyte gene network to growth plate morphology: from genes to phenotype. *PLoS One.* 2012; 7(4): e34729, doi: [10.1371/journal.pone.0034729](https://doi.org/10.1371/journal.pone.0034729), indexed in Pubmed: [22558096](https://pubmed.ncbi.nlm.nih.gov/22558096/).
26. Li Bo, Wang H, Qiu G, et al. Synergistic Effects of Vascular Endothelial Growth Factor on Bone Morphogenetic Proteins Induced Bone Formation In Vivo: Influencing Factors and Future Research Directions. *Biomed Res Int.* 2016; 2016: 2869572, doi: [10.1155/2016/2869572](https://doi.org/10.1155/2016/2869572), indexed in Pubmed: [28070506](https://pubmed.ncbi.nlm.nih.gov/28070506/).
27. Iwan A, Moskalewski S, Hyc A. Growth factor profile in calcified cartilage from the metaphysis of a calf costochondral junction, the site of initial bone formation. *Biomed Rep.* 2021; 14(6): 54, doi: [10.3892/br.2021.1430](https://doi.org/10.3892/br.2021.1430), indexed in Pubmed: [33884197](https://pubmed.ncbi.nlm.nih.gov/33884197/).
28. Brighton C, Sugioka Y, Hunt R. Cytoplasmic structures of epiphyseal plate chondrocytes. *J Bone Joint Surg.* 1973; 55(4): 771–784, doi: [10.2106/00004623-197355040-00012](https://doi.org/10.2106/00004623-197355040-00012), indexed in Pubmed: [4283751](https://pubmed.ncbi.nlm.nih.gov/4283751/).
29. Byard RW, Foster BK, Byers S. Immunohistochemical characterisation of the costochondral junction in SIDS. *J Clin Pathol.* 1993; 46(2): 108–112, doi: [10.1136/jcp.46.2.108](https://doi.org/10.1136/jcp.46.2.108), indexed in Pubmed: [8459029](https://pubmed.ncbi.nlm.nih.gov/8459029/).
30. Clark CC, Tolin BS, Brighton CT. The effect of oxygen tension on proteoglycan synthesis and aggregation in mammalian growth plate chondrocytes. *J Orthop Res.* 1991; 9(4): 477–484, doi: [10.1002/jor.1100090403](https://doi.org/10.1002/jor.1100090403), indexed in Pubmed: [2045974](https://pubmed.ncbi.nlm.nih.gov/2045974/).
31. Wozney J. Overview of bone morphogenetic proteins. *Spine.* 2002; 27(Suppl.): S2–S8, doi: [10.1097/00007632-200208151-00002](https://doi.org/10.1097/00007632-200208151-00002), indexed in Pubmed: [12205411](https://pubmed.ncbi.nlm.nih.gov/12205411/).
32. Termaat MF, Den Boer FC, Bakker FC, et al. Bone morphogenetic proteins. Development and clinical efficacy in the treatment of fractures and bone defects. *J Bone Joint Surg Am.* 2005; 87(6): 1367–1378, doi: [10.2106/JBJS.D.02585](https://doi.org/10.2106/JBJS.D.02585), indexed in Pubmed: [15930551](https://pubmed.ncbi.nlm.nih.gov/15930551/).
33. Vukicevic S, Oppermann H, Verbanac D, et al. The clinical use of bone morphogenetic proteins revisited: a novel biocompatible carrier device OSTEOGROW for bone healing. *Int Orthop.* 2014; 38(3): 635–647, doi: [10.1007/s00264-013-2201-1](https://doi.org/10.1007/s00264-013-2201-1), indexed in Pubmed: [24352822](https://pubmed.ncbi.nlm.nih.gov/24352822/).
34. James AW, LaChaud G, Shen J, et al. A review of the clinical side effects of bone morphogenetic protein-2. *Tissue Eng Part B Rev.* 2016; 22(4): 284–297, doi: [10.1089/ten.TEB.2015.0357](https://doi.org/10.1089/ten.TEB.2015.0357), indexed in Pubmed: [26857241](https://pubmed.ncbi.nlm.nih.gov/26857241/).
35. Epstein NE. Basic science and spine literature document bone morphogenetic protein increases cancer risk. *Surg Neurol Int.* 2014; 5(Suppl 15): S552–S560, doi: [10.4103/2152-7806.148039](https://doi.org/10.4103/2152-7806.148039), indexed in Pubmed: [25593776](https://pubmed.ncbi.nlm.nih.gov/25593776/).
36. Seeherman H, Wozney JM. Delivery of bone morphogenetic proteins for orthopedic tissue regeneration. *Cytokine Growth Factor Rev.* 2005; 16(3): 329–345, doi: [10.1016/j.cytogfr.2005.05.001](https://doi.org/10.1016/j.cytogfr.2005.05.001), indexed in Pubmed: [15936978](https://pubmed.ncbi.nlm.nih.gov/15936978/).
37. Park SY, Kim KH, Kim S, et al. BMP-2 Gene Delivery-Based Bone Regeneration in Dentistry. *Pharmaceutics.* 2019; 11(8), doi: [10.3390/pharmaceutics11080393](https://doi.org/10.3390/pharmaceutics11080393), indexed in Pubmed: [31387267](https://pubmed.ncbi.nlm.nih.gov/31387267/).
38. Loozen LD, Kruyt MC, Kragten AHM, et al. BMP-2 gene delivery in cell-loaded and cell-free constructs for bone regeneration. *PLoS One.* 2019; 14(7): e0220028, doi: [10.1371/journal.pone.0220028](https://doi.org/10.1371/journal.pone.0220028), indexed in Pubmed: [31365542](https://pubmed.ncbi.nlm.nih.gov/31365542/).
39. Mumcuoglu D, Fahmy-Garcia S, Ridwan Y, et al. Injectable BMP-2 delivery system based on collagen-derived microspheres and alginate induced bone formation in a time- and dose-dependent manner. *Eur Cell Mater.* 2018; 35: 242–254, doi: [10.22203/eCM.v035a17](https://doi.org/10.22203/eCM.v035a17), indexed in Pubmed: [29697853](https://pubmed.ncbi.nlm.nih.gov/29697853/).
40. Maisani M, Sindhu KR, Felon M, et al. Prolonged delivery of BMP-2 by a non-polymer hydrogel for bone defect regeneration. *Drug Deliv Transl Res.* 2018; 8(1): 178–190, doi: [10.1007/s13346-017-0451-y](https://doi.org/10.1007/s13346-017-0451-y), indexed in Pubmed: [29192408](https://pubmed.ncbi.nlm.nih.gov/29192408/).
41. Marsell R, Einhorn TA. The biology of fracture healing. *Injury.* 2011; 42(6): 551–555, doi: [10.1016/j.injury.2011.03.031](https://doi.org/10.1016/j.injury.2011.03.031), indexed in Pubmed: [21489527](https://pubmed.ncbi.nlm.nih.gov/21489527/).
42. Academy of Medical Royal Colleges. Ethical issues in paediatric organ donation. UK Donation Ethics Committee (UKDEC) 2015:4. URL: https://www.aomrc.org.uk/wp-content/uploads/2016/04/Paediatric_organ_donation_position_0615-2.pdf.
43. He T, Huang Y, Chak JC, et al. Recommendations for improving accuracy of gene expression data in bone and cartilage tissue engineering. *Sci Rep.* 2018; 8(1): 14874, doi: [10.1038/s41598-018-33242-z](https://doi.org/10.1038/s41598-018-33242-z), indexed in Pubmed: [30291289](https://pubmed.ncbi.nlm.nih.gov/30291289/).
44. Lopa S, Ceriani C, Cecchinato R, et al. Stability of housekeeping genes in human intervertebral disc, endplate and articular cartilage cells in multiple conditions for reliable transcriptional analysis. *Eur Cell Mater.* 2016; 31: 395–406, doi: [10.22203/ecm.v031a25](https://doi.org/10.22203/ecm.v031a25), indexed in Pubmed: [27232666](https://pubmed.ncbi.nlm.nih.gov/27232666/).
45. Han H, Liu L, Chen M, et al. The optimal compound reference genes for qRT-PCR analysis in the developing rat long bones under physiological conditions and prenatal dexamethasone exposure model. *Reprod Toxicol.* 2020; 98: 242–251, doi: [10.1016/j.reprotox.2020.10.008](https://doi.org/10.1016/j.reprotox.2020.10.008), indexed in Pubmed: [33086097](https://pubmed.ncbi.nlm.nih.gov/33086097/).
46. Arnott JA, Lambi AG, Mundy C, et al. The role of connective tissue growth factor (CTGF/CCN2) in skeletogenesis. *Crit Rev Eukaryot Gene Expr.* 2011; 21(1): 43–69, doi: [10.1615/critrevukargeneexpr.v21.i1.40](https://doi.org/10.1615/critrevukargeneexpr.v21.i1.40), indexed in Pubmed: [21967332](https://pubmed.ncbi.nlm.nih.gov/21967332/).
47. Ramazani Y, Knops N, Elmonem MA, et al. Connective tissue growth factor (CTGF) from basics to clinics. *Matrix Biol.* 2018; 68-69: 44–66, doi: [10.1016/j.matbio.2018.03.007](https://doi.org/10.1016/j.matbio.2018.03.007), indexed in Pubmed: [29574063](https://pubmed.ncbi.nlm.nih.gov/29574063/).
48. Bell PA, Dennis EP, Hartley CL, et al. Mesencephalic astrocyte-derived neurotrophic factor is an important factor in chondrocyte ER homeostasis. *Cell Stress Chaperones.* 2019; 24(1): 159–173, doi: [10.1007/s12192-018-0953-7](https://doi.org/10.1007/s12192-018-0953-7), indexed in Pubmed: [30543055](https://pubmed.ncbi.nlm.nih.gov/30543055/).
49. Reddy S, Devlin R, Menaa C, et al. Isolation and characterization of a cDNA clone encoding a novel peptide (OSF) that enhances osteoclast formation and bone resorption. *J Cell Physiol.* 1998; 177(4): 636–645, doi: [10.1002/\(SICI\)1097-4652\(199812\)177:4<636::AID-JCP14>3.0.CO;2-H](https://doi.org/10.1002/(SICI)1097-4652(199812)177:4<636::AID-JCP14>3.0.CO;2-H), indexed in Pubmed: [10092216](https://pubmed.ncbi.nlm.nih.gov/10092216/).
50. Steiglitz BM, Ayala M, Narayanan K, et al. Bone morphogenetic protein-1/Tolloid-like proteinases process dentin matrix protein-1. *J Biol Chem.* 2004; 279(2): 980–986, doi: [10.1074/jbc.M310179200](https://doi.org/10.1074/jbc.M310179200), indexed in Pubmed: [14578349](https://pubmed.ncbi.nlm.nih.gov/14578349/).
51. Vadon-Le Goff S, Hulmes DJS, Moali C. BMP-1/tolloid-like proteinases synchronize matrix assembly with growth factor activation to promote morphogenesis and tissue remodeling. *Matrix Biol.* 2015; 44-46: 14–23, doi: [10.1016/j.matbio.2015.02.006](https://doi.org/10.1016/j.matbio.2015.02.006), indexed in Pubmed: [25701650](https://pubmed.ncbi.nlm.nih.gov/25701650/).
52. Mailhot G, Yang M, Mason-Savas A, et al. BMP-5 expression increases during chondrocyte differentiation in vivo and in vit-

- ro and promotes proliferation and cartilage matrix synthesis in primary chondrocyte cultures. *J Cell Physiol.* 2008; 214(1): 56–64, doi: [10.1002/jcp.21164](https://doi.org/10.1002/jcp.21164), indexed in Pubmed: [17541940](https://pubmed.ncbi.nlm.nih.gov/17541940/).
53. Ye F, Xu H, Yin H, et al. The role of BMP6 in the proliferation and differentiation of chicken cartilage cells. *PLoS One.* 2019; 14(7): e0204384, doi: [10.1371/journal.pone.0204384](https://doi.org/10.1371/journal.pone.0204384), indexed in Pubmed: [31260450](https://pubmed.ncbi.nlm.nih.gov/31260450/).
 54. Yakar S, Werner H, Rosen CJ. Insulin-like growth factors: actions on the skeleton. *J Mol Endocrinol.* 2018; 61(1): T115–T137, doi: [10.1530/JME-17-0298](https://doi.org/10.1530/JME-17-0298), indexed in Pubmed: [29626053](https://pubmed.ncbi.nlm.nih.gov/29626053/).
 55. Racine HL, Serrat MA. The Actions of IGF-1 in the Growth Plate and Its Role in Postnatal Bone Elongation. *Curr Osteoporos Rep.* 2020; 18(3): 210–227, doi: [10.1007/s11914-020-00570-x](https://doi.org/10.1007/s11914-020-00570-x), indexed in Pubmed: [32415542](https://pubmed.ncbi.nlm.nih.gov/32415542/).
 56. Wozney JM, Rosen V. Bone morphogenetic protein and bone morphogenetic protein gene family in bone formation and repair. *Clin Orthop Relat Res.* 1998(346): 26–37, indexed in Pubmed: [9577407](https://pubmed.ncbi.nlm.nih.gov/9577407/).
 57. Wutzl A, Rauner M, Seemann R, et al. Bone morphogenetic proteins 2, 5, and 6 in combination stimulate osteoblasts but not osteoclasts in vitro. *J Orthop Res.* 2010; 28(11): 1431–1439, doi: [10.1002/jor.21144](https://doi.org/10.1002/jor.21144), indexed in Pubmed: [20872578](https://pubmed.ncbi.nlm.nih.gov/20872578/).
 58. Zhou N, Li Qi, Lin X, et al. BMP2 induces chondrogenic differentiation, osteogenic differentiation and endochondral ossification in stem cells. *Cell Tissue Res.* 2016; 366(1): 101–111, doi: [10.1007/s00441-016-2403-0](https://doi.org/10.1007/s00441-016-2403-0), indexed in Pubmed: [27083447](https://pubmed.ncbi.nlm.nih.gov/27083447/).
 59. Bahamonde M, Lyons K. BMP3: To Be or Not To Be a BMP. *J Bone Joint Surg Am-American Volume.* 2001; 83: S1–S6–S1–62, doi: [10.2106/00004623-200100001-00008](https://doi.org/10.2106/00004623-200100001-00008), indexed in Pubmed: [11263666](https://pubmed.ncbi.nlm.nih.gov/11263666/).
 60. Gamer LW, Cox K, Carlo JM, et al. Overexpression of BMP3 in the developing skeleton alters endochondral bone formation resulting in spontaneous rib fractures. *Dev Dyn.* 2009; 238(9): 2374–2381, doi: [10.1002/dvdy.22048](https://doi.org/10.1002/dvdy.22048), indexed in Pubmed: [19653325](https://pubmed.ncbi.nlm.nih.gov/19653325/).
 61. Peng H, Wright V, Usas A, et al. Synergistic enhancement of bone formation and healing by stem cell-expressed VEGF and bone morphogenetic protein-4. *J Clin Invest.* 2002; 110(6): 751–759, doi: [10.1172/JCI15153](https://doi.org/10.1172/JCI15153), indexed in Pubmed: [12235106](https://pubmed.ncbi.nlm.nih.gov/12235106/).
 62. Shum L, Wang X, Kane AA, et al. BMP4 promotes chondrocyte proliferation and hypertrophy in the endochondral cranial base. *Int J Dev Biol* 2003;47(6):423–431, indexed in Pubmed: [14598792](https://pubmed.ncbi.nlm.nih.gov/14598792/).
 63. Gao X, Usas A, Lu A, et al. BMP2 is superior to BMP4 for promoting human muscle-derived stem cell-mediated bone regeneration in a critical-sized calvarial defect model. *Cell Transplant.* 2013; 22(12): 2393–2408, doi: [10.3727/096368912X658854](https://doi.org/10.3727/096368912X658854), indexed in Pubmed: [23244588](https://pubmed.ncbi.nlm.nih.gov/23244588/).
 64. Chang SC, Hoang B, Thomas JT, et al. Cartilage-derived morphogenetic proteins. New members of the transforming growth factor-beta superfamily predominantly expressed in long bones during human embryonic development. *J Biol Chem.* 1994; 269(45): 28227–28234, indexed in Pubmed: [7961761](https://pubmed.ncbi.nlm.nih.gov/7961761/).
 65. Tsumaki N, Tanaka K, Arikawa-Hirasawa E, et al. Role of CDMP-1 in skeletal morphogenesis: promotion of mesenchymal cell recruitment and chondrocyte differentiation. *J Cell Biol.* 1999; 144(1): 161–173, doi: [10.1083/jcb.144.1.161](https://doi.org/10.1083/jcb.144.1.161), indexed in Pubmed: [9885252](https://pubmed.ncbi.nlm.nih.gov/9885252/).
 66. Storm EE, Huynh TV, Copeland NG, et al. Limb alterations in brachypodism mice due to mutations in a new member of the TGF beta-superfamily. *Nature.* 1994; 368(6472): 639–643, doi: [10.1038/368639a0](https://doi.org/10.1038/368639a0), indexed in Pubmed: [8145850](https://pubmed.ncbi.nlm.nih.gov/8145850/).
 67. Polinkovsky A, Robin NH, Thomas JT, et al. Mutations in CDMP1 cause autosomal dominant brachydactyly type C. *Nat Genet.* 1997; 17(1): 18–19, doi: [10.1038/ng0997-18](https://doi.org/10.1038/ng0997-18), indexed in Pubmed: [9288091](https://pubmed.ncbi.nlm.nih.gov/9288091/).
 68. Zhang X, Zara J, Siu RK, et al. The role of NELL-1, a growth factor associated with craniosynostosis, in promoting bone regeneration. *J Dent Res.* 2010; 89(9): 865–878, doi: [10.1177/0022034510376401](https://doi.org/10.1177/0022034510376401), indexed in Pubmed: [20647499](https://pubmed.ncbi.nlm.nih.gov/20647499/).
 69. Tanjaya J, Zhang Y, Lee S, et al. Efficacy of Intraperitoneal Administration of PEGylated NELL-1 for Bone Formation. *Biores Open Access.* 2016; 5(1): 159–170, doi: [10.1089/biores.2016.0018](https://doi.org/10.1089/biores.2016.0018), indexed in Pubmed: [27354930](https://pubmed.ncbi.nlm.nih.gov/27354930/).
 70. James AW, Shen J, Tsuei R, et al. NELL-1 induces Sca-1 + mesenchymal progenitor cell expansion in models of bone maintenance and repair. *JCI Insight.* 2017; 2(12), doi: [10.1172/jci.insight.92573](https://doi.org/10.1172/jci.insight.92573), indexed in Pubmed: [28614787](https://pubmed.ncbi.nlm.nih.gov/28614787/).
 71. Qi H, Kim JK, Ha P, et al. Inactivation of nell-1 in chondrocytes significantly impedes appendicular skeletogenesis. *J Bone Miner Res.* 2019; 34(3): 533–546, doi: [10.1002/jbmr.3615](https://doi.org/10.1002/jbmr.3615), indexed in Pubmed: [30352124](https://pubmed.ncbi.nlm.nih.gov/30352124/).
 72. Chen G, Deng C, Li YP. TGF- β and BMP signaling in osteoblast differentiation and bone formation. *Int J Biol Sci.* 2012; 8(2): 272–288, doi: [10.7150/ijbs.2929](https://doi.org/10.7150/ijbs.2929), indexed in Pubmed: [22298955](https://pubmed.ncbi.nlm.nih.gov/22298955/).
 73. Wu M, Chen G, Li YP. TGF- β and BMP signaling in osteoblast, skeletal development, and bone formation, homeostasis and disease. *Bone Res.* 2016; 4: 16009, doi: [10.1038/boneres.2016.9](https://doi.org/10.1038/boneres.2016.9), indexed in Pubmed: [27563484](https://pubmed.ncbi.nlm.nih.gov/27563484/).
 74. Wezeman FH, Bollnow MR. Immunohistochemical localization of fibroblast growth factor-2 in normal and brachymorphic mouse tibial growth plate and articular cartilage. *Histochem J.* 1997; 29(6): 505–514, doi: [10.1023/a:1026415707378](https://doi.org/10.1023/a:1026415707378), indexed in Pubmed: [9248858](https://pubmed.ncbi.nlm.nih.gov/9248858/).
 75. Nagai H, Tsukuda R, Mayahara H. Effects of basic fibroblast growth factor (bFGF) on bone formation in growing rats. *Bone.* 1995; 16(3): 367–373, doi: [10.1016/8756-3282\(94\)00049-2](https://doi.org/10.1016/8756-3282(94)00049-2).
 76. Kusafuka K, Hiraki Y, Shukunami C, et al. Cartilage-specific matrix protein, chondromodulin-I (ChM-I), is a strong angiogenic inhibitor in endochondral ossification of human neonatal vertebral tissues in vivo: relationship with angiogenic factors in the cartilage. *Acta Histochem.* 2002; 104(2): 167–175, doi: [10.1078/0065-1281-00642](https://doi.org/10.1078/0065-1281-00642), indexed in Pubmed: [12086337](https://pubmed.ncbi.nlm.nih.gov/12086337/).
 77. Gerber HP, Vu TH, Ryan AM, et al. VEGF couples hypertrophic cartilage remodeling, ossification and angiogenesis during endochondral bone formation. *Nat Med.* 1999; 5(6): 623–628, doi: [10.1038/9467](https://doi.org/10.1038/9467), indexed in Pubmed: [10371499](https://pubmed.ncbi.nlm.nih.gov/10371499/).
 78. Nagao M, Hamilton JL, Kc R, et al. Vascular endothelial growth factor in cartilage development and osteoarthritis. *Sci Rep.* 2017; 7(1): 13027, doi: [10.1038/s41598-017-13417-w](https://doi.org/10.1038/s41598-017-13417-w), indexed in Pubmed: [29026147](https://pubmed.ncbi.nlm.nih.gov/29026147/).
 79. Vadala G, Russo F, Musumeci M, et al. Targeting VEGF-A in cartilage repair and regeneration: state of the art and perspectives. *J Biol Regul Homeost Agents* 2018;32(6 suppl.): 217–224. , indexed in Pubmed: [30644305](https://pubmed.ncbi.nlm.nih.gov/30644305/).
 80. Horner A, Kemp P, Summers C, et al. Expression and distribution of transforming growth factor-beta isoforms and their signaling receptors in growing human bone. *Bone.* 1998; 23(2): 95–102, doi: [10.1016/s8756-3282\(98\)00080-5](https://doi.org/10.1016/s8756-3282(98)00080-5), indexed in Pubmed: [9701467](https://pubmed.ncbi.nlm.nih.gov/9701467/).

Submitted: 2 June, 2021

Accepted after reviews: 13 July, 2021

Available as AoP: 30 July, 2021

SDF-1/CXCR4 axis promotes osteogenic differentiation of BMSCs through the JAK2/STAT3 pathway

Wen Xiong, Xin Guo, Xianhua Cai

The First School of Clinical Medicine, Southern Medical University, Guangdong, China

Abstract

Introduction. This study aimed to investigate the effects of stromal cell-derived factor-1 (SDF-1) and activation of its receptor, chemokine receptor 4 (CXCR4), on the osteogenic differentiation of bone marrow mesenchymal stem cells (BMSCs), and the key signaling mechanisms involved in these effects.

Material and methods. BMSCs were treated with 100 $\mu\text{g/L}$ SDF-1 and cultured in osteogenic medium for 7 days. RT-qPCR and western blotting were used to detect the protein and mRNA levels of Janus kinase 2 (JAK2), signal transducer and activator of transcription 3 (STAT3), Runt-related transcription factor 2 (Runx2), and osteocalcin (OCN). Alizarin-red staining was used to detect the mineralization-inducing ability of the cells.

Results. After BMSCs were treated with SDF-1, the levels of JAK2 mRNA, STAT3 mRNA, and protein phosphorylation increased, the number of mineralized nodules of BMSCs increased, and the osteogenic-differentiation ability was enhanced. In addition, after BMSCs were treated with an inhibitor of JAK2 phosphorylation, the levels of JAK2, STAT3, Runx2, and OCN decreased significantly, the number of mineralized nodules of BMSCs also decreased, and the osteogenic-differentiation ability decreased. The inhibition of CXCR4-treated BMSCs further confirmed that SDF-1/CXCR4 activated JAK2/STAT3 to regulate the osteogenic differentiation of BMSCs.

Conclusions. SDF-1/CXCR4 promoted the osteogenic differentiation of BMSCs through JAK2/STAT3 activation. (*Folia Histochemica et Cytobiologica* 2021, Vol. 59, No. 3, 187–194)

Key words: BMSCs; osteogenic differentiation; SDF-1; CXCR4; JAK2/STAT3; Runx2, osteocalcin; alizarin red

Introduction

Bone marrow mesenchymal stem cells (BMSCs) are non-hematopoietic stem cells present in the bone marrow. BMSCs cultured *in vitro* can adhere to the vessel wall and proliferate rapidly, exhibiting a fibroblast-like long fusiform shape. BMSCs have the potential for cross-system and cross-germ differentiation under the action of a specific microenvironment and suitable cytokines/growth factors. They can differentiate into mesodermal and neuroectodermal cells, such as osteoblasts, chondrocytes, endothelial cells, and nerve cells;

accordingly, they have recently become a resource for tissue repair [1, 2]. Osteogenic differentiation of BMSCs is closely related to bone-related diseases: for example, the inhibition of osteoporosis [3]. Chen *et al.* demonstrated that osteogenic differentiation of BMSCs promotes new bone formation, which in turn, accelerates fracture healing [4]. Therefore, it is important to study the molecular mechanisms related to the differentiation of BMSCs.

Stromal cell-derived factor-1 (SDF-1) is a chemokine protein. It mainly binds to CXCR4 and plays an important role in the homeostasis of organ development and hematopoietic cell differentiation [5, 6]. The interaction between SDF-1 and CXCR4 can control the migration, osteogenic differentiation, and survival of BMSCs under oxidative stress [7–11]. SDF-1 has also been shown to accelerate and enhance calcium deposition, regulate a variety of osteogenic factors such as runt-related

Correspondence address: Xianhua Cai
The First School of Clinical Medicine,
Southern Medical University,
No.1023, South Shatai Road, Baiyun District,
Guangzhou 510515, Guangdong, China
e-mail: whcaixh@163.com

This article is available in open access under Creative Common Attribution-Non-Commercial-No Derivatives 4.0 International (CC BY-NC-ND 4.0) license, allowing to download articles and share them with others as long as they credit the authors and the publisher, but without permission to change them in any way or use them commercially.

transcription factor 2 (Runx2), bone morphogenetic protein 2 (BMP2), and osteocalcin (OCN), enhance alkaline phosphatase activity, and maintain bone homeostasis by assisting BMSCs to migrate to injured tissues [12, 13]. However, how the SDF-1/CXCR4 axis regulates the osteogenic differentiation of BMSCs remains unclear.

Janus kinase 2/signal transducer and activator of transcription 3 (JAK2/STAT3) signaling in osteoblasts plays an important role in bone biology [14]. By contrast, activation of JAK2/STAT3 signaling in BMSCs has been reported to inhibit bone regeneration [15]. Therefore, the exact role of JAK2/STAT3 signaling in bone biology remains controversial. The collection, proliferation, and osteogenic differentiation of mesenchymal stem cells are important for the treatment of bone defects [16]. In recent reports, JAK2/STAT3 signaling plays an important role in the proliferation and osteogenic differentiation of BMSCs [17], and SDF-1 can induce the activation of STAT3 and improve the migration of bone marrow stromal cells in a middle cerebral artery occlusion stroke model [18]. Nevertheless, whether SDF-1/CXCR4 can induce BMSC differentiation by promoting JAK2/STAT3 pathway activation has not been reported. In view of the current research, this study aimed to explore the effect of SDF-1 and the activation of its receptor, CXCR4, on the osteogenic differentiation of bone marrow mesenchymal stem cells (BMSCs) and the key signaling mechanism.

Materials and methods

Cell culture. Human bone marrow mesenchymal stem cells (hBMSCs) were purchased from ScienCell (San Diego, CA, USA) and cultured in α -MEM (HyClone, Logan, UT, USA) containing 15% FBS, 100 μ M L-ascorbic acid, 2 mM L-glutamine, 100 U/mL penicillin, and 100 μ g/mL streptomycin (Yaanda Biotechnology Co., Ltd., Beijing, China), at 37 °C in a 5% CO₂ cell culture chamber.

SDF-1 treatment and cell grouping. The cells (1 × 10⁵ cells/mL) were cultured in 12-well plates with osteogenic differentiation medium (α -MEM + 0.1 μ M dexamethasone + 10 mM β -glycerophosphate + 50 μ g/mL ascorbic acid) to induce osteogenic differentiation of hBMSCs for 7 days. The experiment was divided into two groups: the control group (cultured in osteogenic differentiation medium for 7 days), and the SDF-1 (PeproTech, East Windsor, NJ, USA) induced group (100 μ g/L SDF-1 was added to the cells for 30 min and the cells were washed with phosphate-buffered saline (PBS) which were then cultured in osteogenic differentiation medium for 7 days). Cells need to be washed with culture medium after replacing the medium after addition of drugs.

AG490 treatment and cell grouping. The experiment was divided into four groups: the control group, the AG490 (JAK2 phosphorylation inhibitor, MCE, China) group (cells were treated with 50 μ mol/L AG490 for 72 h and cultured in osteogenic differentiation medium for 7 days), the SDF-1 group (100 μ g/L SDF-1 was added to the cells for 30 min which were then cultured in osteogenic differentiation medium for 7 days), the SDF-1 + AG490 group (the cells were treated with 100 μ g/L SDF-1 30 min, and with 50 μ mol/L AG490 for 72 h and cultured in osteogenic differentiation medium for 7 days). Cells need to be washed with culture medium after replacing the medium after addition of drugs.

AMD3100 treatment and cell grouping. The experiment was divided into four groups: the control group, the AMD3100 (SDF-1/CXCR4 receptor antagonist, MCE, China) group (5 μ g/mL AMD3100 were added to the cell culture for 48 h and the cells were cultured in osteogenic differentiation medium for 7 days), the SDF-1 group (100 μ g/L SDF-1 was added for 30 min and the cells were cultured in osteogenic differentiation medium for 7 days), the SDF-1 + AMD3100 group (100 μ g/L SDF-1 was added for 30 min, 5 μ g/mL AMD3100 was added for 48 h and the cells were cultured in osteogenic differentiation medium for 7 days). Cells need to be washed with culture medium after replacing the medium after addition of drugs.

RT-qPCR. Total RNA was extracted using TRIzol reagent (Invitrogen, Carlsbad, CA, USA), and then DNA was removed using a turbo DNase Kit (Ambion). The extracted RNA was quantified using a NanoDrop spectrophotometer. A Primescript real-time (RT) kit (Takara Bio, Shiga, Japan) was used to synthesize complementary DNA using 1000 ng of total RNA. SYBR Select Master Mix (Applied Biosystems, Waltham, MA, USA) was used to perform quantitative real-time PCR on an Applied Biosystems 7900HT system. Glyceraldehyde 3-phosphate dehydrogenase (GAPDH) was used as the standardized internal reference for JAK2, STAT3, Runx2, and OCN mRNA. The CT value was calculated using the 2^{- $\Delta\Delta$ Ct} method. The primer sequences used in this study were as follows:

JAK2, F:5'-TCTGGGGAGTATGTTGCAGAA-3',
R:5'-AGACATGGTTGGGTGGATACC-3';
STAT3, F:5'-CAGCAGCTTGACACACGGTA-3',
R:5'-AAACACCAAAGTGGCATGTGA-3';
Runx2, F:5'-CGCGTTGCATAGTCACAAAA-3',
R:5'-AGTGCAGGGTCCGAGGTATT-3';
OCN, F:5'-CACTCCTCGCCCTATTGGC-3',
R:5'-CCCTCCTGCTTGGACACAAAG-3';
GAPDH, F:5'-TGTGGGCATCAATGGATTTGG-3',
R:5'-CCCTCCTGCTTGGACACAAAG-3'.

Western blotting. Total cellular proteins were extracted using a radioimmunoprecipitation assay (RIPA; Beyotime,

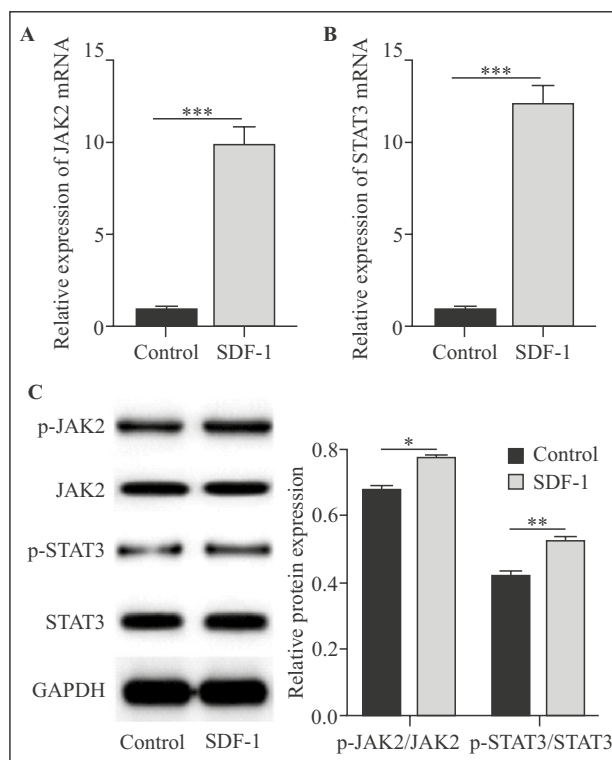


Figure 1. Effect of SDF-1 on JAK2/STAT3 mRNA and protein levels of SDF-1-treated BMSCs. BMSCs were treated with SDF-1 (100 $\mu\text{g/L}$) for 30 min (A and B) and cells were collected after 7 days. The mRNA levels of JAK2 and STAT3 were detected by RT-qPCR. Western blotting was used to detect the levels of the JAK2/STAT3-related proteins: p-JAK2, JAK2, p-STAT3, and STAT3. Data are means of three independent experiments, and each independent experiment was repeated with three replicate wells. * $P < 0.05$, ** $P < 0.01$, *** $P < 0.001$ vs. control group.

Shanghai, China). The total protein was separated by electrophoresis and transferred to a polyvinylidene fluoride (PVDF) membrane (Millipore, Billerica, MA, USA). After blocking with 5% skim milk for 2 h, the membrane was incubated with the primary antibodies — Anti-Runx2 (ab192256, 1:1000, Abcam, Cambridge, UK), anti-OCN (ab270202, 1:1000, Abcam), anti-JAK2 (ab108596, 1:1000, Abcam), anti-STAT3 (ab68153, 1:1000, Abcam) at 4°C overnight. The next day, the membrane was incubated with the corresponding secondary antibody at room temperature for 2 h. Immune response bands were exposed to enhanced chemiluminescence (ECL; Thermo Fisher Science, Waltham, MA, USA) and analyzed using ImageJ software (NIH, Bethesda, MD, USA).

Alizarin-red staining. After 7 days, the cells from the six-well plates of each group were collected. The cells were removed from the culture medium, then washed twice with PBS. The cells were fixed with 10% formaldehyde at room temperature for 15 min. The cells were rinsed twice with redistilled water, and 40 mM alizarin red dye solution was added, 1 mL per well. The cells were incubated at room temperature for 20 min and slightly oscillated. To remove dyes that were not fully bound, the cells were rinsed with redistilled water

and shaken for 5 min; this was repeated four times. Excess redistilled water was allowed to absorb before observation under an inverted microscope.

Statistical analysis. GraphPad Prism 8 (GraphPad Inc., La Jolla, CA, USA) was used for statistical analysis. The differences between experimental groups were analyzed by Student's *t*-test. Single-factor analysis of variance (ANOVA) was used for comparison among groups and then a minimum-significant-difference test was performed. $P < 0.05$ was considered to be statistically significant.

Results

Effect of SDF-1 on JAK2/STAT3 levels in BMSCs

To explore the effect of the SDF-1/CXCR4 axis on BMSCs, BMSCs were treated with SDF-1 (100 $\mu\text{g/L}$). The levels of the JAK2/STAT3-related proteins — p-JAK2, JAK2, p-STAT3, and STAT3 — and their mRNAs were detected by RT-qPCR and Western blotting. The results showed that the levels of JAK2 mRNA, STAT3 mRNA, and their protein phosphorylation in the SDF-1 treated group were higher than those of the non-SDF-1 group ($p < 0.05$, Fig. 1A–C).

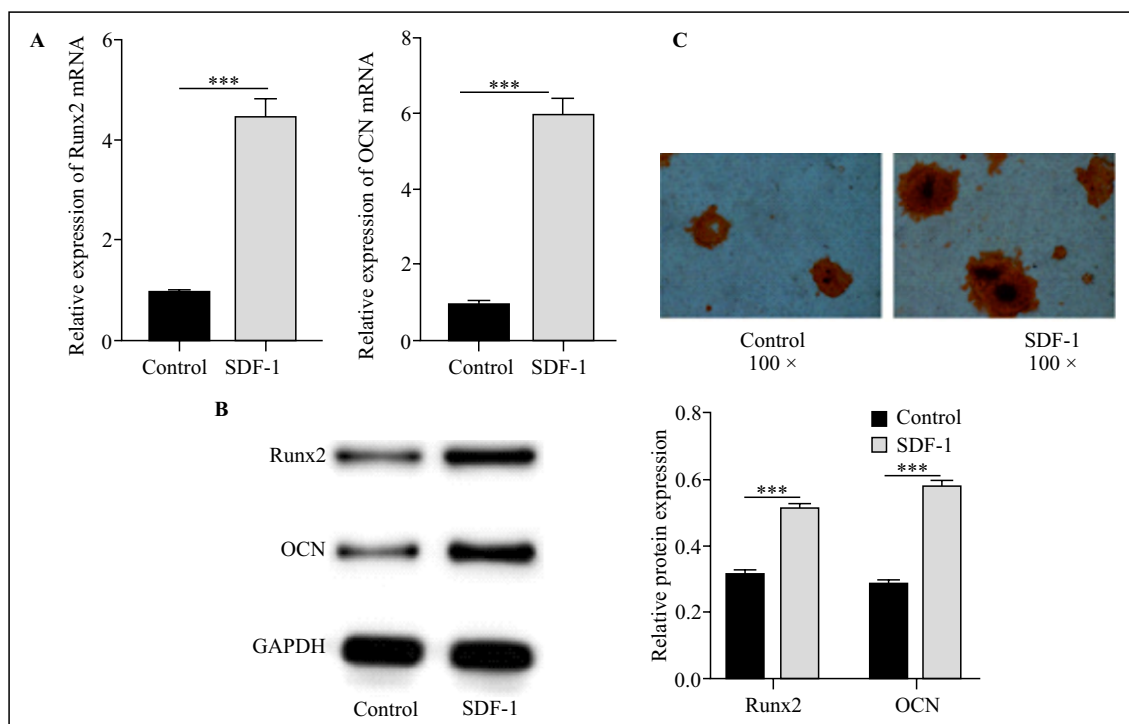


Figure 2. SDF-1 regulated osteogenic differentiation of BMSCs. BMSCs were treated with SDF-1 (100 $\mu\text{g/L}$) for 30 min and cells were collected after 7 days. **A.** The mRNA levels of Runx2 and osteocalcin (OCN) were detected by RT-qPCR. **B.** The levels of Runx2 and OCN were detected by western blotting. **C.** Alizarin-red staining assay used to detect the mineralization-induction ability of the cells. Data are means of three independent experiments, and each independent experiment was repeated with three replicate wells. *** $P < 0.001$ vs. control group.

Thus, the results showed that SDF-1 promoted the activation of JAK2/STAT3 in BMSCs.

SDF-1 regulated osteogenic differentiation of BMSCs

Next, we explored the effect of SDF-1/CXCR4 on the osteogenic differentiation of BMSCs. RT-qPCR and Western blotting were used to detect the expression of the osteogenesis-related genes — Runx2 and OCN. The results showed that, compared with the control group, the expression levels of Runx2, OCN, and their mRNA were significantly upregulated. In addition, the results of alizarin-red staining showed that the number of mineralized nodules and the osteogenic-differentiation ability of BMSCs in the SDF-1-treated cells were higher than in the control cells. These results suggested that SDF-1/CXCR4 could promote the osteogenic differentiation of BMSCs ($p < 0.05$, Fig. 2A–C).

JAK2/STAT3 participated in SDF-1-mediated osteogenic differentiation of BMSCs

JAK2/STAT3 signaling has been shown to play an important role in the proliferation and osteogenic differentiation of BMSCs [13]. However, whether JAK2/STAT3 is involved in SDF-1-mediated osteogenic

differentiation of BMSCs remains unclear. BMSCs were treated with the JAK2 phosphorylation inhibitor, AG490. First, JAK2/STAT3-related protein and mRNA levels were detected by RT-qPCR and western blotting; the results showed that the levels of JAK2, STAT3 mRNA, and the phosphorylation of their proteins in the AG490 group were significantly lower than in the SDF-1 group ($p < 0.05$, Fig. 3A–C). We then explored the effect of the JAK2 phosphorylation inhibitor, AG490, on the osteogenic differentiation of BMSCs. RT-qPCR and western blot results showed that Runx2, OCN, and their mRNA levels were significantly downregulated in the SDF-1 + AG490 group compared with the SDF-1 group ($p < 0.05$, Fig. 3D–F). Alizarin-red staining showed that the number of mineralized nodules and osteogenic-differentiation ability of BMSCs in the AG490 group were lower than in the SDF-1 group ($p < 0.05$, Fig. 3G).

SDF-1/CXCR4 activated JAK2/STAT3 pathway to regulate osteogenic differentiation of BMSCs

To further verify the role of SDF-1/CXCR4 in the osteogenic differentiation of BMSCs by activating JAK2/STAT3, we treated BMSCs with the CXCR4 inhibitor, AMD3100. The results of western blotting

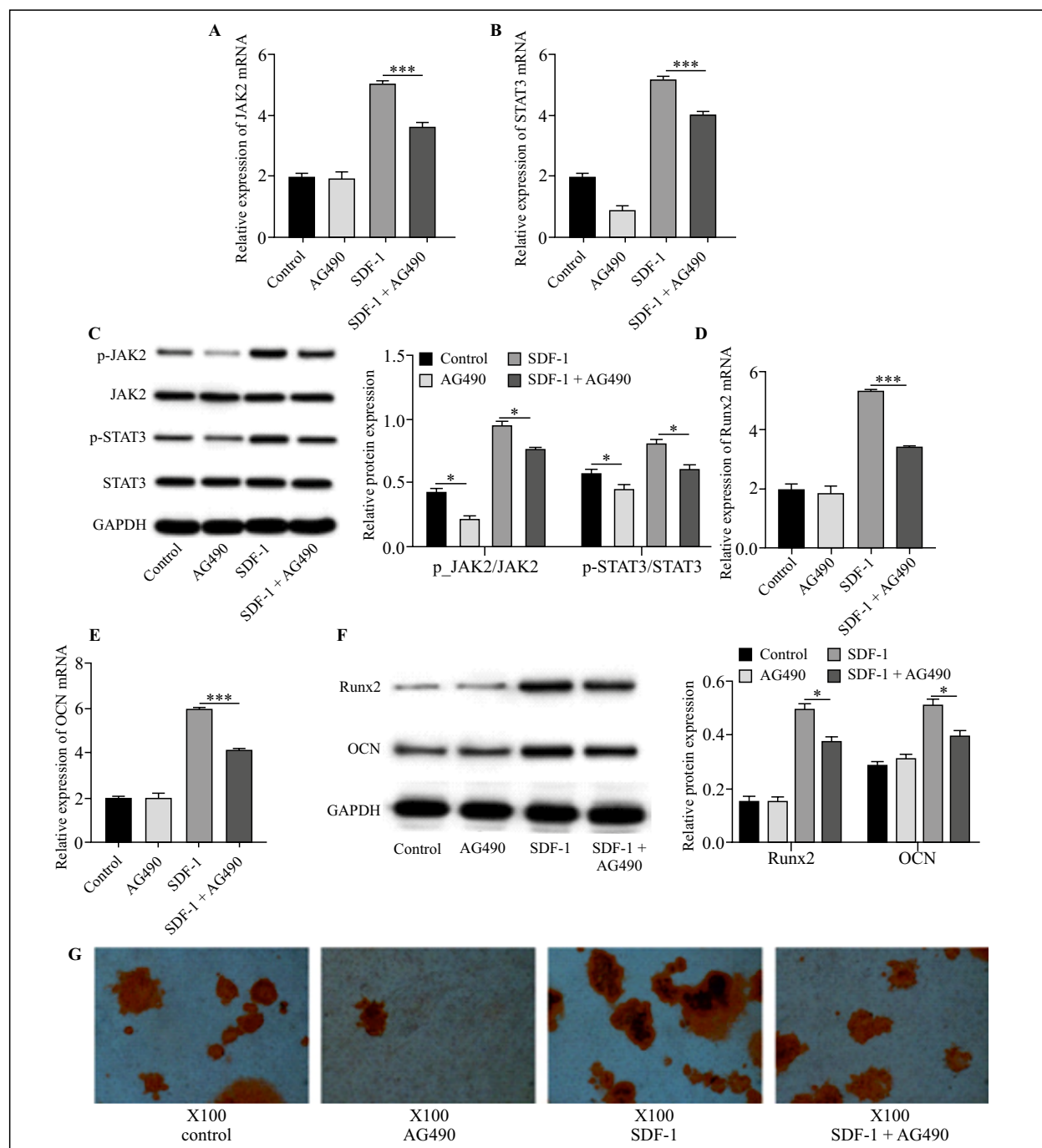


Figure 3. JAK2/STAT3 participated in SDF-1-mediated osteogenic differentiation of BMSCs. BMSCs were treated first with SDF-1 (100 $\mu\text{g/L}$) for 30 min and then with the JAK2 phosphorylation inhibitor, AG490 (5 $\mu\text{g/mL}$) for 72 h and cells were collected after 7 days. **A.** and **B.** Levels of JAK2 mRNA and STAT3 mRNA were detected by RT-qPCR. **C.** Western blotting was used to detect the levels of JAK2/STAT3-related proteins p-JAK2, JAK2, p-STAT3, and STAT3. **D.** and **E.** RT-qPCR was used to detect the levels of Runx2 mRNA and OCN mRNA. **F.** The levels of Runx2 and OCN were detected by Western blotting. **G.** Alizarin-red staining assay was used to detect the ability of cells to induce mineralization. Data are means of three independent experiments, and each independent experiment was repeated with three replicate wells. * $P < 0.05$, *** $P < 0.001$ compared with SDF-1 group.

showed that the phosphorylation of JAK2 and STAT3 proteins was downregulated compared with the control group. In the SDF-1-treated group, AMD3100 treatment reversed the effect of SDF-1 on JAK2 and

STAT3 protein phosphorylation ($p < 0.05$, Fig. 4A). Taken together, these results suggest that SDF-1/CXCR4 activated JAK2/STAT3 to regulate the osteogenic differentiation of BMSCs (Fig. 4B).

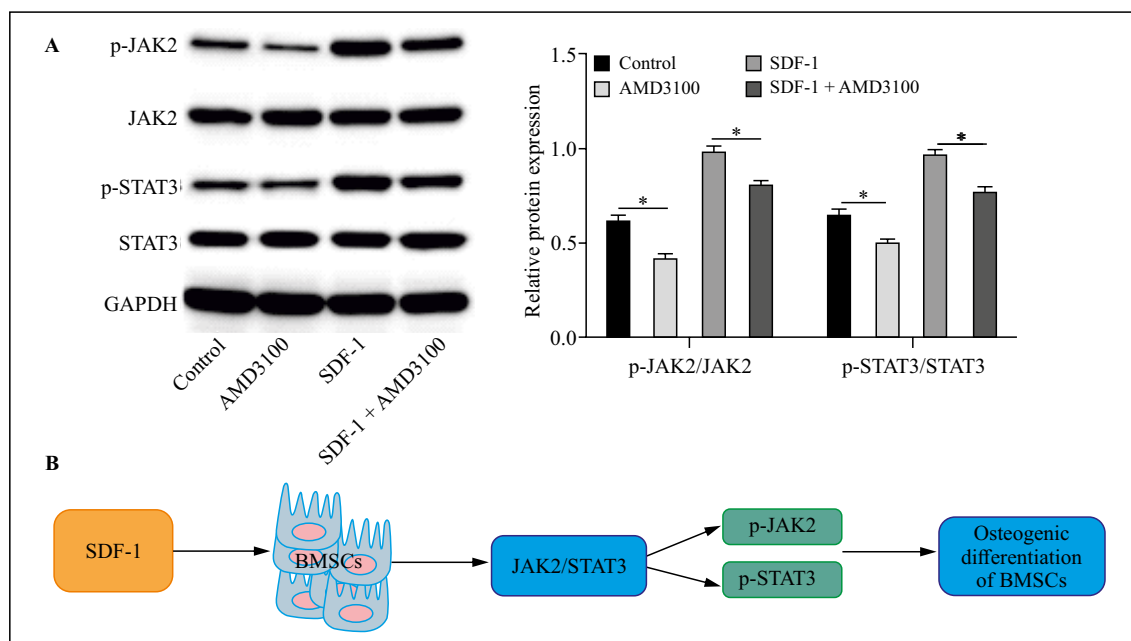


Figure 4. SDF-1/CXCR4 activated JAK2/STAT3 pathway to regulate osteogenic differentiation of BMSCs. BMSCs were first with SDF-1 (100 $\mu\text{g/L}$) for 30 min and then exposed for 48 h to the CXCR4 inhibitor AMD3100 (5 $\mu\text{g/mL}$), afterwards the cells were collected after 7 days. **A.** The levels of p-JAK2, JAK2, p-STAT3, and STAT3 were detected by Western blotting. **B.** The diagram shows postulated mechanisms of SDF-1-induced osteogenic differentiation of BMSCs by the promotion of the SDF-1/CXCR4 activated JAK2/STAT3 signaling. Data are means of three independent experiments, and each independent experiment was repeated with three replicate wells. * $P < 0.05$, compared to the control or SDF-1 group.

Discussion

JAK2 is a non-receptor tyrosine kinase member of the Janus kinase (JAKs) family, which serves as a cytoplasmic signaling component of cytokine receptors and is activated by cytokine-mediated trans-phosphorylation, leading to receptor phosphorylation and recruitment and phosphorylation of signal transducer and activator of transcription (STAT) proteins [19]. As a downstream substrate of JAK2, STAT3 is an inducible monomer transcription factor. After recruitment by JAK2, STAT3 dimerizes and translocates to the nucleus after Tyr705 phosphorylation. The activation of STAT3 signaling can induce changes in the expression of downstream molecules and regulate biological processes such as cell migration, proliferation, and apoptosis [20]. Previous studies have shown that the JAK2/STAT3 pathway is involved in the progression of colorectal cancer [18] and central nervous system diseases related to experimental cerebral ischemia [21]. There are also relevant reports on bone defect diseases. For example, Yu *et al.* [13] confirmed that inhibition of JAK2/STAT3 signal transduction can inhibit the proliferation and osteogenic differentiation of bone-marrow stromal cells and impede the healing of bone defects, indicating that JAK2/STAT3 plays an

important role in the proliferation and osteogenesis of bone marrow stromal cells. AG490, the inhibitor of JAK2, can reduce the phosphorylation of STAT3 by selectively inactivating JAK2. The therapeutic potential of AG490 has been demonstrated for experimental bone-defect in a mouse model [22]. Similarly to the latter research, we used JAK2 phosphorylation inhibitor AG490 to explore the role of JAK2/STAT3 in osteogenic differentiation of BMSCs. The results showed that phosphorylation of JAK2 and STAT3 decreased in BMSCs, and the osteogenic-differentiation ability of BMSCs also decreased. Our results suggest that inhibition of the JAK2/STAT3 pathway could inhibit the osteogenic differentiation of BMSCs.

SDF-1 is a low-molecular-weight chemokine protein, which is the most effective chemokine for bone marrow cells, and belongs to the CXC chemokine family [23]. SDF-1 is continuously secreted by stromal cells. CXCR4 is the only known receptor of SDF-1 that belongs to the G-protein-coupled receptor family. SDF-1 and CXCR4 constitute the SDF-1/CXCR4 axis, which transduces specific signals and mediates different effects [24]. It plays an important role in embryonic development, mediating immune and inflammatory responses, and regulating stem-cell migration and homing [25, 26]. CXCR4 is barely

expressed in normal tissues but increases in ischemia [27]. CXCR4 is expressed in BMSCs, and cytokines produced in result of tissue injury can stimulate CXCR4 to be transferred from within cells to the cell surface [28]. SDF-1 has a strong chemoattractant effect on CXCR4-expressing BMSCs since the specific binding of SDF-1 to CXCR4 is conducive to the directional chemotaxis of BMSCs [29]. In this study, we found that SDF-1 promotes the osteogenic differentiation of BMSCs.

As a specific inhibitor of CXCR4, AMD3100 has been widely used in basic research on CXCR4 pathway disorders. For example, in myeloma, AMD3100 blocks the interaction between multiple myeloma cells and the bone marrow microenvironment, and enhances multiple myeloma cells' sensitivity to treatment [30]. In this study, to verify the effect of SDF-1/CXCR4 regulating JAK2/STAT3 pathway in the osteogenic differentiation of BMSCs, we treated BMSCs with the JAK2 phosphorylation inhibitor AG490 and the CXCR4 specific inhibitor AMD3100. The results showed that AMD3100 treatment could reduce the phosphorylation levels of JAK2 and STAT3. The results further indicated that SDF-1/CXCR4 could signal through JAK2/ and STAT3 pathway.

In conclusion, our results suggest that SDF-1/CXCR4 activates JAK2/STAT3 to regulate the osteogenic differentiation of BMSCs; however, there are still some shortcomings in this study. Xiu *et al.* [31] confirmed that SDF-1/CXCR4 can promote the migration of BMSCs and enhance SDF-1/CXCR4 therapeutic effect of BMSCs in LPS-induced acute liver injury, which is caused by the activation of the PI3K/Akt signaling pathway. Therefore, it is important to study the effect of SDF-1/CXCR4 on other aspects of BMSCs function, including their migration. In addition, previous studies have confirmed that SDF-1/CXCR4 reduces adhesion-mediated chemoresistance of multiple myeloma cells by activating PI3K/Akt and upregulating interleukin-6 (IL-6) [32]. Therefore, the role of SDF-1/CXCR4 and other signaling pathways in BMSCs needs to be further explored.

Funding

None.

Authors' contribution

CXH: conceived and designed the experiments; WX: performed the experiments; XG: statistic analysis; WX: wrote the paper. All authors read and approved the final manuscript.

Data availability statement

The data used to support the findings of this study are available from the corresponding author upon request.

Competing interests

The authors declare that they have no competing interest.

References

1. Nishigaki A, Tsuzuki-Nakao T, Kido T, et al. Concentration of stromal cell-derived factor-1 (SDF-1/CXCL12) in the follicular fluid is associated with blastocyst development. *Reprod Med Biol.* 2019; 18(2): 161–166, doi: [10.1002/rmb2.12259](https://doi.org/10.1002/rmb2.12259), indexed in Pubmed: [30996679](https://pubmed.ncbi.nlm.nih.gov/30996679/).
2. Kawaguchi N, Zhang TT, Nakanishi T. Involvement of CXCR4 in normal and abnormal development. *Cells.* 2019; 8(2), doi: [10.3390/cells8020185](https://doi.org/10.3390/cells8020185), indexed in Pubmed: [30791675](https://pubmed.ncbi.nlm.nih.gov/30791675/).
3. Li G, An J, Han X, et al. Hypermethylation of microRNA-149 activates SDF-1/CXCR4 to promote osteogenic differentiation of mesenchymal stem cells. *J Cell Physiol.* 2019; 234(12): 23485–23494, doi: [10.1002/jcp.28917](https://doi.org/10.1002/jcp.28917), indexed in Pubmed: [31206187](https://pubmed.ncbi.nlm.nih.gov/31206187/).
4. Chen Q, Zheng C, Li Y, et al. Bone targeted delivery of SDF-1 via alendronate functionalized nanoparticles in guiding stem cell migration. *ACS Appl Mater Interfaces.* 2018; 10(28): 23700–23710, doi: [10.1021/acsami.8b08606](https://doi.org/10.1021/acsami.8b08606), indexed in Pubmed: [29939711](https://pubmed.ncbi.nlm.nih.gov/29939711/).
5. Li G, Yun X, Ye K, et al. Long non-coding RNA-H19 stimulates osteogenic differentiation of bone marrow mesenchymal stem cells via the microRNA-149/SDF-1 axis. *J Cell Mol Med.* 2020; 24(9): 4944–4955, doi: [10.1111/jcmm.15040](https://doi.org/10.1111/jcmm.15040), indexed in Pubmed: [32198976](https://pubmed.ncbi.nlm.nih.gov/32198976/).
6. Zhuang XM, Zhou B, Yuan KF. Role of p53 mediated miR-23a/CXCL12 pathway in osteogenic differentiation of bone mesenchymal stem cells on nanostructured titanium surfaces. *Biomed Pharmacother.* 2019; 112: 108649, doi: [10.1016/j.biopha.2019.108649](https://doi.org/10.1016/j.biopha.2019.108649), indexed in Pubmed: [30784930](https://pubmed.ncbi.nlm.nih.gov/30784930/).
7. Barzelay A, Weisthal Algor S, Niztan A, et al. Adipose-derived mesenchymal stem cells migrate and rescue rpe in the setting of oxidative stress. *Stem Cells Int.* 2018; 2018: 9682856, doi: [10.1155/2018/9682856](https://doi.org/10.1155/2018/9682856), indexed in Pubmed: [30651740](https://pubmed.ncbi.nlm.nih.gov/30651740/).
8. Herberg S, Fulzele S, Yang N, et al. Stromal cell-derived factor-1 β potentiates bone morphogenetic protein-2-stimulated osteoinduction of genetically engineered bone marrow-derived mesenchymal stem cells in vitro. *Tissue Eng Part A.* 2013; 19(1-2): 1–13, doi: [10.1089/ten.TEA.2012.0085](https://doi.org/10.1089/ten.TEA.2012.0085), indexed in Pubmed: [22779446](https://pubmed.ncbi.nlm.nih.gov/22779446/).
9. Periyasamy-Thandavan S, Burke J, Mendhe B, et al. MicroRNA-141-3p negatively modulates SDF-1 expression in age-dependent pathophysiology of human and murine bone marrow stromal cells. *J Gerontol A Biol Sci Med Sci.* 2019; 74(9): 1368–1374, doi: [10.1093/gerona/gly186](https://doi.org/10.1093/gerona/gly186), indexed in Pubmed: [31505568](https://pubmed.ncbi.nlm.nih.gov/31505568/).
10. Itoh S, Udagawa N, Takahashi N, et al. A critical role for interleukin-6 family-mediated Stat3 activation in osteoblast differentiation and bone formation. *Bone.* 2006; 39(3): 505–512, doi: [10.1016/j.bone.2006.02.074](https://doi.org/10.1016/j.bone.2006.02.074), indexed in Pubmed: [16679075](https://pubmed.ncbi.nlm.nih.gov/16679075/).
11. Yue R, Zhou BoO, Shimada IS, et al. Leptin receptor promotes adipogenesis and reduces osteogenesis by regulating

- mesenchymal stromal cells in adult bone marrow. *Cell Stem Cell*. 2016; 18(6): 782–796, doi: [10.1016/j.stem.2016.02.015](https://doi.org/10.1016/j.stem.2016.02.015), indexed in Pubmed: [27053299](https://pubmed.ncbi.nlm.nih.gov/27053299/).
12. Pajarinen J, Lin T, Gibon E, et al. Mesenchymal stem cell-macrophage crosstalk and bone healing. *Biomaterials*. 2019; 196: 80–89, doi: [10.1016/j.biomaterials.2017.12.025](https://doi.org/10.1016/j.biomaterials.2017.12.025), indexed in Pubmed: [29329642](https://pubmed.ncbi.nlm.nih.gov/29329642/).
 13. Yu X, Li Z, Wan Q, et al. Inhibition of JAK2/STAT3 signaling suppresses bone marrow stromal cells proliferation and osteogenic differentiation, and impairs bone defect healing. *Biol Chem*. 2018; 399(11): 1313–1323, doi: [10.1515/hsz-2018-0253](https://doi.org/10.1515/hsz-2018-0253), indexed in Pubmed: [30044759](https://pubmed.ncbi.nlm.nih.gov/30044759/).
 14. Han J, Feng Z, Xie Yu, et al. Oncostatin M-induced upregulation of SDF-1 improves bone marrow stromal cell migration in a rat middle cerebral artery occlusion stroke model. *Exp Neurol*. 2019; 313: 49–59, doi: [10.1016/j.expneurol.2018.09.005](https://doi.org/10.1016/j.expneurol.2018.09.005), indexed in Pubmed: [30213507](https://pubmed.ncbi.nlm.nih.gov/30213507/).
 15. Zhang P, Zhang H, Lin J, et al. Insulin impedes osteogenesis of BMSCs by inhibiting autophagy and promoting premature senescence via the TGF-1 pathway. *Aging (Albany NY)*. 2020; 12(3): 2084–2100, doi: [10.18632/aging.102723](https://doi.org/10.18632/aging.102723), indexed in Pubmed: [32017705](https://pubmed.ncbi.nlm.nih.gov/32017705/).
 16. Li X, Zheng Y, Hou L, et al. Exosomes derived from maxillary BMSCs enhanced the osteogenesis in iliac BMSCs. *Oral Dis*. 2020; 26(1): 131–144, doi: [10.1111/odi.13202](https://doi.org/10.1111/odi.13202), indexed in Pubmed: [31541596](https://pubmed.ncbi.nlm.nih.gov/31541596/).
 17. Onodera K, Sakurada A, Notsuda H, et al. Growth inhibition of KRAS and EGFR mutant lung adenocarcinoma by cosuppression of STAT3 and the SRC/ARHGAP35 axis. *Oncol Rep*. 2018; 40(3): 1761–1768, doi: [10.3892/or.2018.6536](https://doi.org/10.3892/or.2018.6536), indexed in Pubmed: [30015929](https://pubmed.ncbi.nlm.nih.gov/30015929/).
 18. Park SY, Lee CJ, Choi JH, et al. The JAK2/STAT3/CCND2 Axis promotes colorectal cancer stem cell persistence and radioresistance. *J Exp Clin Cancer Res*. 2019; 38(1): 399, doi: [10.1186/s13046-019-1405-7](https://doi.org/10.1186/s13046-019-1405-7), indexed in Pubmed: [31511084](https://pubmed.ncbi.nlm.nih.gov/31511084/).
 19. Hubbard SR. Mechanistic insights into regulation of JAK2 tyrosine kinase. *Front Endocrinol (Lausanne)*. 2017; 8: 361, doi: [10.3389/fendo.2017.00361](https://doi.org/10.3389/fendo.2017.00361), indexed in Pubmed: [29379470](https://pubmed.ncbi.nlm.nih.gov/29379470/).
 20. Liu H, Du T, Li C, et al. STAT3 phosphorylation in central leptin resistance. *Nutr Metab (Lond)*. 2021; 18(1): 39, doi: [10.1186/s12986-021-00569-w](https://doi.org/10.1186/s12986-021-00569-w), indexed in Pubmed: [33849593](https://pubmed.ncbi.nlm.nih.gov/33849593/).
 21. Chen XM, Yu YH, Wang L, et al. Effect of the JAK2/STAT3 signaling pathway on nerve cell apoptosis in rats with white matter injury. *Eur Rev Med Pharmacol Sci*. 2019; 23(1): 321–327, doi: [10.26355/eurrev_201901_16779](https://doi.org/10.26355/eurrev_201901_16779), indexed in Pubmed: [30657573](https://pubmed.ncbi.nlm.nih.gov/30657573/).
 22. Yu X, Wan QL, Li Z, et al. [(*)AG490 could suppress bone marrow mesenchymal stem cells migration, mineralization and bone defect healing via inhibiting Jak2-STAT3 pathway]. *Zhonghua Kou Qiang Yi Xue Za Zhi*. 2018; 53(5): 293–300, doi: [10.3760/cma.j.issn.1002-0098.2018.05.002](https://doi.org/10.3760/cma.j.issn.1002-0098.2018.05.002), indexed in Pubmed: [29972985](https://pubmed.ncbi.nlm.nih.gov/29972985/).
 23. Teicher BA, Fricker SP. CXCL12 (SDF-1)/CXCR4 pathway in cancer. *Clin Cancer Res*. 2010; 16(11): 2927–2931, doi: [10.1158/1078-0432.CCR-09-2329](https://doi.org/10.1158/1078-0432.CCR-09-2329), indexed in Pubmed: [20484021](https://pubmed.ncbi.nlm.nih.gov/20484021/).
 24. Mousavi A. CXCL12/CXCR4 signal transduction in diseases and its molecular approaches in targeted-therapy. *Immunol Lett*. 2020; 217: 91–115, doi: [10.1016/j.imlet.2019.11.007](https://doi.org/10.1016/j.imlet.2019.11.007), indexed in Pubmed: [31747563](https://pubmed.ncbi.nlm.nih.gov/31747563/).
 25. Ding Qi, Sun J, Xie W, et al. Stemona alkaloids suppress the positive feedback loop between M2 polarization and fibroblast differentiation by inhibiting JAK2/STAT3 pathway in fibroblasts and CXCR4/PIK/AKT1 pathway in macrophages. *Int Immunopharmacol*. 2019; 72: 385–394, doi: [10.1016/j.intimp.2019.04.030](https://doi.org/10.1016/j.intimp.2019.04.030), indexed in Pubmed: [31030094](https://pubmed.ncbi.nlm.nih.gov/31030094/).
 26. Dimova I, Karthik S, Makanya A, et al. SDF-1/CXCR4 signalling is involved in blood vessel growth and remodelling by intussusception. *J Cell Mol Med*. 2019; 23(6): 3916–3926, doi: [10.1111/jcmm.14269](https://doi.org/10.1111/jcmm.14269), indexed in Pubmed: [30950188](https://pubmed.ncbi.nlm.nih.gov/30950188/).
 27. Ge G, Zhang H, Li R, et al. The function of SDF-1-CXCR4 axis in SP cells-mediated protective role for renal ischemia/reperfusion injury by SHH/GLI1-ABCG2 pathway. *Shock*. 2017; 47(2): 251–259, doi: [10.1097/SHK.0000000000000694](https://doi.org/10.1097/SHK.0000000000000694), indexed in Pubmed: [27454381](https://pubmed.ncbi.nlm.nih.gov/27454381/).
 28. Wang G, Zhuo Z, Zhang Q, et al. Transfection of CXCR-4 using microbubble-mediated ultrasound irradiation and liposomes improves the migratory ability of bone marrow stromal cells. *Curr Gene Ther*. 2015; 15(1): 21–31, doi: [10.2174/15665232146666141121111220](https://doi.org/10.2174/15665232146666141121111220), indexed in Pubmed: [25414029](https://pubmed.ncbi.nlm.nih.gov/25414029/).
 29. Jaerve A, Schira J, Müller HW. Concise review: the potential of stromal cell-derived factor 1 and its receptors to promote stem cell functions in spinal cord repair. *Stem Cells Transl Med*. 2012; 1(10): 732–739, doi: [10.5966/sctm.2012-0068](https://doi.org/10.5966/sctm.2012-0068), indexed in Pubmed: [23197665](https://pubmed.ncbi.nlm.nih.gov/23197665/).
 30. Azab AK, Runnels JM, Pitsillides C, et al. CXCR4 inhibitor AMD3100 disrupts the interaction of multiple myeloma cells with the bone marrow microenvironment and enhances their sensitivity to therapy. *Blood*. 2009; 113(18): 4341–4351, doi: [10.1182/blood-2008-10-186668](https://doi.org/10.1182/blood-2008-10-186668), indexed in Pubmed: [19139079](https://pubmed.ncbi.nlm.nih.gov/19139079/).
 31. Xiu G, Li X, Yin Y, et al. SDF-1/CXCR4 augments the therapeutic effect of bone marrow mesenchymal stem cells in the treatment of lipopolysaccharide-induced liver injury by promoting their migration through PI3K/Akt signaling pathway. *Cell Transplant*. 2020; 29: 963689720929992, doi: [10.1177/0963689720929992](https://doi.org/10.1177/0963689720929992), indexed in Pubmed: [32452221](https://pubmed.ncbi.nlm.nih.gov/32452221/).
 32. Liu Y, Liang HM, Lv YQ, et al. Blockade of SDF-1/CXCR4 reduces adhesion-mediated chemoresistance of multiple myeloma cells via interacting with interleukin-6. *J Cell Physiol*. 2019; 234(11): 19702–19714, doi: [10.1002/jcp.28570](https://doi.org/10.1002/jcp.28570), indexed in Pubmed: [30953364](https://pubmed.ncbi.nlm.nih.gov/30953364/).

Submitted: 18 May, 2021

Accepted after reviews: 24 September, 2021

Available as AoP: 27 September, 2021

IL-39 increases ROS production and promotes the phosphorylation of p38 MAPK in the apoptotic cardiomyocytes

Wei Xiong¹, Hua Chen², Jiequan Lu³, Jie Ren³, Chen Nie¹, Ruijuan Liang³, Feng Liu³, Baofeng Huang⁴, Yu Luo⁴

¹Department of Emergency, Shenzhen People's Hospital Longhua Branch, The Second Affiliated Hospital of Jinan Medical College, Shenzhen, China

²Department of Emergency, Shenzhen People's Hospital, The Second Affiliated Hospital of Jinan Medical College, Shenzhen, China

³Department of Cardiology, Shenzhen People's Hospital, The Second Affiliated Hospital of Jinan Medical College, Shenzhen, China

⁴Department of Gerontology, Shenzhen People's Hospital, The Second Affiliated Hospital of Jinan Medical College, Shenzhen, China

Abstract

Introduction. The cytokine interleukin (IL)-39 is a novel member of the IL-12 family. Our previous study found that the serum level of IL-39 significantly increased in patients with acute myocardial infarction. However, the role of IL-39 in cardiomyocyte apoptosis remains unclear.

Material and methods. In this study, the cultured mouse HL-1 cardiomyocytes were incubated with PBS, 0–100 ng/mL IL-39, 200 μ M H₂O₂ or 20 μ M Trolox.

Results. IL-39 promoted the production of intracellular reactive oxygen species (ROS) in a concentration-dependent manner in HL-1 cardiomyocytes. IL-39 and H₂O₂ both significantly promoted the production of intracellular ROS, increased the level of intracellular CCL2, stimulated the apoptotic progress of cardiomyocytes, increased the mRNA and protein expression levels of Bax, caspase-3, and p-p38 MAPK, and decreased the mRNA and protein expression levels of Bcl-2. ROS production, CCL2 level, cardiomyocyte apoptosis, and expression of Bax, caspase-3, and p-p38 MAPK were significantly amplified by the administration of IL-39 combined with H₂O₂, and these processes were significantly alleviated by an antioxidant Trolox.

Conclusion. This study was novel in revealing that IL-39 promoted apoptosis by stimulating the phosphorylation of p38 MAPK in mouse HL-1 cardiomyocytes. (*Folia Histochemica et Cytobiologica* 2021, Vol. 59, No. 3, 195–202)

Key words: apoptosis; HL-1 cardiomyocyte; interleukin-39; p38 MAPK; ROS

Introduction

Acute myocardial infarction is the most common cause of mortality and morbidity worldwide [1]. Rep-

erfusion therapy is the most effective procedure to save ischemic cardiomyocytes and limit infarct size [2]. However, the restoration of blood flow may aggravate the injury to the original ischemic myocardium, which is defined as myocardial ischemia–reperfusion injury (MIRI) and lead to myocardial stunning, hemodynamic abnormalities, ventricular arrhythmia, and development of heart failure [3]. The sophisticated pathophysiological process of MIRI needs to be clarified and methods need to be developed to improve the prognosis of these patients [4].

Correspondence address: Luo Yu,
Department of Gerontology, Shenzhen People's Hospital,
The Second Affiliated Hospital of Jinan Medical College,
Shenzhen 518020, China
e-mail: xly9926@126.com

This article is available in open access under Creative Common Attribution-Non-Commercial-No Derivatives 4.0 International (CC BY-NC-ND 4.0) license, allowing to download articles and share them with others as long as they credit the authors and the publisher, but without permission to change them in any way or use them commercially.

The MIRI process involves excess reactive oxygen species (ROS) production, neutrophil aggregation, intracellular calcium overload, and mitochondrial dysfunction [5, 6]. The activation of immune system, including innate immunity and adaptive immunity, was found to be closely associated with MIRI [7, 8]. The members of the interleukin-12 (IL-12) family are critical cytokines mediating the inflammatory process and playing a critical role in immune responses [9]. As a novel member of the IL-12 family, IL-39 was recently reported to enhance inflammatory response through activating signal transducer and activator of transcription in lupus-like mice [10]. However, the relationship between IL-39 and MIRI has not been investigated yet.

The fate of cardiomyocytes in infarcted myocardium is either cellular necrosis or apoptosis. Cardiomyocyte apoptosis is the most common in ischemic regions close to the infarcted myocardium [11]. Our previous study found that the serum level of IL-39 significantly increased in patients with acute ST-segment elevation myocardial infarction (STEMI) and was related to left ventricular systolic dysfunction [12]. IL-17 and IL-23 contribute to cardiomyocyte apoptosis and MIRI [13, 14]; however, the role of IL-39 is worth investigating. This study examined the relationship between IL-39 and cardiomyocyte apoptosis in an *in vitro* model to better understand the role of IL-39 in cardiovascular diseases.

Materials and methods

Cell culture. The mouse HL-1 cardiomyocyte line obtained from Enzyme Research Biotech INC (China) was cultured in DMEM (Gibco, USA) with 10% FBS (Gibco), penicillin (100 unit/mL), and streptomycin (100 μ g/mL) in the humidified incubator in the atmosphere of 5% CO₂ at 37°C. The cells between passages 3 and 5 were employed for experiments. The cells seeded at a density of 5×10^4 cells/well were cultured for 24 h and subsequently treated with phosphate-buffered saline (PBS, vehicle), 0–100 ng/mL IL-39 (R&D, USA), 200 μ M H₂O₂ (Sigma–Aldrich, Germany), 60 ng/mL IL-39 combined with 200 μ M H₂O₂, and 20 μ M Trolox (Solarbio, China) for 24 h.

Intracellular ROS detection. A dichlorodihydrofluorescein diacetate (DCFH-DA) ROS assay kit (Beyotime Biotechnology, China) was employed to investigate intracellular ROS production in HL-1 cardiomyocytes following the manufacturer's protocol. In brief, the medium was discarded 24 h after the cells were cultured and treated using the method described previously. Then, 1.5 mL of DCFH-DA (10 μ M) solution was added, and the cells were subsequently incubated for 30 min at 37°C in the presence of 5% CO₂. The intracellular fluorescence intensities were detected at 488 and 525 nm under a fluorescence microscope (Olympus, Japan).

Enzyme-linked immunosorbent assay. HL-1 cardiomyocytes were cultured and treated with PBS, IL-39, H₂O₂, and/or Trolox. The supernatants of cultured cells were harvested and centrifuged at 2000 rpm for 20 min at 4°C 24 h after the treatment. The level of chemokine C-C motif ligand 2 (CCL2) was measured using an enzyme-linked immunosorbent assay (ELISA) kit (J&L Biotech, China) following the manufacturer's protocol.

Apoptosis assay. The apoptosis of HL-1 cardiomyocytes was analyzed by flow cytometry using a Dead Cell Apoptosis Kit with Annexin V Alexa Fluor 488 and PI (Thermo Fisher, USA). Briefly, the cells were collected and resuspended in 500 μ L of binding buffer, and 1 μ L of Annexin V and 5 μ L of PI were successively added to stain the cells 24 h after the treatment. The samples were determined using flow cytometry (BD Biosciences, USA). The percentage of apoptotic cells were calculated which represented Annexin V positive/ PI positive cells.

Quantitative real-time PCR. Total RNAs were isolated after the cells were treated for 24 h using an RNeasy Mini Kit (Qiagen, Germany) and reversed to cDNA using a One-Step PrimeScript miRNA cDNA Synthesis Kit (TaKaRa, Japan) to quantify target genes in HL-1 cardiomyocytes. Quantitative PCR of Bcl-2, Bax, caspase-3, and phosphorylated-p38 mitogen-activated protein kinase (p-p38 MAPK) were performed using an ABI 7500 Fast Real-Time PCR System (Applied Biosystems, USA) with an SYBR Premix Ex Taq kit (TaKaRa). U6 was used as an internal control. All primers were synthesized by Sangon (China). The relative expression of target genes was calculated using the following equation: Relative expression level = $2^{-(\Delta C_t \text{ sample} - \Delta C_t \text{ control})}$.

Western blot analysis. For Western blot analysis, 20 μ g of total protein extracted from the HL-1 cardiomyocytes after the cells were treated for 24 h was resolved on 10% SDS-polyacrylamide gels and electrotransferred onto nitrocellulose membranes. The membranes were blocked with 5% nonfat milk in TBS containing 0.3% Tween-20 and then incubated overnight with polyclonal rabbit anti-mouse antibodies against Bcl-2 (1:1000 dilution, Abcam, USA), Bax (1:500 dilution, Abcam), caspase-3 (1:1000 dilution, Cell Signaling, USA), and p-p38 MAPK (1:1000 dilution, Cell Signaling). The polyclonal rabbit anti-mouse GAPDH antibody (1:1000 dilution, Abcam) served as control. The goat anti-rabbit horseradish peroxidase-conjugated secondary antibody was subsequently added. ECL was administered to detect protein signals using Quant RT ECL cold CCD imaging system (General Electric, USA).

Statistical analysis. The statistical analyses were carried out using SPSS 16.0 (SPSS Inc, USA). Data were presented as mean \pm standard deviation. The mean value in the vehicle group was defined as 100% for relative gene expression.

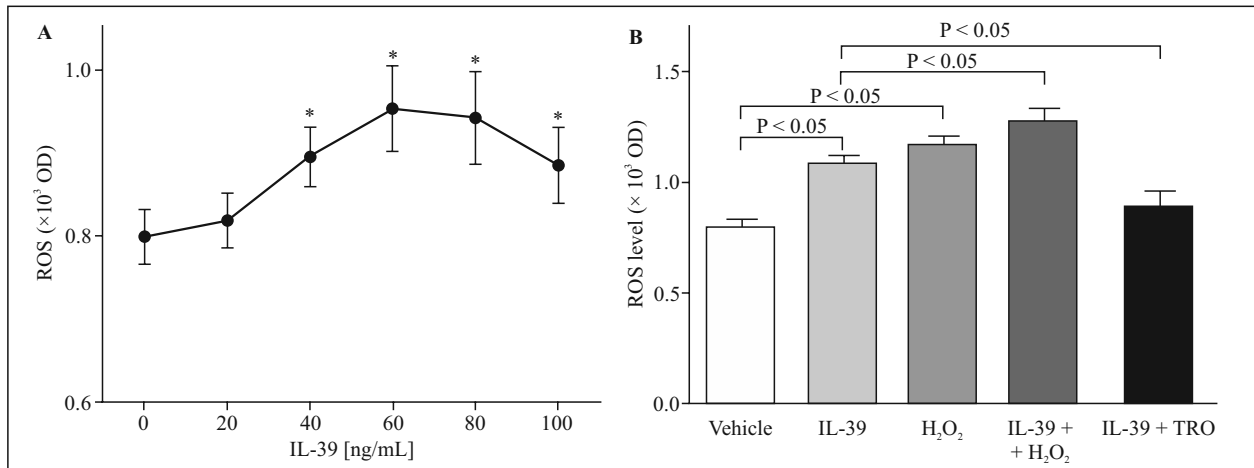


Figure 1. IL-39 promoted ROS production in HL-1 cardiomyocytes. **A.** IL-39 promoted ROS production in a concentration-dependent manner ($n = 6$); $P < 0.05$ vs. 0 ng/mL IL-39. **B.** IL-39 and H₂O₂ increased the ROS level in HL-1 cardiomyocytes ($n = 6$). ROS levels were determined as described in Methods section.

Overall data were compared using analysis of variance and *post-hoc* least significant difference statistics. A P value of less than 0.05 indicated a statistically significant difference.

Results

IL-39 promoted ROS production in HL-1 cardiomyocytes

Different concentrations of IL-39 were added to cultures of HL-1 cardiomyocytes to identify the relationship between ROS production and IL-39 levels. As shown in Figure 1A, IL-39 promoted ROS production in a concentration-dependent manner; the highest level of ROS production was induced by IL-39 at a concentration of 60 ng/mL (vs. 0 ng/mL IL-39, $P < 0.05$). Both 60 ng/mL IL-39 and 200 μ M H₂O₂ promoted ROS production in HL-1 cardiomyocytes (vs. vehicle, $P < 0.05$). The elevation of ROS production induced by 60 ng/mL IL-39 alone was amplified by the stimulation of IL-39 60 ng/mL combined with 200 μ M H₂O₂ (IL-39 + H₂O₂ vs. IL-39, $P < 0.05$), but was decreased by the antioxidant 20 μ M Trolox (IL-39 + TRO vs. IL-39, $P < 0.05$) (Fig. 1B).

IL-39 increased the level of CCL2 in HL-1 cardiomyocytes

The chemokine CCL2 levels in HL-1 cardiomyocytes were investigated using ELISA. Both IL-39 and oxidative stress significantly increased the level of CCL2 (vs. vehicle, $P < 0.05$). The elevation of CCL2 level in HL-1 cardiomyocytes induced by 60 ng/mL IL-39 alone was amplified by the addition of 200 μ M H₂O₂ (IL-39 + H₂O₂ vs. IL-39, $P < 0.05$), however, it was significantly decreased by 20 μ M Trolox (IL-39 + TRO vs. IL-39, $P < 0.05$) (Fig. 2).

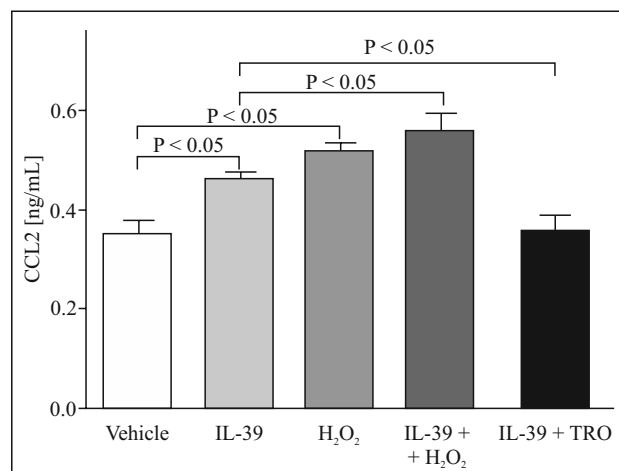


Figure 2. IL-39 increased the level of CCL2 chemokine in HL-1 cardiomyocytes incubated with IL-39 (60 ng/mL), 200 μ M H₂O₂ or IL-39 at 60 ng/mL and 20 μ M Trolox ($n = 6$). CCL2 concentration was determined by ELISA as described in Methods section.

IL-39 stimulates the apoptosis of HL-1 cardiomyocytes

Flow cytometry was used to evaluate the apoptosis of HL-1 cardiomyocytes, the real-time PCR and Western blot analyses were used to examine the mRNA and protein levels of Bcl-2, Bax and caspase-3. Both 60 ng/mL IL-39 and 200 μ M H₂O₂ induced significant apoptosis in HL-1 cells (vs. vehicle, $P < 0.05$). IL-39 demonstrated a more potent ability to promote HL-1 cardiomyocyte apoptosis (IL-39 vs. vehicle, $P < 0.01$). The apoptosis of HL-1 cardiomyocytes induced by 60 ng/mL IL-39 alone was amplified by 200 μ M H₂O₂ (IL-39 + H₂O₂ vs. IL-39, $P < 0.05$), and was

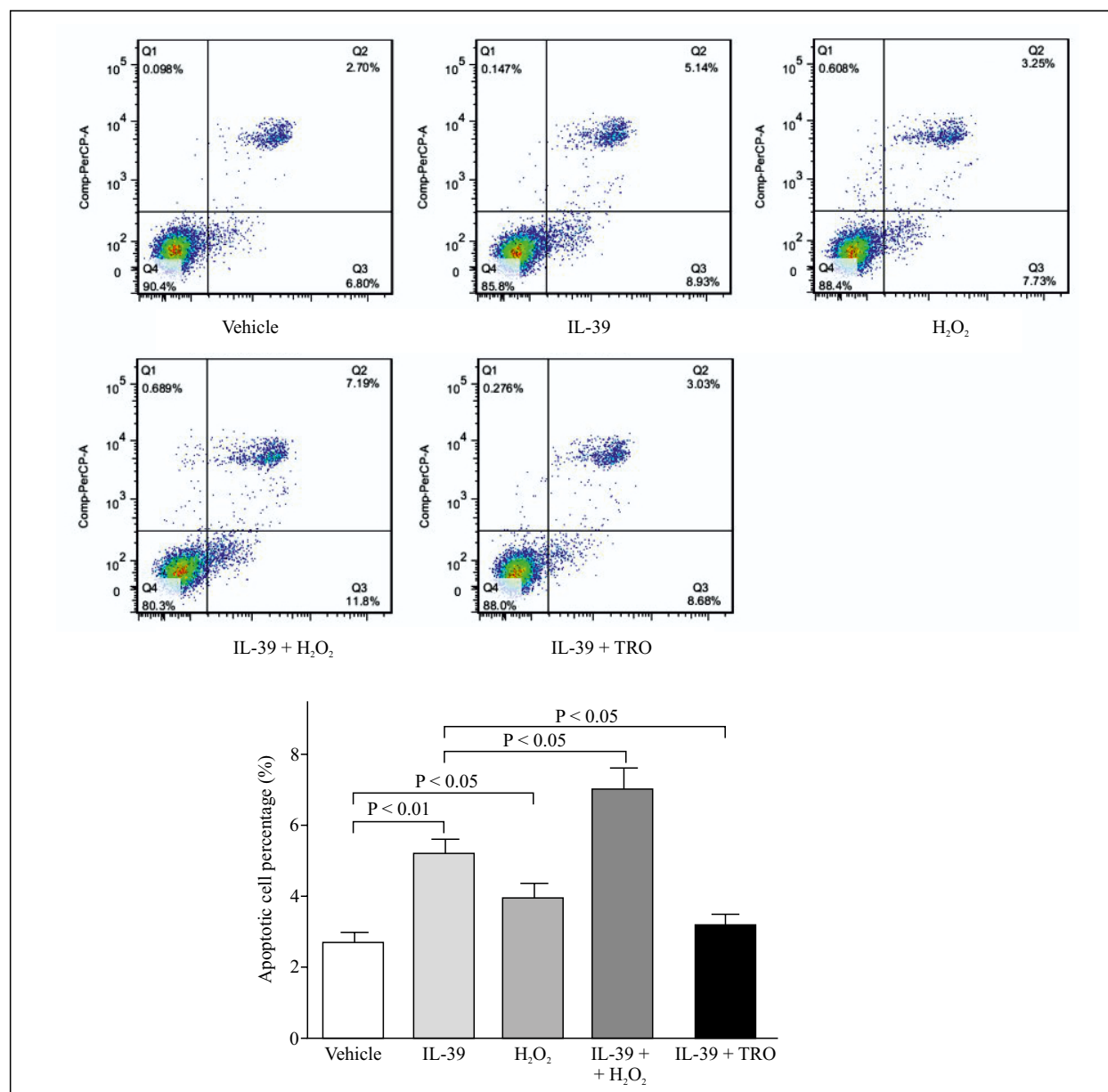


Figure 3. IL-39 promoted the apoptosis of HL-1 cardiomyocytes ($n = 6$). The concentrations of IL-39, H₂O₂, and Trolox were as in the description of Figure 2. Apoptosis was determined by flow cytometry as described in Methods section.

significantly alleviated by 20 μ M Trolox (IL-39 + TRO vs. IL-39, $P < 0.05$) (Fig. 3). The transcription level of Bcl-2 was significantly decreased by 60 ng/mL IL-39 and 200 μ M H₂O₂ (vs. vehicle, $P < 0.05$). The decreased transcription level of Bcl-2 in HL-1 cardiomyocytes induced by 60 ng/mL IL-39 alone was amplified by 200 μ M H₂O₂ (IL-39 + H₂O₂ vs. IL-39, $P < 0.01$), and was significantly alleviated by 20 μ M Trolox (IL-39 + TRO vs. IL-39, $P < 0.05$) (Fig. 4A and 4B). The transcription levels of Bax and caspase-3 were significantly elevated by 60 ng/mL IL-39 and 200 μ M H₂O₂ (vs. vehicle, $P < 0.05$). The increased transcription levels of Bax and caspase-3

in HL-1 cardiomyocytes induced by 60 ng/mL IL-39 alone were amplified by 200 μ M H₂O₂ (IL-39 + H₂O₂ vs. IL-39, $P < 0.05$), and were significantly alleviated by 20 μ M Trolox (IL-39 + TRO vs. IL-39, $P < 0.05$) (Fig. 4A, 4C, 4D).

IL-39 stimulates the phosphorylation of p38 MAPK in the apoptotic cardiomyocytes

To identify the potential molecular mechanism of IL-39 regulating the apoptosis of HL-1 cardiomyocytes, the mRNA and protein levels of phosphorylated p38 MAPK were examined using real-time PCR and Western blot analysis, respectively. As shown in

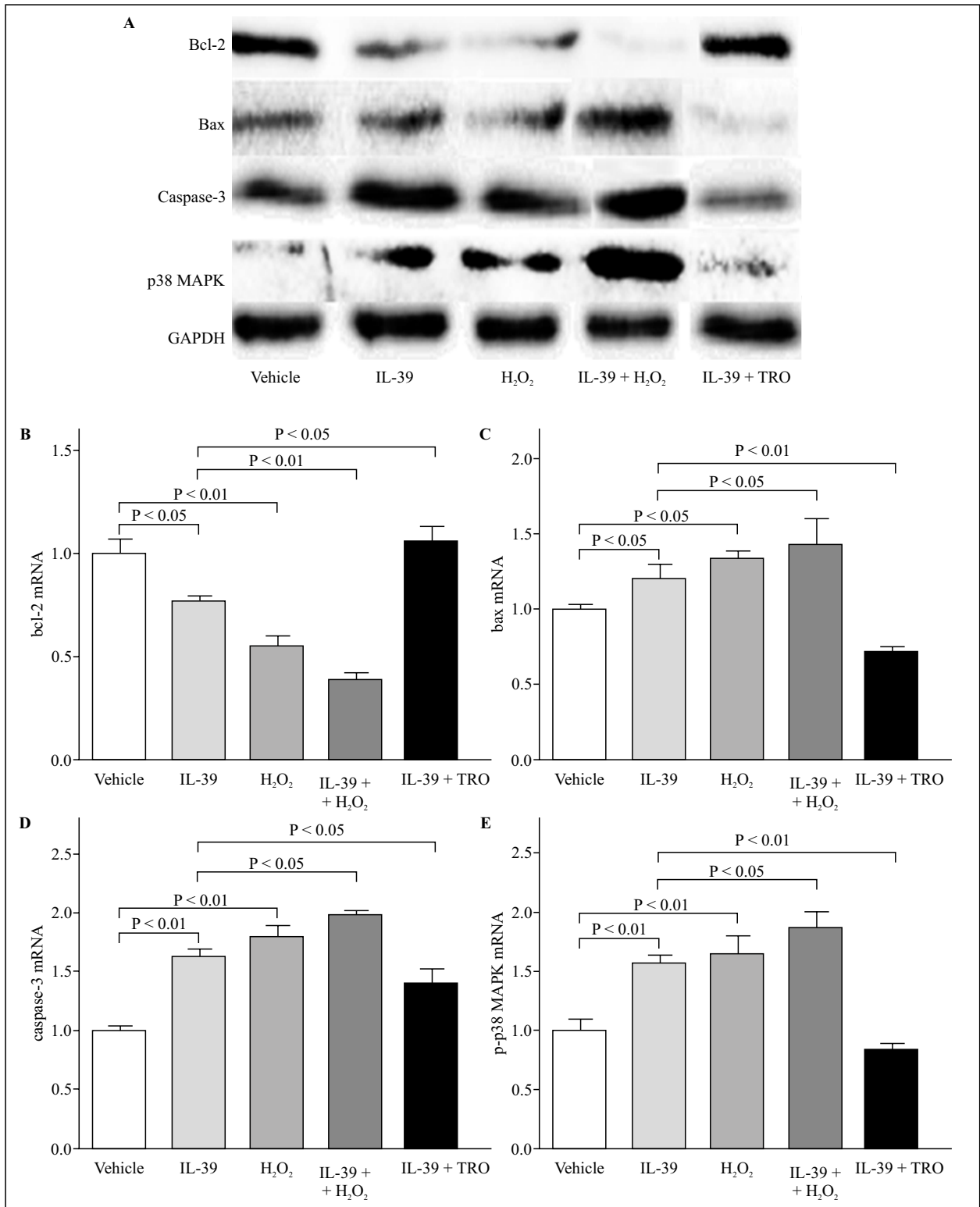


Figure 4. IL-39 promoted the expression of *p*-p38 MAPK in HL-1 cardiomyocytes. **A.** Protein levels in HL-1 cardiomyocytes were identified using Western blot analysis ($n = 3$). **B.** IL-39 significantly decreased the transcription level of Bcl-2 in HL-1 cardiomyocytes ($n = 6$). **C.** IL-39 significantly increased the transcription level of Bax in HL-1 cardiomyocytes ($n = 6$). **D.** IL-39 significantly increased the transcription level of caspase-3 in HL-1 cardiomyocytes ($n = 6$). **E.** IL-39 significantly increased the phosphorylation level of p38 MAPK in HL-1 cardiomyocytes ($n = 6$). The concentrations of IL-30, H₂O₂, and Trolox were as in the description of Figure 2.

Figure 4A and 4E, the transcription level of *p*-p38 MAPK was significantly elevated by 60 ng/mL IL-39 and 200 μ M H₂O₂ (vs. vehicle, $P < 0.05$). The increased transcription level of *p*-p38 MAPK in HL-1 cardiomyocytes induced by 60 ng/mL IL-39 alone was amplified by 200 μ M H₂O₂ (IL-39 + H₂O₂ vs. IL-39, $P < 0.05$), and was significantly alleviated by 20 μ M Trolox (IL-39 + TRO vs. IL-39, $P < 0.05$).

Discussion

In the previous study [12], we found that the serum level of IL-39 in patients with STEMI significantly increased, indicating that IL-39 might be involved in the process of myocardial injury and remodeling. The present study showed that IL-39 promoted ROS production, CCL2 secretion, and cardiomyocyte apoptosis; the underlying mechanism was related to the increased expression of *p*-p38 MAPK.

The MIRI is mediated by several factors including excessive ROS production. The increased accumulation of ROS in cardiomyocytes results in oxidative stress, mitochondrial dysfunction, and subsequent cell death [5]. Antioxidant therapies hold great potential in attenuating cardiac injury induced by ischemia-reperfusion [15]. The data revealed that IL-39 promoted ROS production in a concentration-dependent manner, highlighting its association with MIRI.

Inflammation response is the major pathological feature in cardiac repair after acute myocardial infarction [16]. Chemokines play a critical role in the acute phase of myocardial infarction. CCL2 plays crucial roles in recruiting inflammatory cells and contributes to cardiac remodeling after myocardial infarction [17–19]. The level of CCL2 was also elevated in cardiomyocytes incubated with IL-37 and patients with acute coronary syndrome; hence, CCL2 can be treated as a biomarker and a potential target for therapy [20–22]. The results showed that IL-39 significantly increased the CCL2 level in HL-1 cardiomyocytes. Interestingly, CCL2 protected mouse neonatal cardiac myocytes from hypoxia-induced apoptosis [23]. However, the role of CCL2 in cardiomyocyte apoptosis was not investigated in the present study. Hence, how IL-39 increased the CCL2 level and their association in cardiomyocyte apoptosis deserve further investigation.

Cellular apoptosis is initiated by the activation of cell-surface receptors (the extrinsic pathway) or by the alteration of mitochondria permeability (the intrinsic pathway) [24]. Accumulating evidence indicated the critical role of the Bcl-2 family in determining the cell death process through the extrinsic pathway. The Bcl-2 family comprises two classes of

regulatory proteins: pro-apoptotic members (Bak and Bax) and anti-apoptotic members (Bcl-2 and Bcl-xL) [25, 26]. At the intersection of the intrinsic pathway and the extrinsic pathway, caspase-3 is ultimately stimulated by pro-apoptotic signals and the apoptosis process is completed in the nucleus [27]. IL-39 significantly stimulated the apoptosis of HL-1 cardiomyocytes *in vitro* in this study; the ability to induce apoptosis was more potent than that of H₂O₂. The evidence that decreased the expression of Bcl-2 and increased the expression of Bax and caspase-3 supported the opinion that IL-39 promoted cardiomyocyte apoptosis through the extrinsic pathway.

MAPK families play important roles in a wide variety of cellular programs, including cell growth, proliferation, differentiation, and apoptosis [28, 29]. Characterized as a member of MAPK families, p38 MAPK is activated to balance cell survival and death in response to both extracellular and intracellular stresses [30]. Also, p38 MAPK regulated the phosphorylation of Bcl-2 in the early induction of apoptosis under cellular stress [31]. The cardiomyocyte apoptosis induced by hypoxia/reoxygenation was mediated by the ROS-activated MAPK pathway and inhibited by the p38 MAPK inhibitor [32]. The inhibition of p38 MAPK reduced cardiac injury and improved cardiac function after acute myocardial infarction, indicating its critical role in cardiac remodeling [33–35]. In mice with lupus-like phenotype, IL-39 promoted inflammatory response through the STAT1/STAT3 signaling pathway (10). The present study found that IL-39-induced cardiomyocyte apoptosis involved the elevated expression of *p*-p38 MAPK. However, the upstream and downstream proteins of p38 MAPK were not explored in the present study. Whether p38 MAPK signaling plays a crucial role in IL-39-induced cardiomyocyte apoptosis is unclear. The role and function of IL-39 in physiological and pathological statuses still remain controversial [36] and require further investigation.

In conclusion, this study was novel in demonstrating that IL-39 promoted ROS production and stimulated the phosphorylation of p38 MAPK. Further studies should be accomplished to better understand the role of IL-39 and the molecular mechanism in the pathophysiological process of cardiovascular diseases and its prospects as a therapeutic target.

Acknowledgments

We thank International Science Editing (<http://www.international-scienceediting.com>) for editing this manuscript.

Funding

This study was funded by the Medical Scientific Research Foundation of Guangdong (A2018092, A2018530, A2019406) and the Incubation Foundation of Shenzhen People's Hospital (SYKYPY201905).

Authors' contributions

WX and YL conceived the study. JL, JR, CN, and RL performed the experiments. FL and BH analyzed the data. WX drafted the manuscript. WX, HC, and YL revised the manuscript. All authors read and approved the final manuscript.

Availability of data and materials

All data generated or analyzed in this study are included in this manuscript.

Ethics approval and consent to participate

Not applicable.

Patient consent for publication

Not applicable.

Conflicts of interest

The authors declare no conflicts of interest.

References

- Herrett E, Bhaskaran K, Timmis A, et al. Association between clinical presentations before myocardial infarction and coronary mortality: a prospective population-based study using linked electronic records. *Eur Heart J*. 2014;35(35):2363–2371, doi: [1093/eurheartj/ehu286](https://doi.org/10.1093/eurheartj/ehu286), indexed in Pubmed: [25038774](https://pubmed.ncbi.nlm.nih.gov/25038774/).
- van Do, Sonnenschein K, Nieuwlaet R, et al. Sustained benefit 20 years after reperfusion therapy in acute myocardial infarction. *J Am Coll Cardiol*. 2005;46(1):15–20, doi: [10.1016/j.jacc.2005.03.047](https://doi.org/10.1016/j.jacc.2005.03.047), indexed in Pubmed: [15992629](https://pubmed.ncbi.nlm.nih.gov/15992629/).
- Hausenloy DJ, Botker HE, Engstrom T, et al. Targeting reperfusion injury in patients with ST-segment elevation myocardial infarction: trials and tribulations. *Eur Heart J*. 2017; 38(13): 935–941, doi: [10.1093/eurheartj/ehw145](https://doi.org/10.1093/eurheartj/ehw145), indexed in Pubmed: [27118196](https://pubmed.ncbi.nlm.nih.gov/27118196/).
- Heusch G, Gersh BJ. The pathophysiology of acute myocardial infarction and strategies of protection beyond reperfusion: a continual challenge. *Eur Heart J*. 2017; 38(11): 774–784, doi: [10.1093/eurheartj/ehw224](https://doi.org/10.1093/eurheartj/ehw224), indexed in Pubmed: [27354052](https://pubmed.ncbi.nlm.nih.gov/27354052/).
- Ferdinandy P, Schulz R, Baxter GF. Interaction of cardiovascular risk factors with myocardial ischemia/reperfusion injury, preconditioning, and postconditioning. *Pharmacol Rev*. 2007; 59(4): 418–458, doi: [10.1124/pr.107.06002](https://doi.org/10.1124/pr.107.06002), indexed in Pubmed: [18048761](https://pubmed.ncbi.nlm.nih.gov/18048761/).
- Davidson SM, Ferdinandy P, Andreadou I, et al. CARDIOPROTECTION COST Action (CA16225). Multitarget Strategies to Reduce Myocardial Ischemia/Reperfusion Injury: JACC Review Topic of the Week. *J Am Coll Cardiol*. 2019; 73(1): 89–99, doi: [10.1016/j.jacc.2018.09.086](https://doi.org/10.1016/j.jacc.2018.09.086), indexed in Pubmed: [30621955](https://pubmed.ncbi.nlm.nih.gov/30621955/).
- Lin Li, Knowlton AA. Innate immunity and cardiomyocytes in ischemic heart disease. *Life Sci*. 2014; 100(1): 1–8, doi: [10.1016/j.lfs.2014.01.062](https://doi.org/10.1016/j.lfs.2014.01.062), indexed in Pubmed: [24486305](https://pubmed.ncbi.nlm.nih.gov/24486305/).
- Boag SE, Andreano E, Spyridopoulos I. Lymphocyte Communication in Myocardial Ischemia/Reperfusion Injury. *Antioxid Redox Signal*. 2017; 26(12): 660–675, doi: [10.1089/ars.2016.6940](https://doi.org/10.1089/ars.2016.6940), indexed in Pubmed: [28006953](https://pubmed.ncbi.nlm.nih.gov/28006953/).
- Vignali DAA, Kuchroo VK. IL-12 family cytokines: immunological playmakers. *Nat Immunol*. 2012; 13(8): 722–728, doi: [10.1038/ni.2366](https://doi.org/10.1038/ni.2366), indexed in Pubmed: [22814351](https://pubmed.ncbi.nlm.nih.gov/22814351/).
- Wang X, Wei Y, Xiao He, et al. A novel IL-23p19/Ebi3 (IL-39) cytokine mediates inflammation in Lupus-like mice. *Eur J Immunol*. 2016; 46(6): 1343–1350, doi: [10.1002/eji.201546095](https://doi.org/10.1002/eji.201546095), indexed in Pubmed: [27019190](https://pubmed.ncbi.nlm.nih.gov/27019190/).
- Takemura G, Fujiwara H. Role of apoptosis in remodeling after myocardial infarction. *Pharmacol Ther*. 2004; 104(1): 1–16, doi: [10.1016/j.pharmthera.2004.07.005](https://doi.org/10.1016/j.pharmthera.2004.07.005), indexed in Pubmed: [15500905](https://pubmed.ncbi.nlm.nih.gov/15500905/).
- Luo Yu, Liu F, Liu H, et al. Elevated serum IL-39 in patients with ST-segment elevation myocardial infarction was related with left ventricular systolic dysfunction. *Biomark Med*. 2017; 11(6): 419–426, doi: [10.2217/bmm-2016-0361](https://doi.org/10.2217/bmm-2016-0361), indexed in Pubmed: [28379039](https://pubmed.ncbi.nlm.nih.gov/28379039/).
- Liao YH, Xia Ni, Zhou SF, et al. Interleukin-17A contributes to myocardial ischemia/reperfusion injury by regulating cardiomyocyte apoptosis and neutrophil infiltration. *J Am Coll Cardiol*. 2012; 59(4): 420–429, doi: [10.1016/j.jacc.2011.10.863](https://doi.org/10.1016/j.jacc.2011.10.863), indexed in Pubmed: [22261166](https://pubmed.ncbi.nlm.nih.gov/22261166/).
- Zhang A, Mao X, Li L, et al. Necrostatin-1 inhibits Hmgb1-IL-23/IL-17 pathway and attenuates cardiac ischemia reperfusion injury. *Transpl Int*. 2014; 27(10): 1077–1085, doi: [10.1111/tri.12349](https://doi.org/10.1111/tri.12349), indexed in Pubmed: [24810904](https://pubmed.ncbi.nlm.nih.gov/24810904/).
- Qin C, Yap S, Woodman OL. Antioxidants in the prevention of myocardial ischemia/reperfusion injury. *Expert Rev Clin Pharmacol*. 2009; 2(6): 673–695, doi: [10.1586/cep.09.41](https://doi.org/10.1586/cep.09.41), indexed in Pubmed: [22112260](https://pubmed.ncbi.nlm.nih.gov/22112260/).
- Prabhu SD, Frangogiannis NG. The Biological Basis for Cardiac Repair After Myocardial Infarction: From Inflammation to Fibrosis. *Circ Res*. 2016; 119(1): 91–112, doi: [10.1161/CIRCRESAHA.116.303577](https://doi.org/10.1161/CIRCRESAHA.116.303577), indexed in Pubmed: [27340270](https://pubmed.ncbi.nlm.nih.gov/27340270/).
- Dewald O, Zymek P, Winkelmann K, et al. CCL2/Monocyte Chemoattractant Protein-1 regulates inflammatory responses critical to healing myocardial infarcts. *Circ Res*. 2005; 96(8): 881–889, doi: [10.1161/01.RES.0000163017.13772.3a](https://doi.org/10.1161/01.RES.0000163017.13772.3a), indexed in Pubmed: [15774854](https://pubmed.ncbi.nlm.nih.gov/15774854/).
- Frangogiannis NG, Dewald O, Xia Y, et al. Critical role of monocyte chemoattractant protein-1/CC chemokine ligand 2 in the pathogenesis of ischemic cardiomyopathy. *Circulation*. 2007; 115(5): 584–592, doi: [10.1161/CIRCULATION-AHA.106.646091](https://doi.org/10.1161/CIRCULATION-AHA.106.646091), indexed in Pubmed: [17283277](https://pubmed.ncbi.nlm.nih.gov/17283277/).
- Liehn EA, Piccinini AM, Koenen RR, et al. A new monocyte chemotactic protein-1/chemokine CC motif ligand-2 competitor limiting neointima formation and myocardial ischemia/reperfusion injury in mice. *J Am Coll Cardiol*. 2010; 56(22): 1847–1857, doi: [10.1016/j.jacc.2010.04.066](https://doi.org/10.1016/j.jacc.2010.04.066), indexed in Pubmed: [21087715](https://pubmed.ncbi.nlm.nih.gov/21087715/).
- Du S, Li Z, Xie X, et al. IL-17 stimulates the expression of CCL2 in cardiac myocytes via Act1/TRAF6/p38MAPK-dependent AP-1 activation. *Scand J Immunol*. 2020; 91(1): e12840, doi: [10.1111/sji.12840](https://doi.org/10.1111/sji.12840), indexed in Pubmed: [31630418](https://pubmed.ncbi.nlm.nih.gov/31630418/).

21. de Lemos JA, Morrow DA, Sabatine MS, et al. Association between plasma levels of monocyte chemoattractant protein-1 and long-term clinical outcomes in patients with acute coronary syndromes. *Circulation*. 2003; 107(5): 690–695, doi: [10.1161/01.cir.0000049742.68848.99](https://doi.org/10.1161/01.cir.0000049742.68848.99), indexed in Pubmed: [12578870](https://pubmed.ncbi.nlm.nih.gov/12578870/).
22. Gonzalez-Quesada C, Frangogiannis NG. Monocyte chemoattractant protein-1/CCL2 as a biomarker in acute coronary syndromes. *Curr Atheroscler Rep*. 2009; 11(2): 131–138, doi: [10.1007/s11883-009-0021-y](https://doi.org/10.1007/s11883-009-0021-y), indexed in Pubmed: [19228487](https://pubmed.ncbi.nlm.nih.gov/19228487/).
23. Tarzami ST, Calderon TM, Deguzman A, et al. MCP-1/CCL2 protects cardiac myocytes from hypoxia-induced apoptosis by a G(alpha)-independent pathway. *Biochem Biophys Res Commun*. 2005; 335(4): 1008–1016, doi: [10.1016/j.bbrc.2005.07.168](https://doi.org/10.1016/j.bbrc.2005.07.168), indexed in Pubmed: [16102724](https://pubmed.ncbi.nlm.nih.gov/16102724/).
24. Hengartner MO. The biochemistry of apoptosis. *Nature*. 2000; 407(6805): 770–776, doi: [10.1038/35037710](https://doi.org/10.1038/35037710), indexed in Pubmed: [11048727](https://pubmed.ncbi.nlm.nih.gov/11048727/).
25. Ashkenazi A, Fairbrother WJ, Levenson JD, et al. From basic apoptosis discoveries to advanced selective BCL-2 family inhibitors. *Nat Rev Drug Discov*. 2017; 16(4): 273–284, doi: [10.1038/nrd.2016.253](https://doi.org/10.1038/nrd.2016.253), indexed in Pubmed: [28209992](https://pubmed.ncbi.nlm.nih.gov/28209992/).
26. Wei MC, Zong WX, Cheng EH, et al. Proapoptotic BAX and BAK: a requisite gateway to mitochondrial dysfunction and death. *Science*. 2001; 292(5517): 727–730, doi: [10.1126/science.1059108](https://doi.org/10.1126/science.1059108), indexed in Pubmed: [11326099](https://pubmed.ncbi.nlm.nih.gov/11326099/).
27. Riedl SJ, Shi Y. Molecular mechanisms of caspase regulation during apoptosis. *Nat Rev Mol Cell Biol*. 2004; 5(11): 897–907, doi: [10.1038/nrm1496](https://doi.org/10.1038/nrm1496), indexed in Pubmed: [15520809](https://pubmed.ncbi.nlm.nih.gov/15520809/).
28. Johnson GL, Lapadat R. Mitogen-activated protein kinase pathways mediated by ERK, JNK, and p38 protein kinases. *Science*. 2002; 298(5600): 1911–1912, doi: [10.1126/science.1072682](https://doi.org/10.1126/science.1072682), indexed in Pubmed: [12471242](https://pubmed.ncbi.nlm.nih.gov/12471242/).
29. Zhang W, Liu HT. MAPK signal pathways in the regulation of cell proliferation in mammalian cells. *Cell Res*. 2002; 12(1): 9–18, doi: [10.1038/sj.cr.7290105](https://doi.org/10.1038/sj.cr.7290105), indexed in Pubmed: [11942415](https://pubmed.ncbi.nlm.nih.gov/11942415/).
30. Cuenda A, Rousseau S. p38 MAP-kinases pathway regulation, function and role in human diseases. *Biochim Biophys Acta*. 2007; 1773(8): 1358–1375, doi: [10.1016/j.bbamcr.2007.03.010](https://doi.org/10.1016/j.bbamcr.2007.03.010), indexed in Pubmed: [17481747](https://pubmed.ncbi.nlm.nih.gov/17481747/).
31. De Chiara G, Marcocci ME, Torcia M, et al. Bcl-2 Phosphorylation by p38 MAPK: identification of target sites and biologic consequences. *J Biol Chem*. 2006; 281(30): 21353–21361, doi: [10.1074/jbc.M511052200](https://doi.org/10.1074/jbc.M511052200), indexed in Pubmed: [16714293](https://pubmed.ncbi.nlm.nih.gov/16714293/).
32. Guo W, Liu X, Li J, et al. Prdx1 alleviates cardiomyocyte apoptosis through ROS-activated MAPK pathway during myocardial ischemia/reperfusion injury. *Int J Biol Macromol*. 2018; 112: 608–615, doi: [10.1016/j.ijbiomac.2018.02.009](https://doi.org/10.1016/j.ijbiomac.2018.02.009), indexed in Pubmed: [29410271](https://pubmed.ncbi.nlm.nih.gov/29410271/).
33. Kaiser RA, Lyons JM, Duffy JY, et al. Inhibition of p38 reduces myocardial infarction injury in the mouse but not pig after ischemia-reperfusion. *Am J Physiol Heart Circ Physiol*. 2005; 289(6): H2747–H2751, doi: [10.1152/ajpheart.01280.2004](https://doi.org/10.1152/ajpheart.01280.2004), indexed in Pubmed: [16143643](https://pubmed.ncbi.nlm.nih.gov/16143643/).
34. Shi P, Zhang L, Zhang M, et al. Platelet-Specific p38 α Deficiency Improved Cardiac Function After Myocardial Infarction in Mice. *Arterioscler Thromb Vasc Biol*. 2017; 37(12): e185–e196, doi: [10.1161/ATVBAHA.117.309856](https://doi.org/10.1161/ATVBAHA.117.309856), indexed in Pubmed: [28982666](https://pubmed.ncbi.nlm.nih.gov/28982666/).
35. Molkentin JD, Bugg D, Ghearing N, et al. Fibroblast-Specific Genetic Manipulation of p38 Mitogen-Activated Protein Kinase In Vivo Reveals Its Central Regulatory Role in Fibrosis. *Circulation*. 2017; 136(6): 549–561, doi: [10.1161/CIRCULATIONAHA.116.026238](https://doi.org/10.1161/CIRCULATIONAHA.116.026238), indexed in Pubmed: [28356446](https://pubmed.ncbi.nlm.nih.gov/28356446/).
36. Bridgewood C, Alase A, Watad A, et al. The IL-23p19/EBI3 heterodimeric cytokine termed IL-39 remains a theoretical cytokine in man. *Inflamm Res*. 2019; 68(6): 423–426, doi: [10.1007/s00011-019-01235-x](https://doi.org/10.1007/s00011-019-01235-x), indexed in Pubmed: [30989239](https://pubmed.ncbi.nlm.nih.gov/30989239/).

Submitted: 22 March, 2021

Accepted after reviews: 19 September, 2021

Available as AoP: 20 September, 2021

INSTRUCTIONS FOR AUTHORS

MANUSCRIPT SUBMISSION

Folia Histochemica et Cytobiologica accepts manuscripts (original articles, short communications, review articles) from the field of histochemistry, as well as cell and tissue biology. Each manuscript is reviewed by independent referees. Book reviews and information concerning congresses, symposia, meetings etc., are also published.

All articles should be submitted to FHC electronically online at www.fhc.viamedica.pl where detailed instruction regarding submission process will be provided.

AUTHOR'S STATEMENT

The manuscript must be accompanied by the author's statement that it has not been published (or submitted to publication) elsewhere.

GHOSTWRITING

Ghostwriting and guest-authorship are forbidden. In case of detecting ghost written manuscripts, their actions will be taking involving both the submitting authors and the participants involved.

The corresponding author must have obtained permission from all authors for the submission of each version of the paper and for any change in authorship. Submission of a paper that has not been approved by all authors may result in immediate rejection.

COST OF PUBLICATION

The cost of publication of accepted manuscript is 800 Euro.

OFFPRINTS

PDF file of each printed paper is supplied for the author free of charge. Orders for additional offprints should be sent to the Editorial Office together with galley proofs.

ORGANIZATION OF MANUSCRIPT

The first page must include: the title, name(s) of author(s), affiliation(s), short running head (no more than 60 characters incl. spaces) and detailed address for correspondence including e-mail. Organization of the manuscript: 1. Abstract (not exceeding one typed page — should consist of the following sections: Introduction, Material and methods, Results, Conclusions); 2. Key words (max. 10); Introduction; Material and methods; Results; Discussion; Acknowledgements (if any); References; Tables (with legends); Figures; Legends to figures.

In a short communication, Results and Discussion should be written jointly. Organization of a review article is free.

TECHNICAL REQUIREMENTS

Illustrations (line drawings and halftones) — either single or mounted in the form of plates, can be 85 mm, 125 mm, or 175 mm wide and cannot exceed the size of 175 × 250 mm. The authors are requested to plan their illustrations in such a way that the printed area is economically used. Numbers, inscriptions and abbreviations on the figures must be about 3 mm high. In case of micrographs, magnification (e.g. × 65 000) should be given in the legend. Calibration bars can also be used. For the best quality of illustrations

please provide images in one of commonly used formats e.g. *.tiff, *.png, *.pdf (preferred resolution 300 dpi). Tables should be numbered consecutively in Arabic numerals and each table must be typed on a separate page. The authors are requested to mark the places in the text, where a given table or figure should appear in print. Legends must begin on a new page and should be as concise as necessary for a self-sufficient explanation of the illustrations. PDF file of each paper is supplied free of charge.

CITATIONS

In References section of article please use following American Medical Association 9th Ed. citation style. Note, that items are listed numerically in the order they are cited in the text, not alphabetically. If you are using a typewriter and cannot use italics, then use underlining.

Authors: use initials of first and second names with no spaces. Include up to six authors. If there are more than six, include the first three, followed by et al. If no author is given, start with the title. **Books:** include the edition statement (ex: 3rd ed. or Rev ed.) between the title and place if it is not the first edition. **Place:** use abbreviations of states, not postal codes. **Journals:** abbreviate titles as shown in *Index Medicus*. If the journal does not paginate continuously through the volume, include the month (and day). **Websites:** include the name of the webpage, the name of the entire website, the full date of the page (if available), and the date you looked at it. The rules concerning a title within a title are *not* displayed here for purposes of clarity. See the printed version of the manual for details. For documents and situations not listed here, see the printed version of the manual.

EXAMPLES

Book:

1. Okuda M, Okuda D. *Star Trek Chronology: The History of the Future*. New York: Pocket Books; 1993.

Journal or Magazine Article (with volume numbers):

2. Redon J, Cifkova R, Laurent S et al. Mechanisms of hypertension in the cardiometabolic syndrome. *J Hypertens*. 2009; 27(3):441–451. doi: 10.1097/HJH.0b013e32831e13e5.

Book Article or Chapter:

3. James NE. Two sides of paradise: the Eden myth according to Kirk and Spock. In: Palumbo D, ed. *Spectrum of the Fantastic*. Westport, Conn: Greenwood; 1988:219–223.

When the manufacturers of the reagents etc. are mentioned for the first time, town, (state in the US) and country must be provided whereas for next referral only the name of the firm should be given.

Website:

4. Lynch T. DSN trials and tribble-ations review. Psi Phi: Bradley's Science Fiction Club Web site. 1996. Available at: <http://www.bradley.edu/campusorg/psiphi/DS9/ep/503r.htm>. Accessed October 8, 1997.

Journal Article on the Internet:

5. McCoy LH. Respiratory changes in Vulcans during pon farr. *J Extr Med* [serial online]. 1999;47:237–247. Available at: http://infotrac.galegroup.com/itweb/nysl_li_liu. Accessed April 7, 1999.

